

**DEVELOPMENT OF MESOPOROUS NANOSTRUCTURED
CATALYSTS FOR HIGH EFFICIENCY HYDROGEN
PRODUCTION FROM WATER**

BY

ALAALDIN MOHAMED ABDALLA ADAM

A Dissertation Presented to the
DEANSHIP OF GRADUATE STUDIES

KING FAHD UNIVERSITY OF PETROLEUM & MINERALS

DHAHRAN, SAUDI ARABIA

In Partial Fulfillment of the
Requirements for the Degree of

DOCTOR OF PHILOSOPHY

In

CHEMISTRY

DECEMBER 2017

KING FAHD UNIVERSITY OF PETROLEUM & MINERALS

DHAHRAN- 31261, SAUDI ARABIA

DEANSHIP OF GRADUATE STUDIES

This thesis, written by **ALAALDIN MOHAMED ABDALLA ADAM** under the direction
his thesis advisor and approved by his thesis committee, has been presented and accepted
by the Dean of Graduate Studies, in partial fulfillment of the requirements for the degree
of **DOCTOR OF PHILOSOPHY IN CHEMISTRY**.



25/3/2018

Dr. Abdulaziz A. Al-Saadi
Department Chairman




Dr. Sam A. Zummo
Dean of Graduate Studies

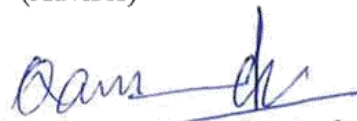


29/3/19

Date



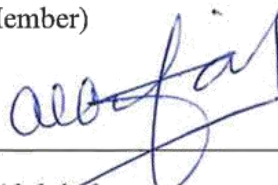
Dr. Mohammad Nahid Siddiqui
(Advisor)



Dr. Mohammad Qamar
(Co-Advisor)



Dr. Abdullah Abulkibash
(Member)



Dr. Abdulrahman A. Al-Arfaj
(Member)



Dr. Basheer Chanbasha
(Member)

© Alaalain Mohamed Abdalla Adam

2017

Dedication

This thesis is dedicated to my parents, wife, son, brothers and sisters for their continuous prayer and support...

ACKNOWLEDGMENTS

I would like to thank my great creator almighty Allah for giving me life, health, strength patience, power and science to finish my study. Also, I would like to express my deepest appreciations to my thesis Advisor Dr. Mohammad Nahid Siddiqui for guiding me throughout the doctorate program, encouragement, significant comments, and continuous help and support during the study. I want to show my deep gratitude to my Co-adviser Dr. Mohammad Qamar, who supported me throughout the PhD project with patience. His insightful comments and expertise assisted me in cultivating my scientific research ability. I wish to extend my gratitude to thesis committee members Dr. Abdullah Abulkibash, Dr. Abdulrahman A. Al-Arfaj and Dr. Basheer Chanbasha for their valuable advice, encouragement and significant comments which supported me to complete this research.

It's my pleasure to acknowledge the Ministry of Education, Saudi Arabia, through the King Fahd University of Petroleum and Minerals for giving me this opportunity to pursue my Ph.D. degree. My deep thank is extended to the chemistry department chairman Dr. Abdulaziz A. Al-Saadi, former chairman Dr. Abdallah Al-Hamdan, Dr. Bassam El-Ali (Graduate coordinator) and all faculty members and staff. I take this opportunity to express my sincere gratitude to the center of excellence in nanotechnology (CENT) for their help and support.

TABLE OF CONTENTS

ACKNOWLEDGMENTS	V
TABLE OF CONTENTS.....	VI
LIST OF TABLES.....	IX
LIST OF FIGURES.....	X
LIST OF ABBREVIATIONS.....	XV
ABSTRACT	XVII
ملخص الرسالة	XIX
CHAPTER 1 INTRODUCTION.....	1
1.1 Energy crisis and global warming:	1
1.2 Electrocatalytic water splitting:.....	2
1.3 Research Objectives:	7
CHAPTER 2 LITERATURE REVIEW	10
2.1 Transition metals based carbides and phosphides compounds:	10
2.1.1 Crystal Structure:.....	10
2.1.2 Bonding in Carbides and phosphides compounds:	11
2.2 Transition metal carbides as (HER) electrocatalysts:	13
2.2.1 Metal-organic frameworks (MOFs)-derived porous carbides:	17
2.2.2 Transition metal phosphides as HER electrocatalysts:	19
2.2.3 Carbon nanotubes as a support for HER electrocatalysts:	24
CHAPTER 3.....	26
METAL ORGANIC FRAMEWORK-GUIDED GROWTH OF MO ₂ C EMBEDDED IN MESOPOROUS CARBON AS HIGH-PERFORMANCE AND STABLE ELECTRO-CATALYST FOR HYDROGEN EVOLUTION REACTION	26

3.1	Introduction:	26
3.2	Experimental:	29
3.2.1	Synthesis of Metal Organic Framework (MIL-53(Al)):	29
3.2.2	Synthesis of Mo ₂ C/C electrocatalyst:	30
3.2.3	Characterization:	30
3.2.4	Evaluation of electrocatalytic activity:	31
3.3	Results and discussion:	32
3.4	Conclusion:	53
CHAPTER 4:		54
RATIONAL GROWTH OF HIGH-PERFORMANCE MOLYBDENUM CARBIDE ON CARBON NANOTUBES FOR ELECTROCHEMICAL HYDROGEN EVOLUTION REACTION:		54
4.1	Introduction:	54
4.2	Experimental:	56
4.2.1	Synthesis of Mo ₂ C/CNT electrocatalyst:	56
4.2.2	Characterization:	57
4.2.3	Evaluation of electrocatalytic activity:	57
4.3	Results and discussion:	58
4.4	Conclusion:	78
CHAPTER 5:		79
OXALATE-DIRECTED GROWTH OF MOLYBDENUM PHOSPHIDE ON CARBON NANOTUBE AS HIGH-PERFORMANCE AND DURABLE ELECTROCATALYST FOR HYDROGEN EVOLUTION REACTION:		79
5.1	Introduction:	79
5.2	Experimental:	80
5.2.1	Synthesis of MoP/CNT electrocatalyst:	80
5.2.2	Characterization:	81
5.2.3	Evaluation of electrocatalytic activity:	81
5.3	Results and discussions:	82
5.4	Conclusion:	97

CHAPTER 6.....	98
HOLLOW AND INTERCONNECTED SCAFFOLD OF COP AND CARBON NANOTUBES AS HIGH PERFORMANCE ELECTROCATALYST FOR HYDROGEN EVOLUTION REACTION.....	98
6.1 Introduction:.....	98
6.2 Experimental:.....	100
6.2.1 Synthesis of cobalt phosphide/carbon nanotubes (CoP/CNT) electrocatalyst:	100
6.2.2 Characterization:	101
6.2.3 Electrochemical characterization:	101
6.2.4 Calculation of turnover frequency (TOF):.....	102
6.3 Results and discussions:	103
6.4 Conclusion:	122
CHAPTER 7.....	123
CONCLUSION AND RECOMMENDATIONS	123
REFERENCES.....	127
APPENDIX A.....	157
APPENDIX B.....	160
VITAE.....	161

LIST OF TABLES

Table 1: Comparison of electrocatalysts (Mo_2C) for HER.....	52
Table 2: Comparison of electrocatalysts (Mo_2C) for HER.....	77
Table 3: Comparison of electrocatalysts (MoP) for HER in acidic medium.....	96
Table 4: Comparison of electrocatalysts (CoP) for HER.....	121

LIST OF FIGURES

Figure 1: Annual carbon dioxide emissions gross in mega tone across sectors.	2
Figure 2: Contributions of production pathways for the worlds' hydrogen yield.	3
Figure 3: Schematic illustration of water electrolyzer.	5
Figure 4: Schematic representation the overall concept of a hydrogen renewable energy system for distributed power generation.	7
Figure 5: Typical crystallographic structures of transition metal carbides. a) face-centered cubic, b) hexagonal closed packed and c) simple hexagonal.	11
Figure 6: Common crystal structures of transition metal phosphides.	12
Figure 7: Common metal Carbides throughout the periodic table.	13
Figure 8: SEM images of, (a) β -Mo ₂ C synthesized by mesitylamine at 750 °C (b) β -Mo ₂ C synthesized by 4-Cl-o-phenylenediamine, at 675 °C (c) α -MoC _{1-x} synthesized by o-phenylenediamine, at 625 °C (d) α -MoC _{1-x} synthesized by p-phenylenediamine, at 675 °C (e) β -Mo ₂ C synthesized by aniline with 4 : 1 amine : Mo ratio, at 675 °C (f) β -Mo ₂ C synthesized by 2-nitro-p-phenylene-diamine, at 875 °C, (g) α -MoC _{1-x} synthesized by p-phenylene-diamine with 4: 1 amine : Mo ratio, at 675 °C (h) α -MoC _{1-x} synthesized by p- phenylene-diamine with 8 : 1 amine : Mo ratio, at 850 °C (i) β -Mo ₂ C synthesized by 1,6-hexanediamine, at 675 °C, (j) β -Mo ₂ C synthesized by 4- nitro-o-phenylene-diamine, at 850 °C (k) α -MoC _{1-x} synthesized by hexamethylenetetramine, at 850 °C, (l) β -Mo ₂ C synthesized by hexamethylenetetramine, at 900 °C.	15
Figure 9: (A) SEM image and (B and C) TEM images of nanoporous Mo ₂ C nanowires. (D) Polarization curve of np-Mo ₂ C NWs compared with commercial Mo ₂ C and bare glassy carbon electrodes in 0.5 M H ₂ SO ₄ . (E) Polarization curve of np-Mo ₂ C NWs before and after 1000 cycles. The inset shows its chronopotentiometry response at η =130 mV.	16
Figure 10: Synthesis of the Fe ₃ C/Mo ₂ C@NPGC nanohybrid derived from Polyoxometalate-based metal–organic frameworks.	18
Figure 11: Schematic representation of the confined preparation of MoS ₂ /3D-NPC.	20
Figure 12: LSV measurements of Mo, Mo ₃ P and MoP in concentrated acid solution (0.5M H ₂ SO ₄).	21
Figure 13: Scan electron microscopy images show the morphologies from starting material of cobalt oxide NWs (a), and Co ₃ O ₄ NWs (b) to the final product of CoP NWs (c). EDX mapping of CoP NWs. (d).	23
Figure 14: Schematic representation of the carbon nanotube formation by rolling up a 2D graphene	24
Figure 15: Schematic illustration of the likely pathways involved in the formation of Mo ₂ C/C electrocatalyst.	33
Figure 16: XRD spectra of MoO ₂ obtained at 800 °C annealed under N ₂ gas.	35

Figure 17: Powder XRD patterns of (A) MIL-53(Al) before and after molybdenum impregnation, and (B) Mo ₂ C/C nanocomposite before and after Al removal.	35
Figure 18: XPS survey spectra of Mo ₂ C/C before (a) and after Al removal (b).	36
Figure 19: BET isotherms of (A) MIL-53(Al) and (B) Mo ₂ C/C nanocomposite together with pore distribution (Fig. B inset).	37
Figure 20: FESE, TEM, SAED and HR-TEM of Mo ₂ C/C.	39
Figure 21: XRD and TEM of Mo ₂ C/XC.	40
Figure 22: SEM and elemental mapping of carbon, molybdenum and oxygen present in Mo ₂ C/C.	40
Figure 23: XPS signatures of Mo ₂ C/C: (A) Mo 3d, (B) C 1s.	41
Figure 24: (A) Potentiodynamic curves showing the effect of carburization temperature and (B) catalyst loading on GCE. (C) Comparative current-potential curves of Pt/C, Mo ₂ C/C and Mo ₂ C/XC72 and (D) their Tafel plots. (E) A time-dependent profile of current density at $\eta = 165$ mV for 20 h, and (F) polarization curves before and after durability test.	43
Figure 25: XRD spectra of Mo ₂ C/C carburized at different temperature.	44
Figure 26: Effect of annealing temperature on cyclic voltammograms (CVs) of Mo ₂ C/C recorded at different scan rates from 5 to 100 mVs ⁻¹ , and their corresponding plots of the current density at 0.355 V _{RHE} vs. scan rate. CVs were recorded in non-faradic region. The linear slopes are equivalent to twice of the electrochemical double layer capacitance (C _{dl}).	45
Figure 27: Potentiodynamic curves showing the effect of temperature on specific current density calculated with real surface area.	46
Figure 28: (A) Nyquist plots recorded at different potential (vs. NHE), (B) Nyquist plots with enlarged region showing two semicircles, (C) Bode plots showing two two-time constants, (D) comparative Nyquist plots of Mo ₂ C/C and Mo ₂ C/XC at $\eta = 100$ mV and 150 mV, (E) comparative Bode plots of Mo ₂ C/C and Mo ₂ C/XC at $\eta = 100$ mV, and (F) Tafel plot. Inset figure in 25 A –electrical equivalent circuit model used to fit the EIS results (also in Figure 29).	50
Figure 29: Two-time constant electrical equivalent circuit model utilized to fit the electrochemical impedance (EIS) results of hydrogen evolution reaction. R _s - series resistance, C _{dl} and C _{d2} are double layer capacitance, R _{ct} - charge transfer resistance for HER, R _p - resistance related to the surface porosity.	51
Figure 30: Suggested sequence of complexation, nucleation and concomitant growth of Mo ₂ C on CNT surface.	59
Figure 31: Photographs showing the change in color of MoCl ₅ and ethanol solution after addition of oxalic acid.	60

Figure 32: ^{13}C NMR of (A) solution of $\text{H}_2\text{C}_2\text{O}_4$ and $\text{C}_2\text{H}_5\text{OH}$ and (B) solution of MoCl_5 , $\text{H}_2\text{C}_2\text{O}_4$ and $\text{C}_2\text{H}_5\text{OH}$, and ^1H NMR of (C) solution of MoCl_5 , $\text{H}_2\text{C}_2\text{O}_4$ and $\text{C}_2\text{H}_5\text{OH}$	60
Figure 33: XRD, FESEM, TEM, HR-TEM and SAED of oxalate-derived β - $\text{Mo}_2\text{C}/\text{CNT}$	62
Figure 34: TEM of $\text{Mo}_2\text{C}/\text{CNT}$ obtained in the presence (A) and absence (B) of oxalic acid.	62
Figure 35: FESEM and elemental mapping of carbon, molybdenum and oxygen present in $\text{Mo}_2\text{C}/\text{CNT}$	63
Figure 36: XPS of oxalate-prepared $\text{Mo}_2\text{C}/\text{CNT}$	64
Figure 37: A- effect of synthesis temperature, B- effect of Mo content, C- effect of catalyst loading, D- (A- Pt/C, B & C- $\text{Mo}_2\text{C}/\text{CNT}$ prepared with and without oxalic acid, respectively, E- stability before and after 1000 potentiodynamic sweeps, and F-stability before and after potentiostatic measurement.	66
Figure 38: XRD spectra of $\text{Mo}_2\text{C}/\text{CNT}$ obtained at different synthesis temperature.	67
Figure 39: Cyclic voltammograms (A, C, E, G) of $\text{Mo}_2\text{C}/\text{CNT}$ recorded at different scan rates from 5 to 100 mVs^{-1} , and their corresponding plots (B, D, F, H) of the current density at $0.248 \text{ V}_{\text{RHE}}$ vs. scan rate as a function of Mo_2C content. CVs were recorded in non-faradic region. The linear slopes are equivalent to twice of the electrochemical double layer capacitance (C_{dl}). (I) Nyquist plot as a function of molybdenum contents.	70
Figure 40: Nyquist and Bode plots for $\text{Mo}_2\text{C}/\text{CNT}$: (A) & (B) – prepared in the absence of oxalic acid, (C) & (D) – prepared in the presence oxalic acid. (E) Enlarged view of Nyquist plots showing two semicircles, (F) comparative Tafel plots for $\text{Mo}_2\text{C}/\text{CNT}$ prepared with (51.3 mVdec^{-1}) and without (53.3 mVdec^{-1}) oxalic acid.	72
Figure 41: Two-time constant electrical equivalent circuit model utilized to fit the electrochemical impedance(EIS) results of hydrogen evolution reaction. R_s – series resistance, C_{dl} and $C_{\text{dl}2}$ are double layer capacitance, R_{ct} – charge transfer resistance for HER, R_p – resistance related to the surface porosity.	73
Figure 42: N_2 adsorption-desorption isotherms of $\text{Mo}_2\text{C}/\text{CNT}$ prepared in the presence (A) and absence (B) of oxalic acid.	74
Figure 43: Cyclic voltammograms (CVs) of $\text{Mo}_2\text{C}/\text{CNT}$ recorded at different scan rates from 5 to 100 mVs^{-1} , and their corresponding plots of the current density at $0.248 \text{ V}_{\text{RHE}}$ vs. scan rate. (A) & (B) – prepared in the absence of oxalic acid, (C) & (D) – prepared in the presence oxalic acid.	74
Figure 44: A representative scheme shows proposed reaction mechanism steps; complexation, nucleation and concomitant growth of MoP on CNT surface.	84

Figure 45: ^{13}C NMR of (A) solution of $\text{H}_2\text{C}_2\text{O}_4$ and $\text{C}_2\text{H}_5\text{OH}$ and (B) solution of MoCl_5 , $\text{H}_2\text{C}_2\text{O}_4$ and $\text{C}_2\text{H}_5\text{OH}$, inset photographs showing the change in color of MoCl_5 and ethanol solution after addition of oxalic acid, and ^1H NMR of (C) solution of MoCl_5 , $\text{H}_2\text{C}_2\text{O}_4$ and $\text{C}_2\text{H}_5\text{OH}$	85
Figure 46: Comparative XRD of MoP/CNT prepared without oxalic acid (black) and prepared with oxalic acid (red).	85
Figure 47: XPS spectra of; (a) Survey of MoP/CNT, (b) C 1s, (c) Mo 3d and (d) P 2p. ...	86
Figure 48: TEM images of (a) MoP/CNT without oxalic acid, (b-d) MoP/CNT with oxalic acid, (e) HRTEM and (f) SAED	87
Figure 49: Elemental mapping of carbon, oxygen, phosphorous and molybdenum present in MoP/CNT.	88
Figure 50: a) Linear sweep voltammograms of A- MoP/CNT prepared in absence of oxalic acid, B- prepared in presence of oxalic acid and C- Pt/C recorded in 0.5M H_2SO_4 and (b) recorded in 1M KOH solution. c) Polarization curves before and after 1000 sweeps and d) a time-dependent profile of current density at $\eta = 115 \text{ mV}$ for 11 h	90
Figure 51: Nyquist plots for MoP/CNT: (a)– prepared in the absence of oxalic acid, ((b))– prepared in the presence oxalic acid. (c) Enlarged view of Nyquist plots showing two semicircles, and (d) their comparative Bode plots at $\eta = 150 \text{ mV}$. (e) comparative Tafel plots for MoP/CNT prepared with (51.6 mVdec^{-1}) and without (54.5 mVdec^{-1}) oxalic acid. (f) & (g) Cyclic voltammograms of MoP/CNT recorded at different scan rates from 5 to 100 mVs^{-1} , and (h) & (g) their corresponding plots of the current density at 0.248 V_{RHE} vs. scan rate. CVs were recorded in non-faradic region. The linear slopes are equivalent to twice of the electrochemical double layer capacitance (C_{dl}).	92
Figure 52: N_2 adsorption-desorption isotherms of MoP/CNT prepared in the presence (A) and absence (B) of oxalic acid.	94
Figure 53: Powder XRD patterns for (A) hollow CoP/CNT (red) and (B) non-hollow CoP/CNT (black).	104
Figure 54: (A) XPS survey scan and high-resolution spectra of (B) C 1s, (C) Co 2p and (D) P 2p for CoP/CNT	104
Figure 55: (A) low and (B) high-magnified TEM images of CoP/CNT. (C) low and (D) high magnified-TEM, (E) HR-TEM and (F) SAED images of hollow CoP/CNT.....	106
Figure 56: Preparation process of HMT-derived CoP/CNT electrocatalyst.	109
Figure 57: (A) ^1H NMR spectra of HMT (bottom) and its solution with $\text{Co}(\text{CH}_3\text{COO})_2 \cdot 4\text{H}_2\text{O}$ and ethanol (top) (B) ^{13}C NMR spectrum of HMT (bottom) and its solution with $\text{Co}(\text{CH}_3\text{COO})_2 \cdot 4\text{H}_2\text{O}$ and ethanol (top).....	110

Figure 58: EDS elemental mapping of carbon, oxygen, phosphorous and cobalt present in CoP/CNT.....	110
Figure 59: XRD of CoO/CNT obtained at 250 °C, CoO@Co _x P/CNT core-shell structure formed at 275 °C and CoP/CNT prepared at temperature of 300 and 350 °C.....	111
Figure 60: Powder XRD patterns of sample prepared at different temperatures (250, 300, 350 and 400 °C).	112
Figure 61: (A) Effect of phosphorization temperatures. (B) effect of Co content. (C) LSV curves of A-Pt/C, B- Hollow nanospheres CoP/CNT and C- nonhollow CoP/CNT in 0.5 M H ₂ SO ₄ and (D) in 1M KOH (D). (E) stability before and after 1000 potentiodynamic sweeps, and (F) Time-dependent potentiostatic measurement.....	114
Figure 62: N ₂ sorption isotherms of (A) hollow CoP/CNT and (B) nonhollow CoP/C.	115
Figure 63: Cyclic voltammograms (CVs) of CoP/CNT recorded at different scan rates from 5 to 150 mVs ⁻¹ , and their corresponding plots of the current density at 0.245 VRHE vs. scan rate. (A) & (B) – Hollow CoP/CNT, (C) & (D) – nonhollow CoP/CNT. CVs were recorded in non-faradic region. The linear slopes are equivalent to twice of the electrochemical double layer capacitance (Cdl).	117
Figure 64: Nyquist and Bode plots for CoP/CNT: (A) & (B)- Solid CoP/CNT, (C) & (D)- Hollow CoP/CNT, (E) Enlarged view of Nyquist plots showing two semicircles, and (F) Their Tafel plots of 54 mVdec ⁻¹ and 56 mV/dec ⁻¹ , respectively.	118
Figure 65: (A) The Cyclic voltammograms recorded between -0.2 and 0.6 V vs. NHE with scan rate of 20 mV/s for A- Non-Hollow CoP/CNT and B- Hollow CoP/CNT and (B) their corresponding TOF Vs overpotentials profiles.	119
Figure 66: Polarization profiles of MoP/CNT prepared at different synthetic temperatures.	157
Figure 67: LSVs of MoP/CNT obtained as function of Mo content.....	157
Figure 68: Linear sweep voltammograms showing Effect of catalyst loading of MoP/CNT.....	158
Figure 69: XRD spectra of MoP/CNT obtained at different synthesis temperature.	158
Figure 70: Temperature-dependent evolution in XRD patterns of MoP/CNT obtained in the presence of oxalic acid.	159
Figure 71: Cyclic voltammograms (A, C, E, G) of CoP/CNT recorded at different scan rates from 5 to 150 mVs ⁻¹ , and their corresponding plots (B, D, F, H) of the current density at 0.245 VRHE vs. scan rate as a function of CoP content. (I) Nyquist plot as a function of cobalt contents.	160

LIST OF ABBREVIATIONS

FESEM	: Field emission scanning electron microscope
PDF	: Powder Diffraction File
LSV	: Linear Sweep Voltammetry
HER	: Hydrogen Evolution Reaction
OER	: Oxygen Evolution Reaction
RHE	: Reversible Hydrogen Electrode
NHE	: Normal Hydrogen Electrode
HMT	: Hexamethylenetetramine
XRD	: X – ray Diffractometer
PEC	: Photoelectrochemical
Min	: Minute
s	: Second
mA	: Milliampere
nm	: Nanometer
mL	Milliliter
eV	: Electron Volt
°C	: Degree Celsius
V	: Volt
θ	: Theta
R_s	: Solution resistance
C_{dl}	: Electrical double layer capacitance
J	: Geometric current density
MOFs	: metal-organic frameworks

Deg.	: Degree
GR & RGO	: Graphene and reduced graphene oxide
η	: Overpotential
CF	: carbon flake
PC	: porous carbon
NPCNT:	: nitrogen & phosphorous-doped carbon nanotubes
NC	: Nitrogen doped Carbon
NP	: Nanoparticles

ABSTRACT

Full Name : [ALAALDIN MOHAMED ABDALLA ADAM]
Thesis Title : [Development of Mesoporous Nanostructured Catalysts for High Efficiency Hydrogen Production from Water]
Major Field : [Chemistry]
Date of Degree : [December 2017]

One of the main impediments facing the large-scale production of hydrogen (H_2) via water electrolysis is the use of expensive platinum metal (Pt) as an electrocatalyst. Early transition metal carbides and phosphides with platinum-like catalytic behavior have emerged as economic and earth-abundant alternatives to Pt. However, most of the synthetic procedures employed to produce these catalysts have led to bulky and low surface area products due to the agglomeration and coalescence of the metal during crystallization, which restrains their application for catalytic H_2 reaction. We, therefore, developed novel preparation protocols to improve the dispersion of the active sites on the carbon supports. We showed that highly porous frameworks of MIL-53, a metal organic framework, could be used as a template to guide the formation of highly dispersed molybdenum carbide (Mo_2C) embedded within the mesoporous carbon. The other strategy was based on the complexation method. Molybdenum was coordinated with oxalate group using oxalic acid, which modified the self-assembling of molecular precursor and controlled the nucleation and growth of Mo_2C and molybdenum phosphide (MoP) on CNTs. In addition, we demonstrated the growth of interconnected hollow scaffold of cobalt phosphide (CoP) on CNTs. Hexamethylenetetramine was used as a structure-directing agent. Plausible growth mechanisms were proposed. The methods are simple with the potential to scale-up.

Composition were characterized using standard techniques, such as transmission and high-resolution transmission electron microscope, field emission scanning electron microscope, powder X-ray diffraction, X-ray photoelectron spectroscopy (XPS), and so forth.

The potential of as-prepared electrocatalysts was evaluated as low-cost electrodes for hydrogen evolution reaction (HER), both in acidic and basic electrolytes. It was demonstrated that smaller particle size with better dispersion, hollow and interconnected artifacts impart benign attributes, such as enhanced specific and electrochemically active surface area, low intrinsic charge transfer resistance, high interfacial charge transfer kinetics, and improved mass transport, to electrocatalysts. As a result, the electrode comprising as-synthesized compositions exhibited remarkable electrocatalytic performance, outperforming most of the electrocatalyst reported as yet.

The findings offer fresh impetus to engineer Pt-free electrode materials with high activity for large scale and sustainable H₂ production through electrolysis.

ملخص الرسالة

الاسم الكامل: علاء الدين محمد عبد الله ادم

عنوان الرسالة: تطوير الحفازات المسامية ذات التركيب النانوي لانتاج الهيدروجين من الماء باعلي كفاءة

التخصص: الكيمياء

تاريخ الدرجة العلمية: ديسمبر 2017

من المعوقات الاساسيه التي تواجه انتاج الهيدروجين بكميات كبيرة عن طريق التحليل الكهربائي للماء هي استخدام معدن البلاتين (Pt) ذو التكلفة العالية كعامل حفاز كهربائي. كبريدات وفوسفيدات العناصر الانتقالية ذات الخصائص التحفيزية الشبيهة بالبلاتين برزت كبدايل متوفرة وذات جدوي اقتصاديه مقارنة بالبلاتين. لكن معظم طرق التحضير المستخدمة لانتاج هذه الحفازات الكهربيه أدت الي منتج ذو كتله ضخمة ومساحة سطح منخفضة بسبب تجمع وتكتل المعدن اثناء عمليه التكوين البلوري، والذي كبح من تطبيقها لتفاعل الهيدروجين التحفيزي. لهذه الاسباب طورنا بروتوكولات تحضير اصيله لتحسين انتشار المواقع النشطة علي دعائمات كربونيه، وبرهنا امكانية استعمال تركيب عالي المسامية MIL-53 (اطار معدني عضوي) كقالب لتوجيه تكوين كبريد الموليبيدينوم (Mo_2C) ذو الانتشاريه عاليه واندغاميه علي الكربون المسامي.

واستندت استراتيجيه اخري علي طريقه التعقيد (تكوين المعقد) حيث تم تكوين رابطه تناسقيه بين الموليبيدينوم ومجموعة الأوكسالات عند استخدام حمض الاوكساليك والتي ادت الي تعديل التجمع الذاتي للجزيئات البادئه وبالتالي التحكم بالتنوي والنمو لكبريد الموليبيدينوم و فوسفيد الموليبيدينوم علي انابيب الكربون النانويه (CNTs). بالاضافه لذلك اثبتنا نمو فوسفيد الكوبالت (CoP) الاجوف والمترايط علي دعائمه من CNTs. وتم استخدام هيكسامثيلينترامين كعامل توجيهي تركيبتي. واقترحنا اليات نمو محتملة. هذه الطرق بسيطه مع امكانية تطبيقها علي نطاق واسع. وقد تم توصيف التركيب الكيميائي لهذه الحفازات باستعمال التقنيات القياسيه مثل انتقال وعاليه الدقة انتقال الالكترون الميكروسكوب (TEM/HRTEM)، ميكروسكوب حقل انبعاث مسح الالكترون (FESEM)، أشعة الحيوذ السينيه (XRD)، الاشعة السينيه الضوئيه الطيفيه (XPS). وقد تم تقييم امكانية الحفازات الكهربيه المصنعه كأقطاب بتكلفة منخفضه لتحفز تفاعل تصاعد الهيدروجين (HER) في كلا من الاوساط الحمضيه والقاعدية. وقد اثبت ان الجزئي ذو الحجم الاصغر مع حسن توزيعه، والتركيبات ذات الشكل الأجوف والمتشابك تضيف سمات حميده مثل تحسين مساحة

السطح الكهروكيميائية والنوعية، مقاومة انتقال الشحنة المنخفض، سرعة انتقال الشحنة البينية العالي و تحسن انتقال الكتلة لغرض التحليل الكهربائي. ونتيجة لذلك القطب الذي يحتوي علي التركيبات المصنعة اظهرت اداء كهروتحفيزي ملحوظ، متفوقا علي معظم الحفازات الكهربائية المنشورة حتي الان. وهذه النتائج تعطي قوة دفع جديدة لتصميم مواد قطبية خالية من البلاتينيوم (Pt) مع نشاطيه عالية لأنتاج الهيدروجين علي مدي واسع ودائم بأستخدام التحليل الكهربائي.

CHAPTER 1

Introduction

1.1 Energy crisis and global warming:

The global energy demand is currently dependent on hydrocarbon fuels derived from natural gas, oil and coal, which known as fossil fuels. In the last few years, the global energy consumption was growing rapidly, for example, in 2013 the world's energy need has been increased by 2.3% with respect to that in 2012 and estimated to increase by 77% in 2050 [1–3] . Nowadays, fossil fuels are contributing to 90% of the world's energy use [4]. However, their contentious production and consumption have led to serious environmental and health impacts. The heavy use of fossil fuels releases a high concentration of anthropogenic carbon dioxide gas (CO₂) into the atmosphere, which contributes significantly to global warming and the earth climate change. For instance, CO₂ emission was increased enormously in Saudi Arabia during the period from 2000 to 2010, and projected to be doubled by 2030 (Figure 1). Another drawback is that fossil fuels are non-renewable energy sources and there is a rapid depletion in oil reserve with increasing demand for mankind's needs [1, 5, 6].

As a result of on growing public concerns on these consequences, developing alternatively environmentally-benign renewable energy technologies are urgently required for energy storage and conversion. The recent statistics showed that emerged renewable technologies such as wind, solar, hydropower, geothermal, biofuels and hydrogen energy represent nearly the quarter of the total worldwide energy consumption. Hydrogen is

presumably the most promising fuel Among all renewable sources due to its highest specific energy density with zero emission greenhouse gases and can be produced in high purity via the environmentally-friendlily electrochemical water splitting. Thus, the transformation from hydrocarbons based energy to a hydrogen economy is expected to play a significant role in the recent future [2, 7].

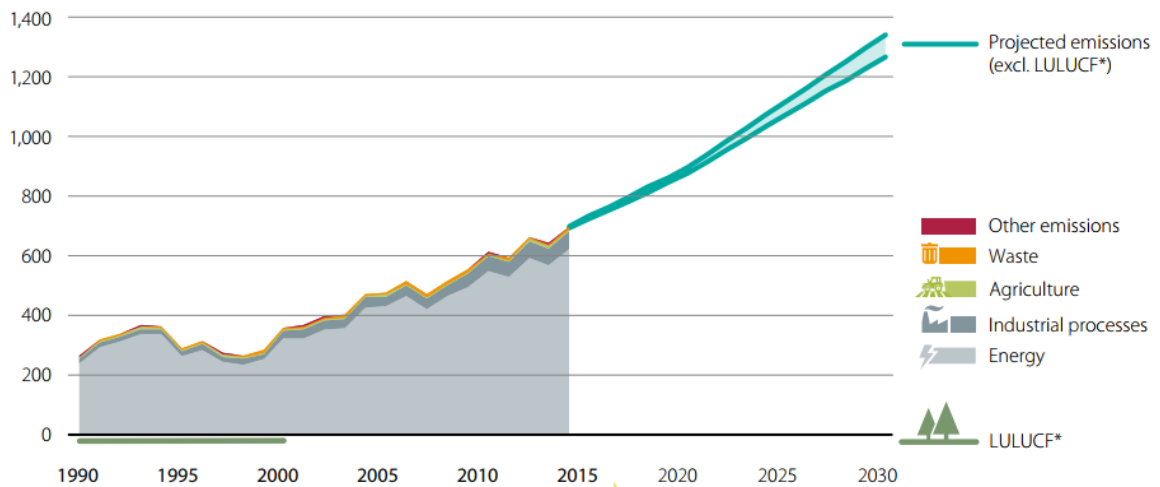


Figure 1: Annual carbon dioxide emissions gross in mega tone across sectors.

1.2 Electrocatalytic water splitting:

Currently, 96% of the global hydrogen production is based on the decomposition of fossil fuels as shown in Figure 2, which are energy-intensive processes and associated with high CO₂ emissions. On the other hand, continuous supply of renewable hydrogen energy via viable economic manner remains a great challenge. One of the most attractive routes being proposed to produce hydrogen in a sustainable way is through water electrolysis. In which, Hydrogen molecules could be produced from water- an abundant and renewable hydrogen raw material through utilizing electrical energy derived from solar, wind or other

renewable resources. Since Electrochemical water splitting is an uphill energy process, demand intensive electrical energy to get pure hydrogen gas. The external electricity used to derive this process is generated from renewable sources such as solar energy and wind power for the sustainable production of hydrogen. Figure 4 shows integrated water electrolyzer to renewable electricity sources and energy conversion process of hydrogen to electricity via fuel cells. The output of the electrolyzer can be stored and can further be consumed in the presence of oxygen to produce electricity. Therefore, production of a zero emission CO₂ energy can be achieved by such coupling system which seems to be the key solution in recent future [8–12].

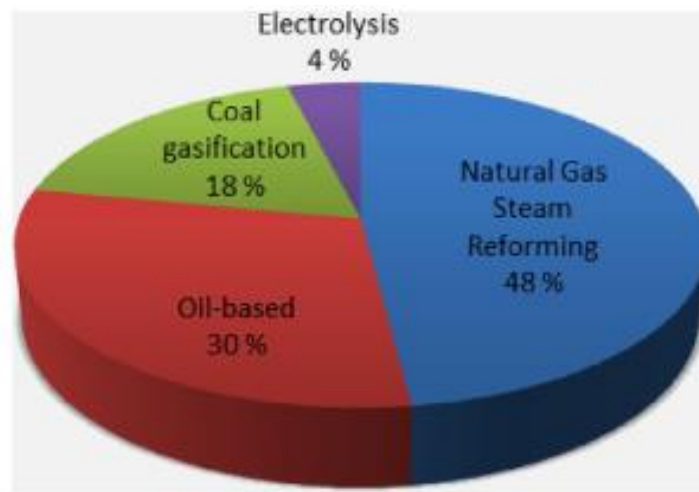
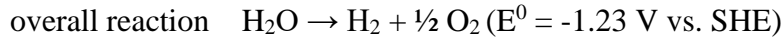


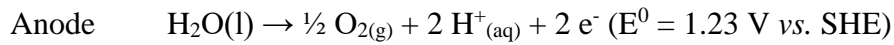
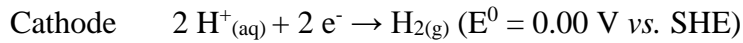
Figure 2: Contributions of production pathways for the worlds' hydrogen yield.

The electrolyzer- a device used to process the electrolytic water splitting is comprised mainly of three components; an aqueous electrolyte, an anode and a cathode (Figure 3). In this electrochemical system, when the external bias applied across the electrodes, water can be dissociated into its primary hydrogen and oxygen molecules.

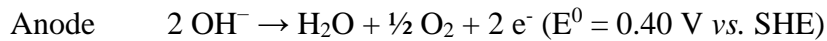
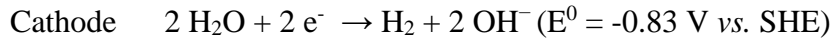
Hence, electrochemical water splitting reactions is divided into two half-reactions, the cathodic hydrogen evolution reaction (HER) and the anodic oxygen evolution reaction (OER), as described by the following equations:



In acidic electrolytes:



In neutral and alkaline solutions



Under standard conditions (STP $\sim 25^\circ \text{C}$, 1 atm), the thermodynamic potential of overall water splitting reaction is found to be (-1.23 V) regardless of the reaction media. Nevertheless, in practice, water electrolysis process always needs higher applied potential than dictated by thermodynamic voltage to derive water splitting with reasonable reaction rates. This extra voltage (known as overvoltage) facilitates essentially the charge transfer to overcome the high activation energy barrier for the formation of reaction intermediates on electrode surfaces. Taking this into consideration, the overall operational potential (E_{op}) to proceed water splitting can be given as follow:

$$V_{\text{op}} = 1.23 \text{ V} + \eta_{\text{a}} + \eta_{\text{c}} + \eta_{\Omega} \quad (1)$$

Where (η_{a}) and (η_{c}) represent the overpotentials at the anode and cathode, respectively. (η_{Ω}) is collective internal resistances of the cell system which involves; solution resistance

as well as contact resistance. For practical water splitting use, the intrinsic activation barriers associated with (η_a) and (η_c) could be lowered by application of effective OER and HER electrocatalysts, respectively. whereas (η_Ω) has to be compensated by an appropriate cell configuration.

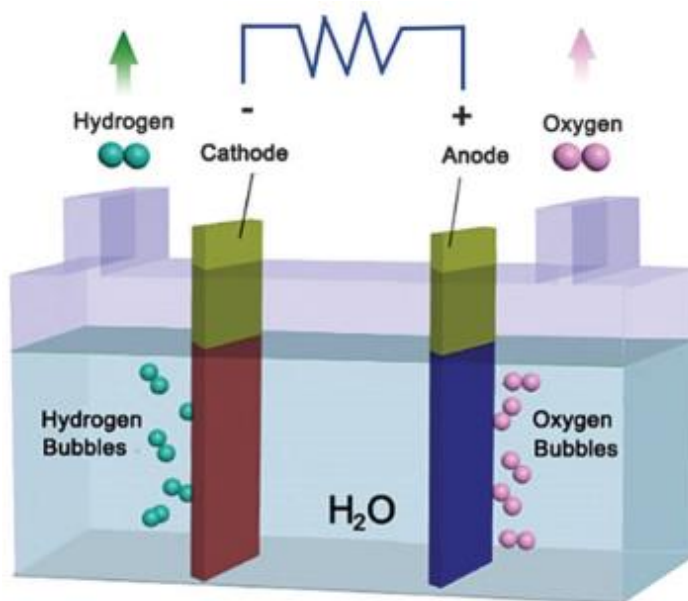


Figure 3: Schematic illustration of water electrolyzer.

To this end, the key issue for research is to develop high-efficient water splitting electrocatalysts, preferably based on low-cost and robust elements in such a way that could lower the overpotentials and improve the cell efficiency. According to previous reports, the minimum overpotentials required by state of the art electrocatalysts to produce a geometric current density of 10 mA (accepted as a metric to evaluate the catalysts performances) for HER and OER in acidic solution are 40 and 300 mV respectively. The above stated current density is indicated the idealized electrochemical activity using 10% efficient photoelectrochemically device that would be required industrially to generate

hydrogen gas, to make the production system more economical. Generally, ideal electrocatalysts should derive HER reaction at overpotentials equal to or less than 100 mV over entire pH solutions (from pH=0 to 14) [10, 13, 14].

Up to date, platinum is the state of the art catalyst for electrocatalytic hydrogen generation due to its high activity, and chemical inertness in acidic media [12]. Thus, the cathodic Platinum electrode is commonly functioned as a benchmark to evaluate the catalytic activities for other electrocatalysts. However, its high price and shortage in the earth's crust suppressed its use for widespread industrial applications. In order to maintain a large-scale production of hydrogen, the cost-effective earth-rich alternatives to Platinum endowed with great catalytic activities and high stabilities would be developed. Conventionally, Nickel based electrocatalysts have been applied for water electrolysis. Nevertheless, the major drawback of Ni electrocatalysts is their vulnerability to corrosion attack in acid solution, that dwindles their function in the proton exchange membrane based electrolyzer [10, 11]. Therefore, to overcome these restricts, more and more attention has been devoted to developing transition metal carbides, nitrides, sulfides, and phosphides as highly efficient HER electrocatalysts [14–17].

The remarkable electrocatalytic activities of these compounds were due to distinct electronic distribution resulted from the insertion of the non-metal atoms in the metal lattice. The considerable activity and robust stability features of these compounds in acidic media nominated them to take place of the precious Pt and platinum group metals in the wide variety of catalytic reactions, involving, hydroprocessing (hydrogenation, hydrodesulfurization and hydrodenitrogenation), Haber ammonia synthesis as well as electrocatalytic hydrogen evolution reaction [16, 18, 19].

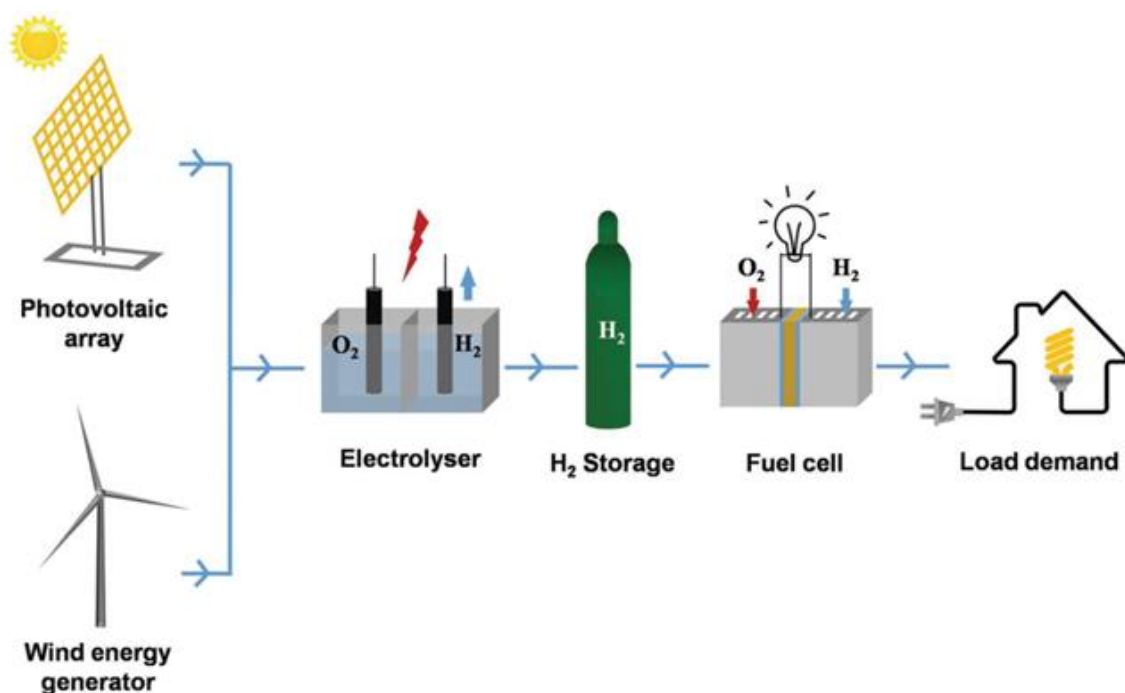


Figure 4: Schematic representation the overall concept of a hydrogen renewable energy system for distributed power generation.

since the electrocatalytic performances of catalysts depend on their surface composition and physio-chemical features such as size, dispersity and morphology, which are predominantly correlated to their synthetic methods.

1.3 Research Objectives:

Based on the preceding premises the main scope of this thesis dealt with the developing of efficient synthesis methods for fabricating low-cost molybdenum based carbides and phosphides as well as cobalt phosphides for hydrogen (H₂) production through water electrolysis in acidic and alkaline aqueous solutions. Firstly, a facile synthetic method based on Al-based MOF namely MIL-53 was used as a confined space for controlled nucleation and growth of Mo₂C nanoparticles on porous carbon for the hydrogen

evolution reaction. Secondly, we developed a versatile simple synthesis approach to improve the dispersity of molybdenum carbide nanoparticles supported on multiwall carbon nanotubes substrate via the oxalate-complexation route, where the oxalate-molybdenum complex obtained through wet chemistry was carbonized under elevated temperature into Mo₂C/CNT. Similarly, high dispersity of MoP nanoparticle on CNT surface was achieved by heating the same oxalate-molybdenum in presence of phosphoric acid. This study affirmed the effectiveness of such method to produce ultra-fine and uniformly well-dispersed electrocatalysts onto the surface of CNT. Consequently, an ultra-improved performance was observed. Finally, CoP/CNT composites were also prepared through low-temperature phosphorization treatment. The hexamethylenetetramine was used as a shaping agent, facilitated the emerging of interconnected hollow CoP nanoparticles, which optimized the charge transfer kinetics and lead to remarkable performance and stability for HER. The catalytic activity of above composites was evaluated in both acidic and basic media and compared with the performance of recently reported electrocatalysts. This dissertation presented the efficiency and originality of these developed methods to produce different composites of carbides and phosphides, which could find use accordingly in a wide range of applications in material chemistry, supercapacitors and lithium ion batteries. More specifically, the thesis has the following objectives:

- 1- To fabricate highly efficient and durable molybdenum carbide (Mo₂C) on mesoporous carbon for catalytic hydrogen evolution.
- 2- To fabricate highly efficient and durable molybdenum carbide (Mo₂C)/and molybdenum phosphide (MoP) on CNT for catalytic hydrogen evolution.

- 3- To fabricate highly efficient and durable cobalt phosphide (CoP) on CNT for catalytic hydrogen evolution.
- 4- To characterize the as prepared materials by standard techniques.
- 5- To study and evaluate their electrochemical activity for hydrogen evolution reaction (HER) in both acidic and alkaline solutions.

CHAPTER 2

Literature review

2.1 Transition metals based carbides and phosphides compounds:

The incorporation of carbon and phosphorous atoms into the transition metal lattice generates an interesting class of materials referred to as carbides and phosphides, respectively. These interstitial compounds are endowed with unique physiochemical properties, they are refractory compounds, demonstrate extreme strength and hardness, display high resistance to corrosion. They are characterized by their conductivity for electrical and thermal energy, and they possess distinct optical, magnetic, electronic, and catalytic characteristics which could make them inexpensive alternative catalysts to the platinum group metals in various application in material science and hydroprocessing catalysis [20–23].

2.1.1 Crystal Structure:

In interstitial metal carbides as illustrated in Figure 5, carbon occupies specific interstitial sites of metal lattice to form three crystallographic structures: face-centered cubic, hexagonal closed packed and simple hexagonal. Despite the physical and chemical characteristics of phosphides closely resemble those of carbides, their structures are substantially different since phosphorous atom has a larger radius (0.109 nm) than a carbon atom. Thus, transition metal phosphides generally adopt Trigonal prismatic structure (Figure 6) [8, 24]. Basically, geometric and electronic factors can predict the crystal structure of transition metal carbides. With respect to geometric consideration, Hagg

provides an empirical rule, which demonstrates that the interstitial structures can be formed when the ratio of atomic between nonmetal atom to metal atom is less than 0.59. The electronic aspect has been elucidated utilizing Engel–Brewer theory, states that, the observed structure depends on the number of sp electrons. The metallic arrangement in transition metal carbides substantially differs from that of the parent counterparts. The pure metal possesses a bcc structure, while its carbides are hcp. the structure changes from bcc to hcp to fcc in accordance with increasing the amount of sp electrons [7, 8].

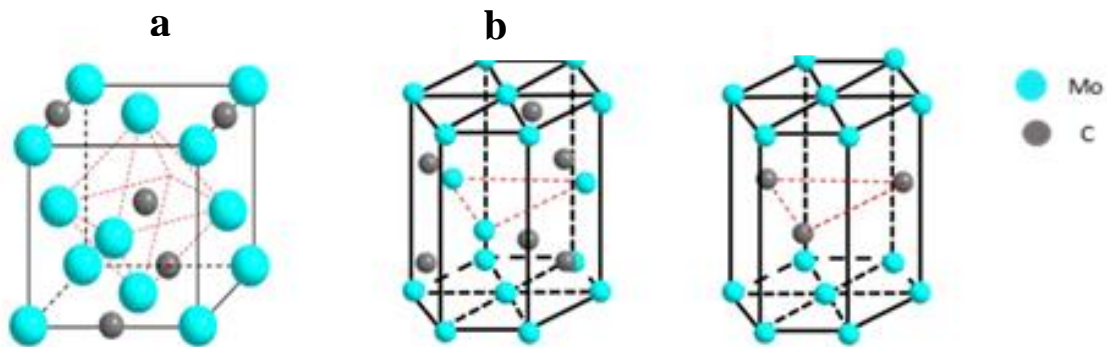


Figure 5: Typical crystallographic structures of transition metal carbides. a) face-centered cubic, b) hexagonal closed packed and c) simple hexagonal.

2.1.2 Bonding in Carbides and phosphides compounds:

Carbides and phosphides can be classified into 3 distinct categories according to the type of chemical interaction between the nonmetal atom and the metallic center: covalent compounds, formed when the metallic center has a high electronegativity; saline compounds, are characterized by ionic bonding and, the metallic compounds, exhibit metal-metal bonding.

transition metal carbides are considered as the most important member of the binary carbides family. The bonding in these compounds is a mixture of metallic, covalent and ionic components. While transition metal phosphides exhibit a combination of metallic and covalent bonding [24, 25].

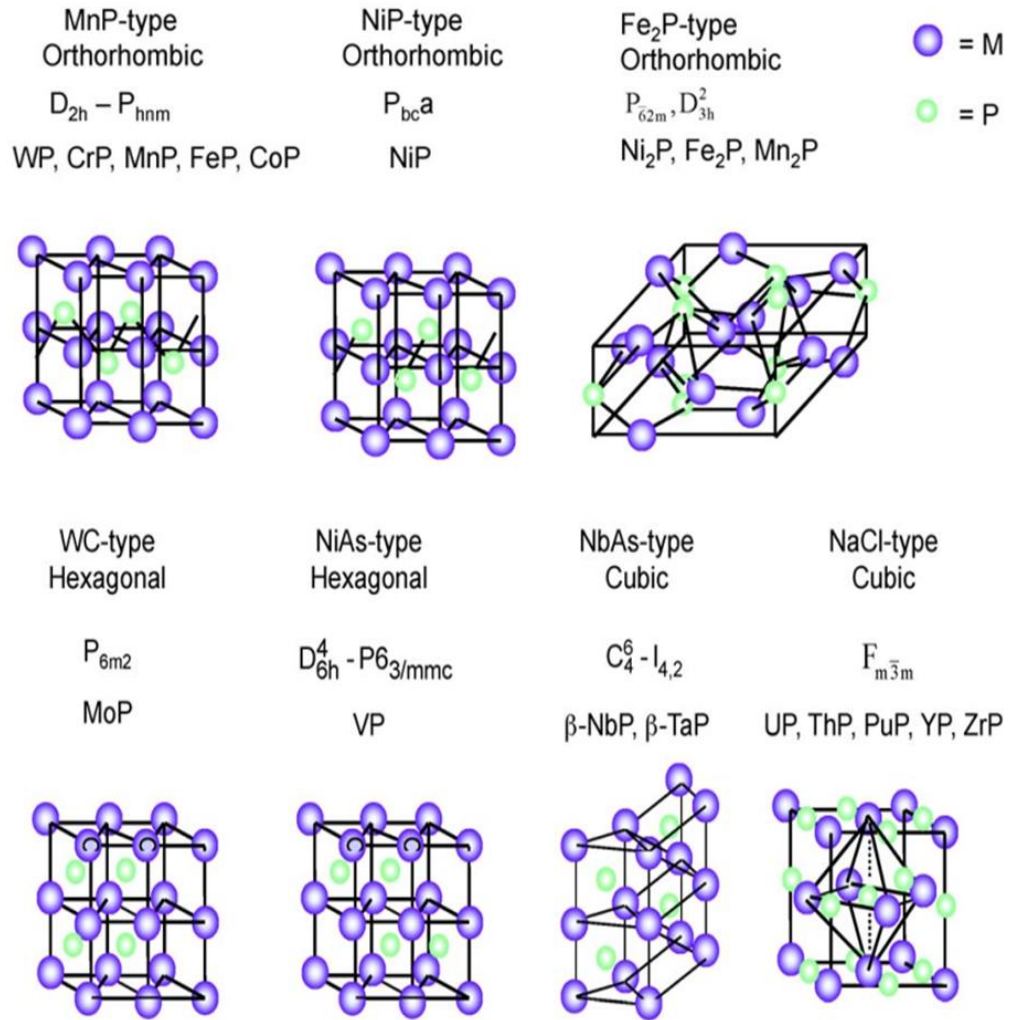


Figure 6: Common crystal structures of transition metal phosphides.










		<u>Carbon affinity</u>											<u>Carbide type</u>					<u>Structure</u>						
		 Strong		 Weak		 Covalent		 Saline		  Metallic		 Simple		 Complex		 Only under extreme conditions								
1	2	3	4	5	6	7	8	9	10	11	12	13	14	15	16	17	18							
1	H																							
2	Li	Be																						
3	Na	Mg																						
4	K	Ca	Sc	Ti	V	Cr	Mn	Fe	Co	Ni	Cu	Zn	Ga	Ge	As	Se	Br	Kr						
5	Rb	Sr	Y	Zr	Nb	Mo	Tc	Ru	Rh	Pd	Ag	Cd	In	Sn	Sb	Te	I	Xe						
6	Cs	Ba	*	Hf	Ta	W	Re	Os	Ir	Pt	Au	Hg	Tl	Pb	Bi	Po	At	Rn						

Figure 7: Common metal Carbides throughout the periodic table.

2.2 Transition metal carbides as (HER) electrocatalysts:

Figure 7 exhibits the Carbides of early transition metals in Groups VI such as tungsten (W) and molybdenum (Mo), which are the most promising substitutes for hydrogen evolution reaction electrocatalysis. Relative to work of Levy and M. Boudart in 1973, tungsten carbides have been shown a Platinum-like catalytic character due to its analogous d-band structure to platinum. The first exploration of molybdenum carbide as HER electrocatalyst was conducted by Hu's group in 2012, they discovered that the bulk Mo_2C possess a high activity and stability for HER in either, in acidic or alkaline media [26, 27]. There are many conventional processes to synthesize transition metal carbides including solid-gas reaction (carbon source is carbonaceous gases), solid-solid reaction (carbon source is in the form of solid materials), solid-liquid reaction (carbon precursor is in the solution state), chemical vapor deposition (CVD), microwave assisted method and plasma method. Traditionally, molybdenum carbide is fabricated using temperature

programmed reduction method (solid-gas reaction). However, such methods suffer from many downsides such as high energy consumption, large particle size, low surface area, an incomplete reaction which resulted in carbon char contaminations, which block the pores and reduced the number of active sites. Therefore, the electroactivity of resultant carbides would be dramatically deteriorated [8, 28, 29].

To address these problems, typically many tactics have been reported in open literature. The efficient strategy for instance, is to tailor/and reduce the catalyst particle size in nanoscale meter, or to construct the material with various nanostructures or architectures morphologies to compromise the loss of active surface areas and speed up the charge and mass transport. Aside from that, is to utilize a nonporous carbon matrix to enhance the conductivity of the composite and to improve the dispersion of the catalyst [30, 31]. Wan et. al synthesized nanostructured Mo_xC_y by direct pyrolysis of amine- accommodating molybdenum based organic-inorganic hybrid materials. The generated products exhibited various morphologies including nanowires, nanorods, nanoflakes, nanospheres, and micro-flowers (figure 8) [32]. Similarly, Liao' group reported nonporous molybdenum carbide nanowires with the 1D morphology of several micrometers in length and 80–120 nm in width by annealing a MoO_x /amine hybrid precursor under the inert environment (figure 9). This electrocatalyst displays outperform HER activity in 0.5M H_2SO_4 , only 130 mV overpotential is required to drive 10 mA/cm^2 with a Tafel slope of 53 mV dec^{-1} and further it demonstrated long-term stability under chronoamperometric experiment. The outstanding activity of this catalyst was attributed to its high surface area ($63.9 \text{ m}^2 \text{ g}^{-1}$), nanoporosity and nanosized crystallites [33].

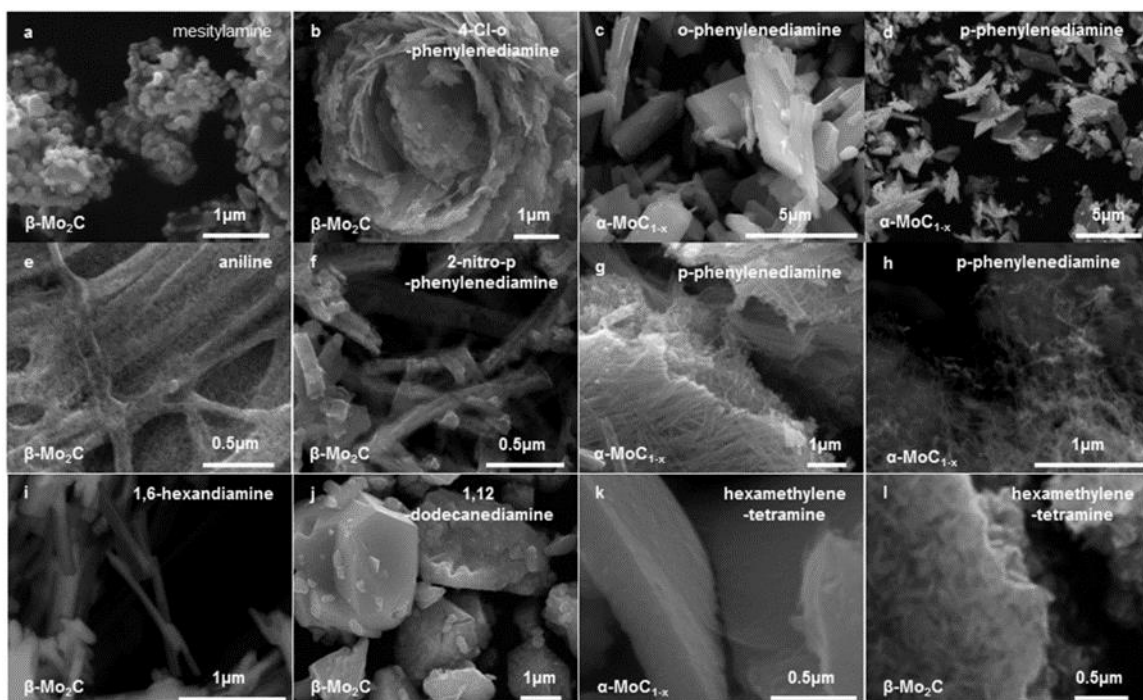


Figure 8: SEM images of, (a) β - Mo_2C synthesized by mesitylamine at 750 °C (b) β - Mo_2C synthesized by 4-Cl-o-phenylenediamine, at 675 °C (c) α - MoC_{1-x} synthesized by o-phenylenediamine, at 625 °C (d) α - MoC_{1-x} synthesized by p-phenylenediamine, at 675 °C (e) β - Mo_2C synthesized by aniline with 4 : 1 amine : Mo ratio, at 675 °C (f) β - Mo_2C synthesized by 2-nitro-p-phenylenediamine, at 875 °C, (g) α - MoC_{1-x} synthesized by p-phenylenediamine with 4 : 1 amine : Mo ratio, at 675 °C (h) α - MoC_{1-x} synthesized by p-phenylenediamine with 8 : 1 amine : Mo ratio, at 850 °C (i) β - Mo_2C synthesized by 1,6-hexanediamine, at 675 °C, (j) β - Mo_2C synthesized by 4-nitro-o-phenylenediamine, at 850 °C (k) α - MoC_{1-x} synthesized by hexamethylenetetramine, at 850 °C, (l) β - Mo_2C synthesized by hexamethylenetetramine, at 900 °C.

The electrocatalytic performance of carbide materials depends on their surface composition and conditions which are closely related to their synthetic methods. carbon nanotubes (CNT) supported Mo_2C nanoparticles composite was synthesized by Muckerman et al., this study showed that CNTs has dual roles; can act as both a carbon source for the reaction and a supportive matrix as well. These materials were prepared from carbon-containing molybdate precursor by the carburization process. This conjunction with

carbon substrate promotes the formation of the small particle (particle size 7–15 nm) without agglomeration, which is desired to bring about more exposed active sites and enhanced electronic conductivity.

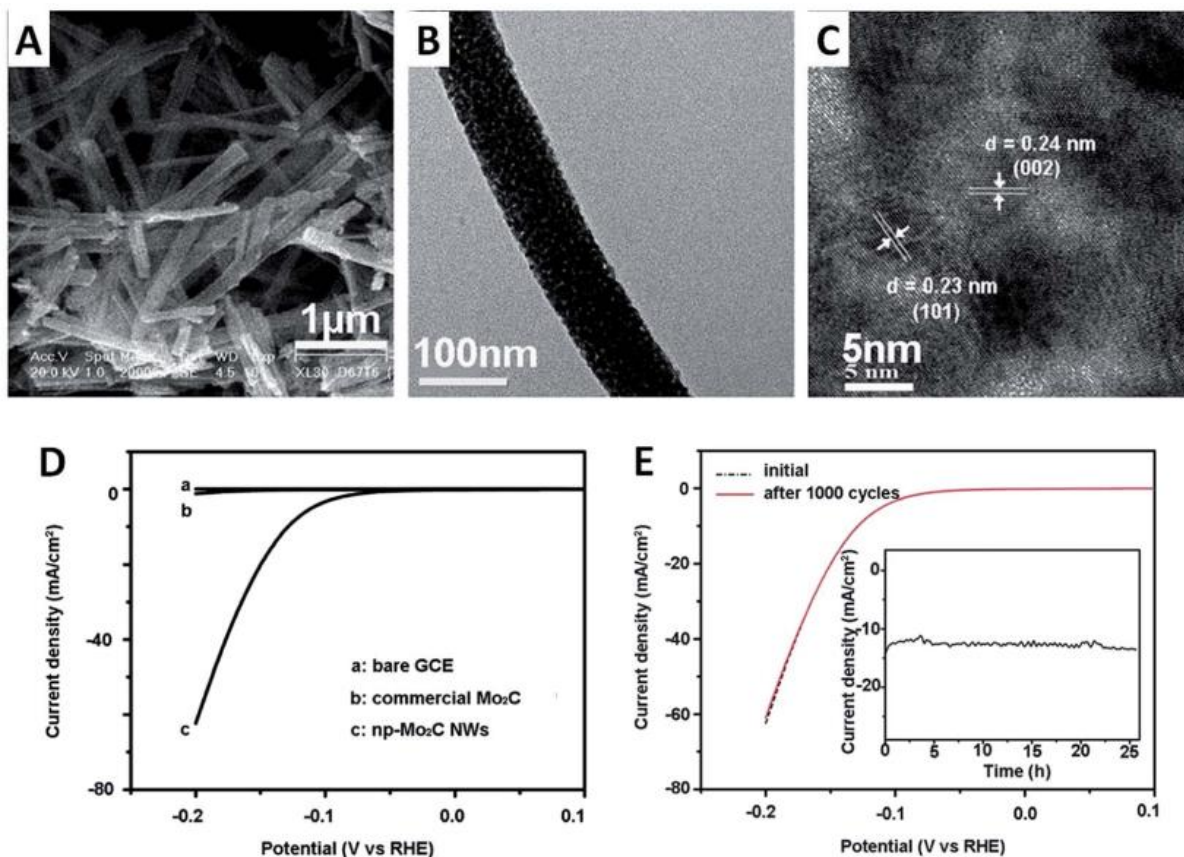


Figure 9: (A) SEM image and (B and C) TEM images of nanoporous Mo₂C nanowires. (D) Polarization curve of np-Mo₂C NWs compared with commercial Mo₂C and bare glassy carbon electrodes in 0.5 M H₂SO₄. (E) Polarization curve of np-Mo₂C NWs before and after 1000 cycles. The inset shows its chronopotentiometry response at $\eta=130$ mV.

The as-prepared composite catalyst demonstrated superior electrocatalytic activity toward HER with an overpotential of 152 mV at 10 mA cm⁻² and small Tafel slope of 55.2 mV [34]. Similarly, Mo₂C nanocrystals anchored on CNT-graphene composite was demonstrated by Lee's group, performed highly current density of 10 mA cm⁻² with a

modest overpotential of 130 mv. The study showed that CNT-graphene hybrid in 3D-structure was responsible for preventing aggregation of nanocrystals, offering a large contact area with the electrolyte, resulting in the fast charge transfer [35].

In addition, the coupling of Mo₂C nanocrystals and graphene materials exhibited remarkable activity and stability due to the intimate interactions between Mo₂C and carbon sheet [36].

2.2.1 Metal-organic frameworks (MOFs)-derived porous carbides:

In recent years, metal-organic frameworks (MOF) as an emerging family of crystalline porous material composed of metal ion and organic ligand by stable coordination bonds, have aroused a great research interest because of their ultra-high surface areas (from 1000 to 10000 m² g⁻¹) and their potential to tune the size, morphology, and porosity. Thanks to these unique features, MOFs show promising alternative in the wide range of applications, including; gas storage [37], Oxygen reduction reaction [38], oxygen evolution reaction [39], hydrogen evolution reaction, supercapacitors [40], sensing [41], water treatment [42] and drug delivery [43].

MOFs can be used both as precursor, template and/or support to drive the synthesis of transition metal oxides [44], carbides [45], phosphides [46], nitrides [47], sulphides [48] and selenides [49]. By taking carbides into account, the metal component in the MOF is readily converted to carbide in the presence and /or aiding of pyrolytic carbon that generated from organic ligands during the controlled carburization conditions. In this regard, Li et al. used a mixture of Polyoxometalate-based metal organic frameworks (POMOFs) namely PMo₁₂@MIL-100 (Fe) and melamine as precursors to derive synthesis

of N, P co-doped graphitic carbon supported $\text{Fe}_3\text{C}/\text{Mo}_2\text{C}$ ($\text{Fe}_3\text{C}/\text{Mo}_2\text{C}@\text{NPGC}$) (Figure 10). This composite was formed by heating under inert environment and the resultant hybrid revealed exceptional catalytic activity and stability as HER electrocatalyst. which was originated from many factors; firstly, the synergetic effect of co-dopant nitrogen and phosphorous atoms into carbon layer, resulted in increased active sites density. Secondly, the presence of carbon layers in the product not only prevents the agglomeration and corrosion of the $\text{Fe}_3\text{C}/\text{Mo}_2\text{C}$ nanoparticles, but also facilitates electron transformation from the embedded $\text{Fe}_3\text{C}/\text{Mo}_2\text{C}$ into the outer carbon layers. Lastly, the mesoporous structures of $\text{Fe}_3\text{C}/\text{Mo}_2\text{C}@\text{NPGC}$ can accelerate the mass transport and enhance the conductivity [50, 51].

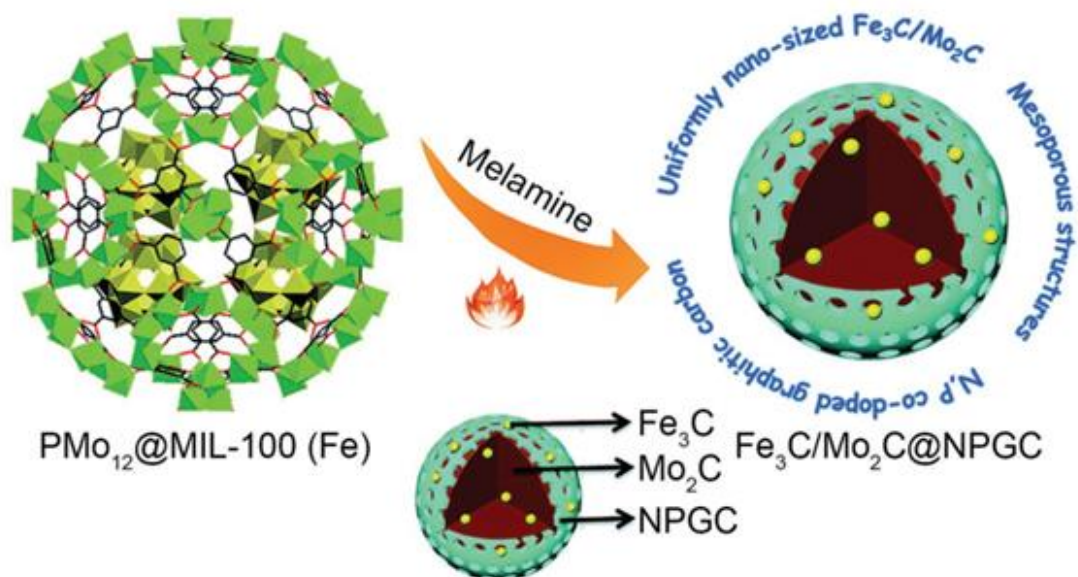


Figure 10: Synthesis of the $\text{Fe}_3\text{C}/\text{Mo}_2\text{C}@\text{NPGC}$ nanohybrid derived from Polyoxometalate-based metal–organic frameworks.

Lou et al. synthesized mesoporous molybdenum carbide nano-octahedrons (MoC_x) by direct pyrolysis of a Mo-based MOFs at 800°C under N_2 gas stream. The TEM images

confirmed its continuous structure porosity as well as the growth of many tiny nanocrystallites on the surface of MoC_x nano-octahedrons. And the obtained catalyst is considered as an efficient electrocatalyst for HER with 142 and 151 mV overpotentials to drive 10 mA cm^{-2} current density in acidic and basic solutions, respectively [52]. One more facile strategy to avoid the lacks in available metal-rich MOFs and control over the morphology of the MOF-derived porous carbon compounds during the heating process, is to load the secondary transition metal into MOF-derived carbon template by an impregnation method [53]. Following this, Yang's group prepared a MoS_2 -based 3D nonporous composite (MoS_2 /3D-NPC) via an impregnation/incipient approach. In this approach, first, 3D nanoporous carbon (3DNPC) was obtained from the Al-based MOF precursor (Al-based porous coordination polymer) by annealing at 800°C followed by Al leaching process. then, the confined growth of MoS_2 nanosheets in the pores of 3D-NPC was conducted by in situ solvothermal reduction of $(\text{NH}_4)_2\text{MoS}_4$, producing a MoS_2 -based 3D hierarchical structure material (figure 11) [54].

2.2.2 Transition metal phosphides as HER electrocatalysts:

It's well known that transition metal phosphides have long been used for hydrogenation catalysis, particularly hydrodesulfurization (HDS). Recent studies revealed that hydrogen evolution reaction is analogous to hydrodesulfurization reaction, where, both of which were undergone a reversible adsorption/desorption of hydrogen atom in the catalytic process. This relation widened the scope search for a novel HER electrocatalyst. In 2013, Ni_2P has been first reported as a promising candidate for HER, and achieved a much better activity than the state-of-the-art MoS_2 [55].

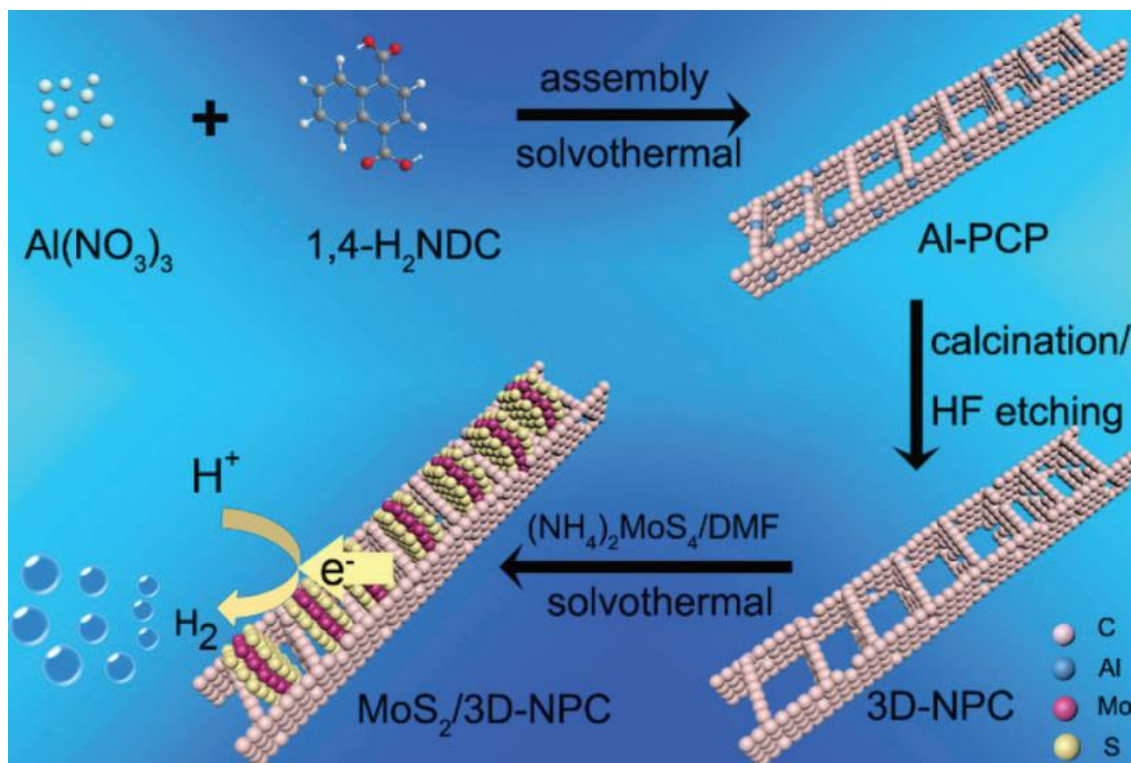


Figure 11: Schematic representation of the confined preparation of MoS₂/3D-NPC.

Commonly, two approaches were applied in literature to fabricate nanostructures transition metal phosphides; the Solution-phase reaction and gas-solid reaction. The first approach, based on the Solution-phase to synthesize phosphides using tri-octyl phosphine (TOP) as phosphorus source in organic solvent was established. TOP is widely utilized as a favored phosphorus source. In situ, thermal decomposition of such precursor can take place at a moderate temperature around 300 °C in presence of various metal precursors such as; metal-based acetylacetonates, oxides and carbonyls, or metal nanoparticles. Then these precursors can completely be transformed into phosphides [55–59]. While tri-octyl phosphine mediated solution-phase method can be used for the preparation of metal phosphides with a diversity of morphologies and crystal phases. On the other hand, this organic phosphine is highly flammable and corrosive. Besides, the low yield by this route

as well, impedes its application to the large-scale production of phosphide catalysts [60, 61, 64].

Secondly, gas-solid reaction, involves the high-temperature program reduction of metal phosphate precursor to decompose the strong bond of P-O and form a metal-phosphorus bond. In this method, a mixture of $\text{NH}_4\text{H}_2\text{PO}_4$ (as inorganic phosphorous source) and solid metal source are undergone to hydrogen gas carburization reduction at a temperature range from 400 to 1000 $^{\circ}\text{C}$. Based on this, Wang et al. reported preparation of well crystalline Mo_3P and MoP by heating a mixture of stoichiometric amounts of $(\text{NH}_4)_6\text{Mo}_7\text{O}_{24} \cdot 4\text{H}_2\text{O}$ and $(\text{NH}_4)_2\text{HPO}_4$ at 650 $^{\circ}\text{C}$ and 800 $^{\circ}\text{C}$, respectively. The performance of MoP was evaluated, and it revealed efficient HER activity with a current density of 30 mA cm^{-2} at 180 mV overpotential (Figure 12). whereas Mo_3P showed considerably subordinate catalytic performance. The theoretical calculations proved such a remarkable HER performance is attributed to P terminated plane on (001)- MoP , which realized an appropriate ΔG_{H}^0 with value approaches to zero [65].

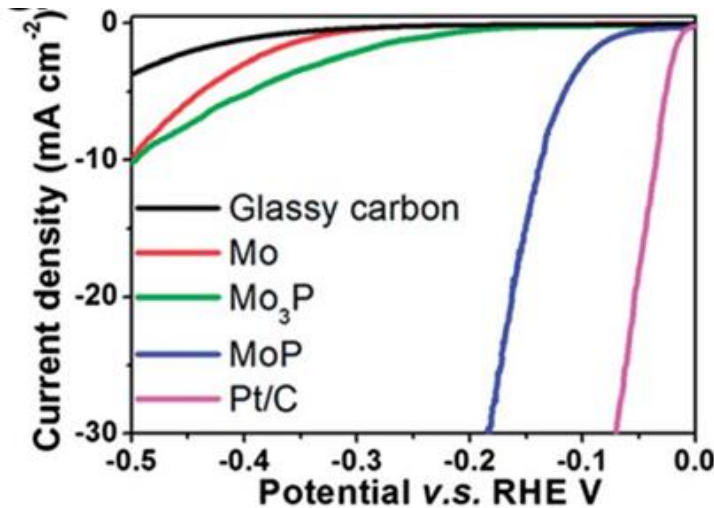
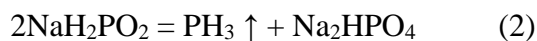


Figure 12: LSV measurements of Mo, Mo_3P and MoP in concentrated acid solution (0.5M H_2SO_4) To avoid the agglomeration of MoP particles during a thermal treatment (sintering effect).

Sun et al. suggested introducing of citric acid as the chelating agent. Which leads to form a closely interconnected network of MoP nanoparticles with BET surface area of $143.3 \text{ m}^2 \text{ g}^{-1}$, which was about three times higher than that of MoP nanoparticles prepared in absent of citric acid. Such a significant enhancement in the specific surface brought about a spectacular improvement in HER activity. The generated current densities were measured at an overpotential of 200 mV to be 100 mA cm^{-2} and 1.7 mA cm^{-2} for MoP synthesized with and without chelating ligand, respectively [66]. Despite the high-temperature route was used extensively to synthesize the transition metal phosphides. it nevertheless, can induce the sintering process, usually resulting in bulky phosphide structures with a large crystal size [67].

Another mild and facile kind of gas-solid phase reaction, including a direct phosphidation of metal oxides, chlorides, hydroxides, metal-organic frameworks (MOFs), and other metal compounds source by sodium hypophosphites (NaH_2PO_2). In details, by heating above 250°C temperature, sodium hypophosphite can be decomposed disproportionally to release phosphine gas, for further reaction with solid metal precursors under protective nitrogen gas flow to yield the phosphides. The equation of decomposition was shown as follows:



In this respect, Feng et al. synthesized polydispersed Ni_2P nanoparticles of 10–50 nm in size. The as-prepared electrocatalyst exhibited comparable HER activity to that reported by Schaak et al. and obtained by the TOP method [64]. Jiang et al. prepared CoP with several nano-architectures, involving; nanowires, nanosheets and nanoparticles via the

low-temperature phosphatization of different nanostructured cobalt oxides with the pristine morphologies remained well preserved (Figure 13). In this procedure, sodium hypophosphite and cobalt oxide (Co/P = 1: 5 ratio) were put sequentially at a distance in one sealed holder with sodium hypophosphite at the upstream side of the furnace. Then, the samples were annealed for 2 h at 300 °C in gaseous Ar stream [61, 62, 63, 64, 69].

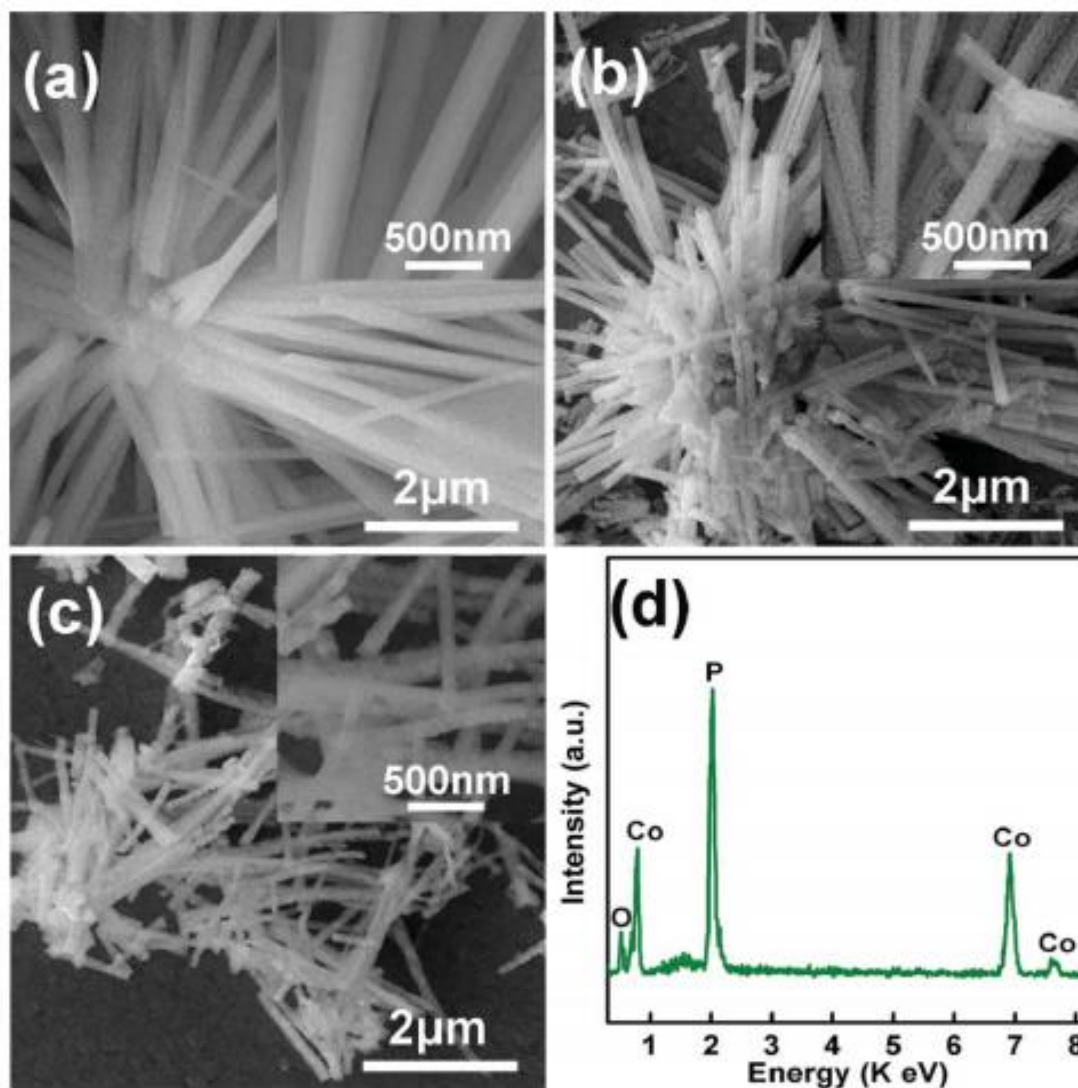


Figure 13: Scan electron microscopy images show the morphologies from starting material of cobalt oxide NWs (a), and Co₃O₄ NWs (b) to the final product of CoP NWs (c). EDX mapping of CoP NWs. (d).

2.2.3 Carbon nanotubes as a support for HER electrocatalysts:

Since, Iijima's recognition of carbon nanotubes in 1999, CNTs as emerging type of carbon material have received a great interest due to their unique properties; first of all, CNTs have excellent electrical conductivity, estimated to be around 5000 S cm^{-1} . Secondly, they possess a high specific surface area with distinct mesoporous structures range from 2-50 nm, which makes them highly electrochemically accessible to the electrolyte. Besides these, CNTs also have a good thermal conductivity, thermal stability and high mechanical strength. By virtue of these attractive features, CNTs exhibit potential applications in a diversity of areas, such as sensors, nanoelectronics devices, organic photovoltaic cells, catalysts support, fuel cells and batteries [69–72].

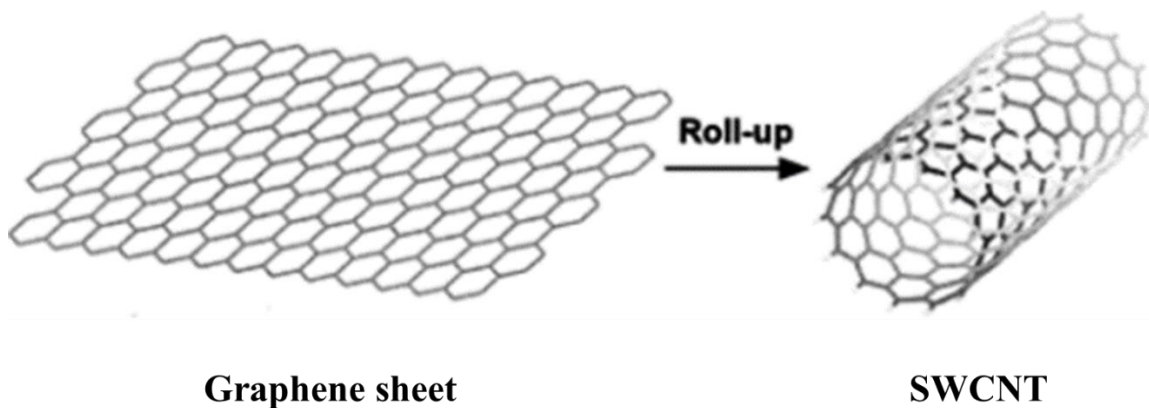


Figure 14 Schematic representation of the carbon nanotube formation by rolling up a 2D graphene Sheet.

CNTs can be viewed as seamless cylinders composed of one or more curved layers of graphene. Depending on the layers of curved graphene, CNTs can be classified as

SWNTs, which compose of a single layer of graphene sheet seamlessly rolled up into a cylinder form, and MWNTs which consist of additional concentric tubes around the SWNT core [73].

So far, only six systems of transition metals phosphides namely; Fe, Co, Ni, Cu, Mo and W based phosphides have exhibited promising HER performances. However, most of these catalysts have been suffering from low electric conductivity and deficiency in the number of active sites. Therefore, the introduction of nano-carbon supports into metal phosphides can sort out lack of conductivity and textual properties. CNTs have been emerged as adaptable potential candidates to support phosphides electrocatalysts for hydrogen production. The current studies demonstrated that CNTs couldn't only enhance the electrical conductivity, but it could increase the dispersion of active phases due to their huge surface area [74, 75].

CHAPTER 3

Metal organic framework-guided growth of Mo₂C embedded in mesoporous carbon as high-performance and stable electrocatalyst for hydrogen evolution reaction

3.1 Introduction:

The surge in the field of renewable energy aiming to develop clean energy technology is continuing to rise. The quest for an H₂-based economy derived from non-fossil resources remains at the forefront of future fuels. During the past few decades, there has been intense research on the use of electrical energy to produce H₂ in energy efficient and environmentally benign way [76–79]. Electrocatalytic hydrogen generation via water electrolysis provides an important alternative to that extracted from hydrocarbon resources.

The technological development of water electrolysis to achieve a high flow rate of hydrogen is essentially decelerated by the requirement of high overvoltage. Development of catalyst that can lower the overpotential for hydrogen generation is the cost-determining factor of overall electrocatalytic process. Hence, one of the most crucial components which could revolutionize H₂ production is the design and development of a robust electrocatalyst that can efficiently split water at the overpotential as low as possible. Currently, platinum (Pt) is known as the state-of-the-art electrocatalyst for hydrogen evolution reaction (HER) and oxygen reduction reaction (ORR). However, due to high cost and its scarcity, research focus shifted to precious-metal-free based materials for efficient HER reaction [60, 80, 81]. Consequently, a wide variety of materials consisting of non-precious metals such as, metal

carbides (Mo_2C [34, 82, 83], WC [84], [85]), metal sulfides (MoS_2 [30], [86], WS_2 [87, 88] and CoSe [89, 90]) metal phosphides (Ni_2P & Ni_5P_4 [91–93], Cu_3P [94] and FeP [95, 96]), metal nitrides ($\text{Co}_{0.6}\text{Mo}_{1.4}\text{N}_2$ [97] and NiMoN_x/C [98]), WO_x -Carbon [99], Ni_3Se_2 Nanoforest/Ni Foam [100] and so forth, have been explored [101–105]. Noticeable reduction in overpotential of several new nonprecious metal electrocatalysts has been achieved [79].

To this end, due to unique d-band electronic structure, the Mo-based electrocatalysts, such as Mo_2C and MoS_2 , have been the subject of intense investigation for electrochemical hydrogen evolution under harsh acidic or basic conditions. Progressively, such electrocatalysts are showing platinum-like catalytic activity for HER reaction. Yet, functional and robust catalysts operating with reasonable current densities (J) at low overpotentials in water are scarce [106-109].

It is generally accepted that achieving control of the architecture and composition of nanoscale materials could lead to the development of new materials and systems with enhanced physico-chemical properties. The potential for success lies in the appropriate tailoring and engineering of the nanomaterials. Since electrochemical hydrogen evolution is a predominantly surface-dictated phenomenon, shape, size, interface, porosity (high surface area and active sites), and composition are highly effective factors among others in enhancing the H_2 evolution and decreasing the overpotential. In addition, it has been increasingly documented that the electrocatalytic activity of Mo_2C also depends on the type of carbon support and the extent of dispersion of active sites on its surface. Coupling between active catalysts and support may induce unique metal-support-interaction which may ultimately influence various phenomena such as the interfacial equilibrium,

adsorption and/or desorption of reactive species and their interaction with electrocatalysts surface, electrical conductivity, and so forth. For instance, Chen et. al., demonstrated that Mo₂C supported on carbon nanotube showed higher activity as compared to that of supported on carbon black (XC72) [34]. Furthermore, Mo₂C/CNT was found to be highly stable under applied experimental conditions. Similarly, mesoporous graphitic carbon nitride has also been used as a reactive template to prepare molybdenum carbide-carbon nanocomposites for electrochemical hydrogen evolution [106]. In another recent study, Zhang et. al., reported the synthesis of porous one-dimensional Mo₂C supported on amorphous carbon as highly efficient and durable electrocatalysts for hydrogen generation in acidic media [107]. Several examples could be presented here underlining the fact that carbon support endowed with fairly dispersed active catalysts on the surface plays a vital role in determining electrocatalytic activity.

Recently, synthesis of porous molybdenum carbide for electrocatalytic H₂ evolution has been demonstrated by using a Cu-based MOF [HKUST-1; Cu₃(BTC)₂(H₂O)₃] with Mo-based Keggin-type POMs (H₃PMo₁₂O₄₀) (NENU-5) and Mo₃(BTC)₂ [52, 108]. In another recent study, nickel-carbon-based electrocatalyst was prepared by carbonization of Ni-based metal-organic frameworks followed by electrochemical activation for HER reaction [109]. MOFs are relatively a new class of materials and availability of MOFs with desired metals is limited. Developing approach which could address this gap seemed attractive and significant. Herein, we demonstrate a MOF-steered novel strategy to synthesize β -Mo₂C embedded in porous carbon as electrocatalyst for H₂ evolution reaction. This

approach is based on the impregnation chemistry; desired metal source (molybdenum chloride in this case) was dispersed and impregnated in the texture of Metal Organic Framework (MIL-53(Al)), unlike previous studies in which molybdenum- or Ni-based metal-organic frameworks were synthesized and employed. Microporous matrix in the MIL-53(Al) was used as a confined environment for the guided nucleation and growth of Mo₂C nanocrystallites. The rationale behind using the porous frameworks of MIL-53(Al) was to preclude agglomeration and coalescence of Mo₂C which are predominant under normal ambience.

The catalyst was thoroughly characterized by various techniques, and electrocatalytic property for HER reaction was studied. As-prepared Mo₂C/C nanocomposite showed stable and highly efficient electrocatalytic hydrogen evolution in alkaline (1M KOH) aqueous media. Furthermore, electrocatalytic performance of Mo₂C/C was compared with that of commercial electrocatalyst Pt/C and Mo₂C/XC72.

3.2 Experimental:

3.2.1 Synthesis of Metal Organic Framework (MIL-53(Al)):

Synthesis of MIL-53 (Al) was carried out by the hydrothermal method [110]. Al(NO₃)₃·9H₂O, 1,4-benzene dicarboxylic acid and deionized water was placed in a Teflon-lined steel autoclave and heated at 220 °C for specific time duration. After completion of the reaction, the resulting white product was filtered, washed with distilled water, dried overnight at 90 °C and activated.

3.2.2 Synthesis of Mo₂C/C electrocatalyst:

In a typical synthesis, a predetermined amount of molybdenum source (MoCl₅) was dissolved in anhydrous isopropanol, and the solution was kept under stirring for 2 h. After complete dissolution of MoCl₅, a measured amount of MOF was suspended and kept under stirring for 12 h to ensure complete impregnation of Mo source into MOF structure. The weight ratio of Mo:C was adjusted to 40:60. As the MIL53(Al) is sensitive towards moisture, as-synthesized MOF samples were heated at 120 °C overnight and was suspended immediately into the reaction solution to avoid any moisture adsorption which could affect the molybdenum impregnation and hence the activity. The solvent, isopropanol, was then evaporated under a vigorous stirring, leaving behind a gel-like product. The resulting product was dried in oven and finally carburized in a tubular furnace in the presence of CH₄ flow at desired temperature (with a heating rate of 1.5 °C/min) for 2 h. The flow of gas was maintained 100 mL/min with mass flow controller (Alicat). After reaction, the black product was collected and subjected to NaOH treatment for Al removal. For Al removal, the product was stirred in a 4.0 M aqueous solution of NaOH and washed thoroughly with deionized water. This process was repeated several times to ensure complete removal of Al. Finally, the obtained product was dried and used as electrocatalyst for HER reaction. Mo₂C/XC was synthesized following identical conditions, but XC72 carbon was used instead of MOF as a support.

3.2.3 Characterization:

Morphological and detailed microstructural attributes of the materials were discerned with the aid of field emission scanning electron microscope (FE-SEM, Tescan

Lyra-3), transmission and high-resolution transmission electron microscope and selected area electron diffraction (TEM/HR-TEM, FEI Tecnai TF20) (SAED). Other techniques employed for characterization of the samples were: X-ray diffractometry (XRD, Rigaku MiniFlex), BET surface area analyzer (Micromeritics ChemiSorb 2750), and X-ray photoelectron spectroscopy (XPS, Thermo Scientific ESCALAB 250Xi).

3.2.4 Evaluation of electrocatalytic activity:

A suspension consisting of electrocatalyst (10 mg), water and isopropanol (30% V/V) and 37 μL of 1.66 % wt. Nafion[®] was prepared and sonicated for approximately 30 min to obtain a homogeneous ink. A measured amount (16 μL) of suspension was deposited on a pre-cleaned glassy carbon (GC) disc electrode (5.0 mm diameter, 0.196 cm^2 , Pine Instruments) and allowed to dry under air flow at ambient temperature. The deposition steps were repeated to obtain the desired catalyst loading on GC electrode. The electrocatalytic activity was studied in a three-electrode cell assembly connected to a potentiostat (EG&G 273A). A 1.0 M KOH solution was used as working electrolyte. Saturated calomel electrode (mercury/mercury chloride, SCE) and coiled platinum mesh were used as the reference and counter electrode, respectively. Linear sweep voltammetry was applied with a scan rate of 5 mV s^{-1} . The SCE electrode was calibrated against normal hydrogen electrode (NHE), and its potential was converted into NHE potential. The current density was calculated against the geometric area of the glassy carbon electrode and presented after iR correction. Before and during the cathodic measurement, high purity H_2 gas was used to remove the dissolved O_2 from the solution. Electrochemical impedance spectroscopy (EIS) was performed in 1.0 M KOH between the frequency range of 105 Hz

and 0.01 Hz with ac amplitude of 10 mV. All the EIS data was normalized to geometric surface area of the working electrode.

3.3 Results and discussion:

A schematic illustration of various steps involved in the synthesis of Mo₂C/C is presented in Figure 15 Metal organic framework (MIL-53(Al)) was synthesized hydrothermally at 220 °C by heating an aqueous solution of aluminum nitrate and phthalic acid. Further, MIL-53(Al) was suspended in a clear solution consisting of anhydrous isopropanol and molybdenum chloride for homogeneous and uniform impregnation of molybdenum into MOF's frameworks. Care should be taken while adding molybdenum chloride into anhydrous isopropanol as it reacts rapidly with alcohol producing hydrochloric acid. As-prepared MIL-53(Al) was heated at 120 °C to remove adsorbed water or moisture, as it is hygroscopic in nature, and immediately added into reaction mixture. Isopropanol was evaporated producing a molybdenum-enriched MIL-53(Al), which was indicated by a color change from white to dark blue, and subjected to heat treatment to obtain Mo₂C/C. During carburization process under flow of CH₄ at high temperature, MOF (1) provided a limited space for fair dispersion, controlled nucleation and growth of fine Mo₂C nanocrystals, and (2) transformed into mesoporous and rigid carbon support carrying Mo₂C nanoparticles. Restricted and ordered array of microporous texture of MIL53(Al) is likely to inhibit agglomeration and coalescence of Mo₂C nanoparticles, presumably through homogeneous distribution of molybdenum on MOF frameworks (external and internal). Lastly, metallic Al was leached out selectively with highly concentrated aqueous solution of NaOH to

produce the desired electrocatalyst. Furthermore, CH_4 acted as a reducing agent and is prerequisite to obtain $\text{Mo}_2\text{C}/\text{C}$. The reaction between CH_4 and oxide of metal organic frameworks could lead to the formation of CO_2 and CO gases. Moreover, decomposition of CH_4 at high temperature could produce H_2 and hydrocarbon gases such as C_2H_2 , C_3H_6 etc. Produced gases can act as reductant and source of carbon.

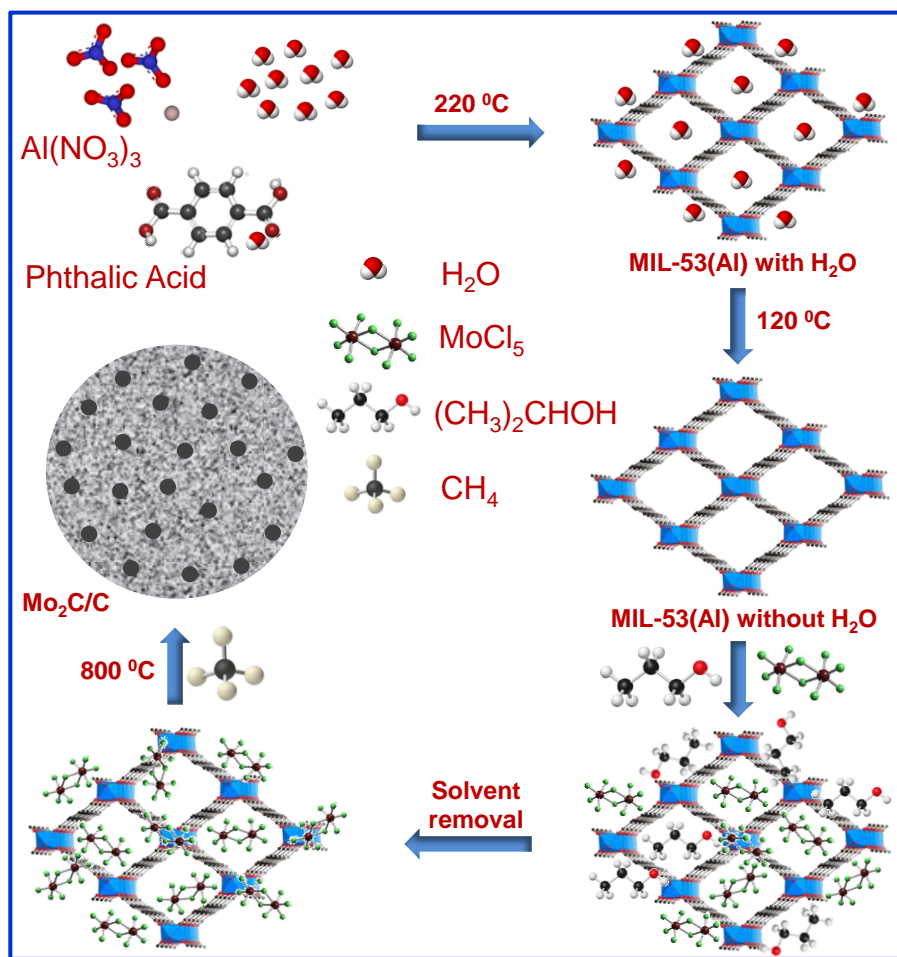


Figure 15: Schematic illustration of the likely pathways involved in the formation of $\text{Mo}_2\text{C}/\text{C}$ electrocatalyst.

On the contrary, formation of molybdenum dioxide (MoO_2) was observed when the molybdenum-impregnated MOF was annealed under N_2 or Ar at 800°C

for 2 h (Figure 16). Formation of MIL-53(Al) was confirmed by XRD and BET analyses. XRD patterns, shown in Figure 17, could be attributed to typical patterns of MIL-53(Al) and indicate crystalline nature of the sample. Furthermore, peaks at approximately 8.7° and 10° are very indicative of a narrow-pore form; upon water/moisture adsorption, structure of MIL-53(Al) is reported to develop from large-pore to narrow-pore form [111]. The XRD patterns of molybdenum-impregnated sample, presented in Figure 17A, suggested the stability and retention of basic frameworks of MIL-53(Al), except the pore size narrowing [111] occurred as indicated by noticeable attenuation in the intensity of peaks at 8.7° and 10° . However, a drastic change occurred in structural features after heat treatment at 800°C or higher temperature under the flow of CH_4 . Typical XRD patterns of samples obtained after carburization is shown in Figure 17B. Patterns indicated the formation of well crystalline structure, and the diffraction peaks centred at 34.3° (100), 37.9° (002), 39.4° (101), 52.1° (102), 61.7° (110), 69.6° (103), and 74.5° (200) are attributed to $\beta\text{-Mo}_2\text{C}$ phase with a hexagonal closed packed structure (PDF-00-001-1188) [112]. XRD analysis of annealed samples also suggested the formation of $\beta\text{-Mo}_2\text{C}$ phase with improved crystallinity. Moreover, aluminum was observed in XRD analysis as MIL-53(Al) contains aluminum. It was removed from the nanocomposite through alkaline treatment using highly concentrated NaOH solution. The absence of aluminum diffraction peak in XRD spectra indicated that Al was completely leached out without affecting the crystal structure of $\text{Mo}_2\text{C}/\text{C}$ nanocomposite. Removal of Al was confirmed by XPS analysis, as shown in Figure 18.

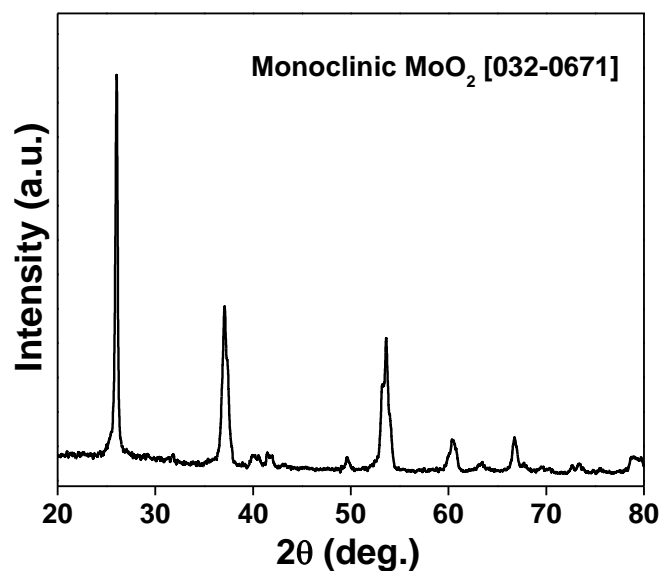


Figure 16: XRD spectra of MoO₂ obtained at 800 °C annealed under N₂ gas.

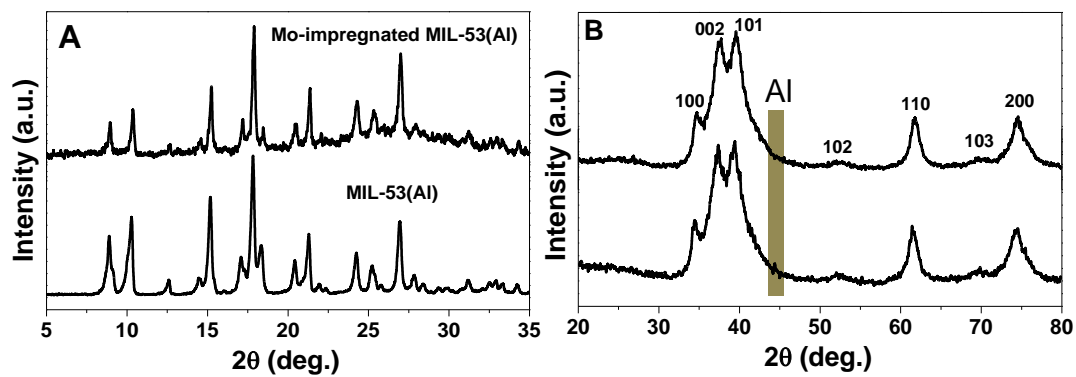


Figure 17: Powder XRD patterns of (A) MIL-53(Al) before and after molybdenum impregnation, and (B) Mo₂C/C nanocomposite before and after Al removal.

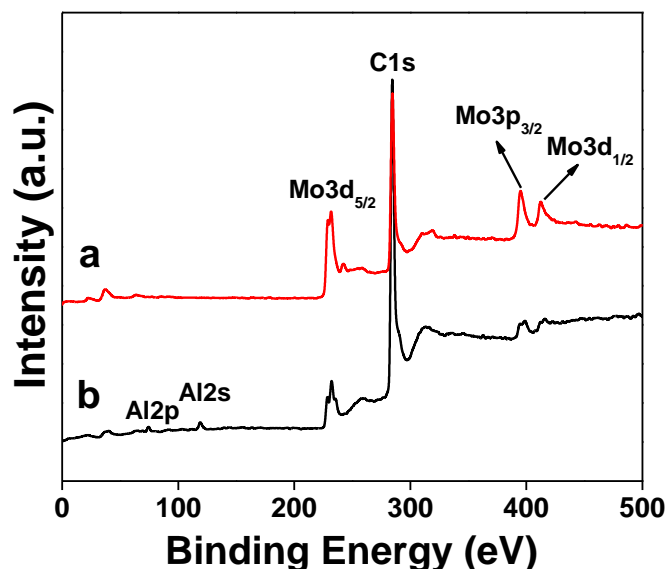


Figure 18: XPS survey spectra of Mo₂C/C before (a) and after Al removal (b).

BET study (Figure 19A) verified the microporous texture of MIL-53(Al). The nitrogen adsorption-desorption isotherms of the synthesized MIL-53(Al) presented type-I adsorption and desorption curves with BET surface area of 1165 m²g⁻¹. Similar isotherms for MIL-53(Al) are documented in the literature [105, 107].

Interestingly, MIL-53(Al) containing molybdenum metal source heated at 800 °C under methane shows a transformation from microporous to mesoporous texture (Figure 19B). As shown, the N₂ adsorption-desorption isotherms were in conformity to the classical type-IV behavior that is characteristic of mesoporous materials. A narrow pore size distribution centered at ~3.6 nm was observed (inset figure in Figure 19B).

The FE-SEM and TEM images shown in Figure 20 highlight the size,

morphology, and homogeneity of Mo₂C/C. FE-SEM image showed Mo₂C/Cnanocomposite possessed irregular and ill-defined morphology, closely resembling to shape and morphology of as-prepared MIL-53(Al). Further structural details and distribution of Mo₂C nanocrystallites were analyzed by TEM, as shown in Figures 20B and C.

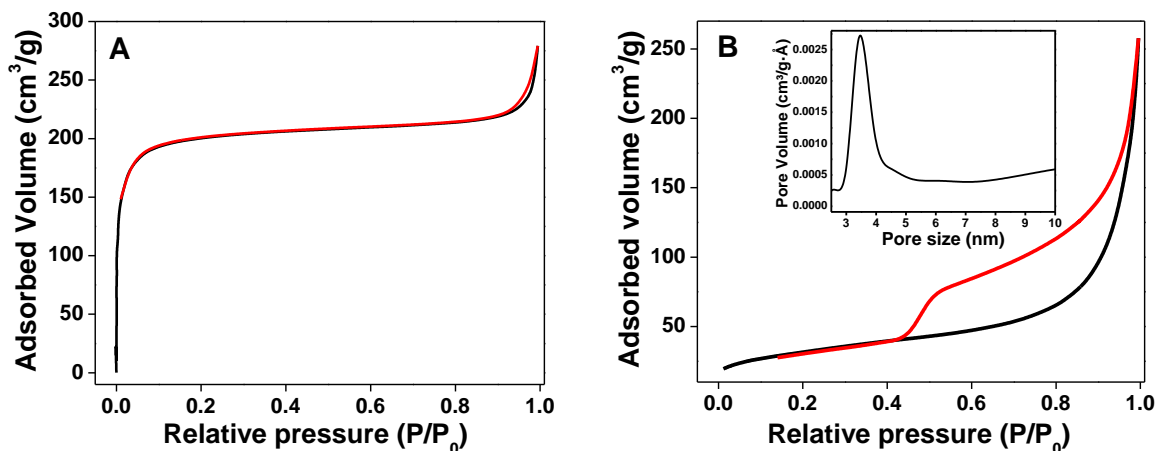


Figure 19: BET isotherms of (A) MIL-53(Al) and (B) Mo₂C/C nanocomposite together with pore distribution (Fig. B inset).

As evident, Mo₂C grains have almost uniform, near-spherical shape with size in the range of 5 to 10 nm. The attributes of the carbon layer around the electrocatalyst may have a substantial impact on the electrical conductivity and release of hydrogen bubbles. Figure 20D reveals that Mo₂C nanoparticles were well-distributed and effectively embedded in the thin layers of carbon with mesoporous feature derived from the carburization of MIL-53(Al) MOF. A localized EDS (Figure 22) analysis further corroborated that these thin layers are essentially carbon. The electron

diffraction and the HR-TEM microscopy images (Figures 20E and F) show polycrystalline nature of sample with high degree of crystallinity.

The interplanar distance for the (101) plane was computed to be 0.23 nm, in good agreement with 0.23 nm based on XRD data. Furthermore, crystal structure, morphological details and distribution of Mo₂C nanoparticles supported on XC carbon were also obtained by XRD and TEM, as shown in Figure 20 XRD patterns confirmed the formation of crystalline β -phase of Mo₂C. However, TEM investigation revealed the formation of bigger Mo₂C nanoparticles with particle size in the range of 20 to 40 nm. MOF has porous texture created by organic ligands which are susceptible to heat treatment. At high temperature, such as 800 °C, the microporous structure of MOF collapsed and transformed into mesoporous carbon as confirmed by BET analysis. Moreover, at high temperature, sintering and growth of Mo₂C are likely to take place thus making Mo₂C particle between 5 and 10 nm. However, the growth of Mo₂C was still restricted by porous texture of MOF or mesoporous carbon. Contrary, when Mo₂C was grown on commercial XC carbon, the particle size was bigger highlighting the effect of MOF.

Detailed chemical composition and oxidations states of Mo₂C/C were investigated by XPS, and respective spectra for Mo and C, are illustrated in Figure 23. XPS survey scans before and after Al removal are shown in Figure 18 suggesting the removal of Al from Mo₂C/C after alkaline treatment. The binding energy peaks at 228.7 and 231.8 eV are attributed to the Mo 3d_{5/2} and Mo 3d_{3/2} of Mo(II) spectral lines, respectively; these are in good agreement with those reported in the literature for Mo₂C [113, 114]. In addition, peaks at binding energies of 229.2 and 232.3 eV belong to molybdenum oxide. The surface of Mo₂C is susceptible to oxide (MoO₂ and MoO₃) formation when exposed to air

atmosphere. Formation of oxides has been observed in previous studies. In addition to characteristic peak of graphitic carbon at 284.6 eV, the C 1s spectrum (Figure 23B) also showed the presence of C–O (at 285.5 eV) groups in the layers of as-prepared Mo₂C/C catalyst.

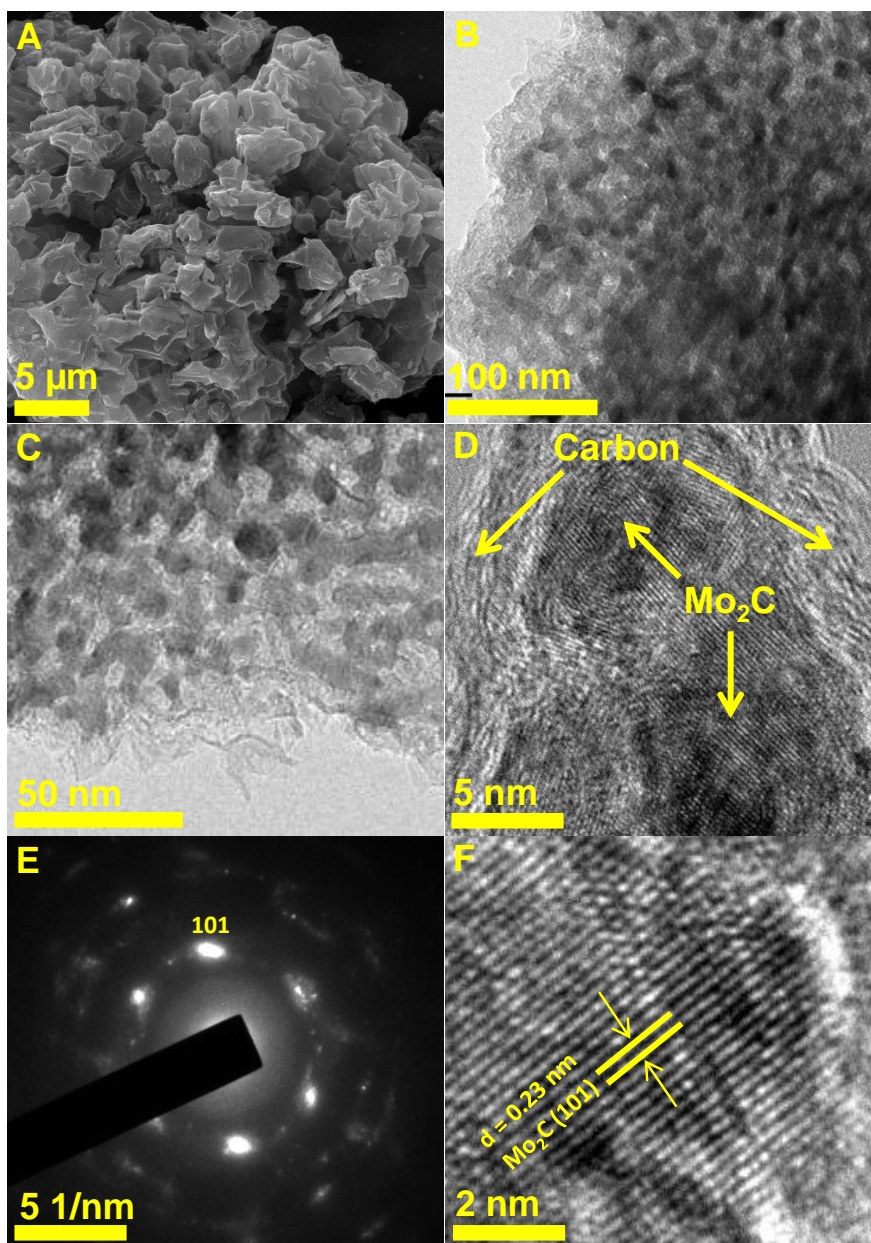


Figure 20: FESE, TEM, SAED and HR-TEM of Mo₂C/C.

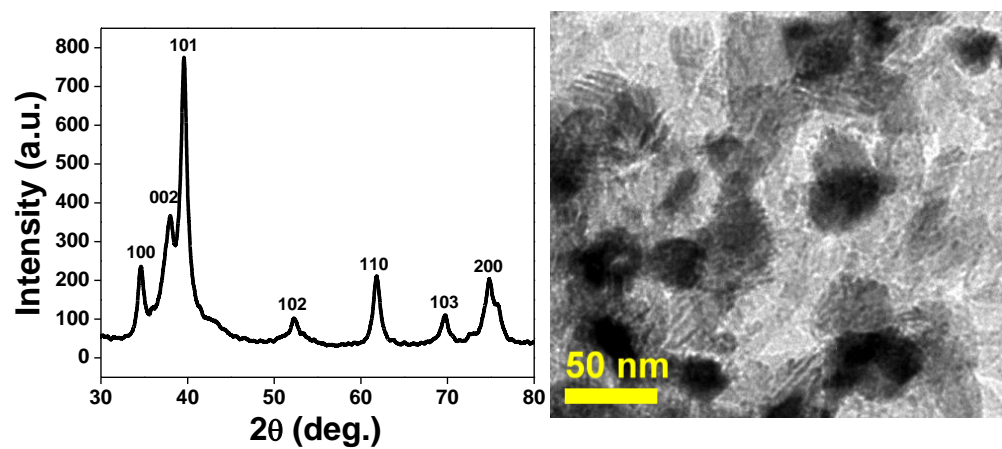


Figure 21: XRD and TEM of $\text{Mo}_2\text{C}/\text{XC}$.

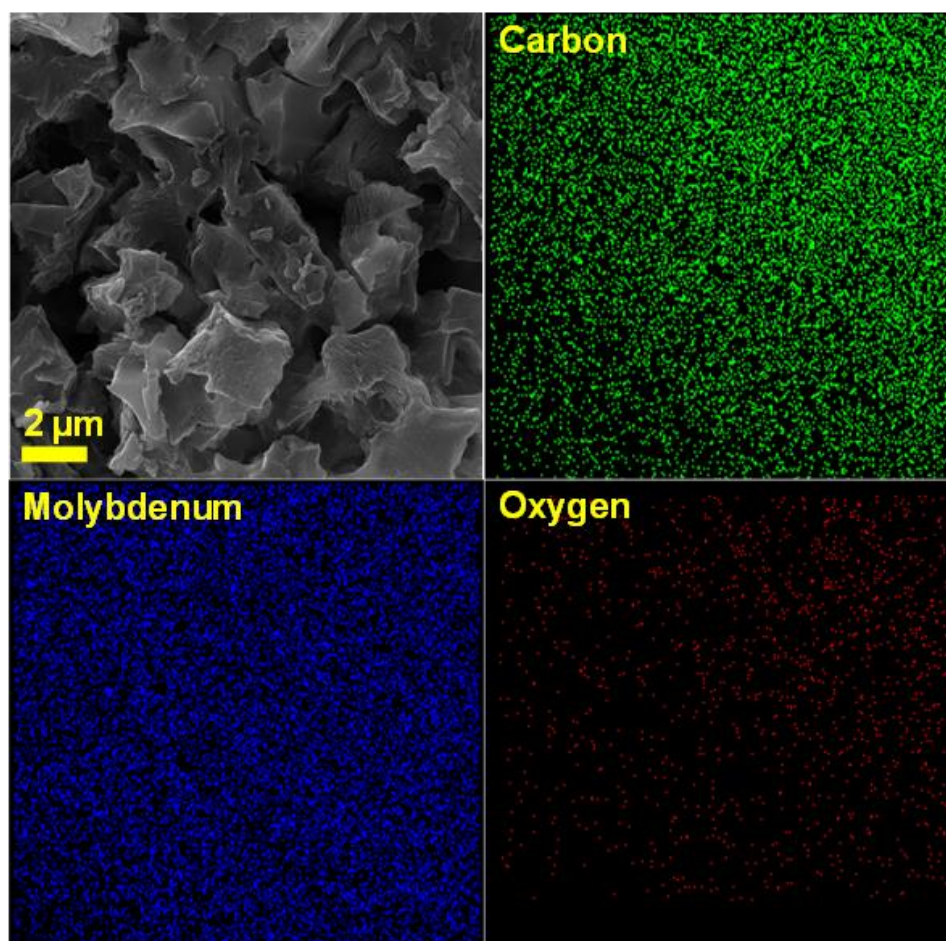


Figure 22: SEM and elemental mapping of carbon, molybdenum and oxygen present in $\text{Mo}_2\text{C}/\text{C}$.

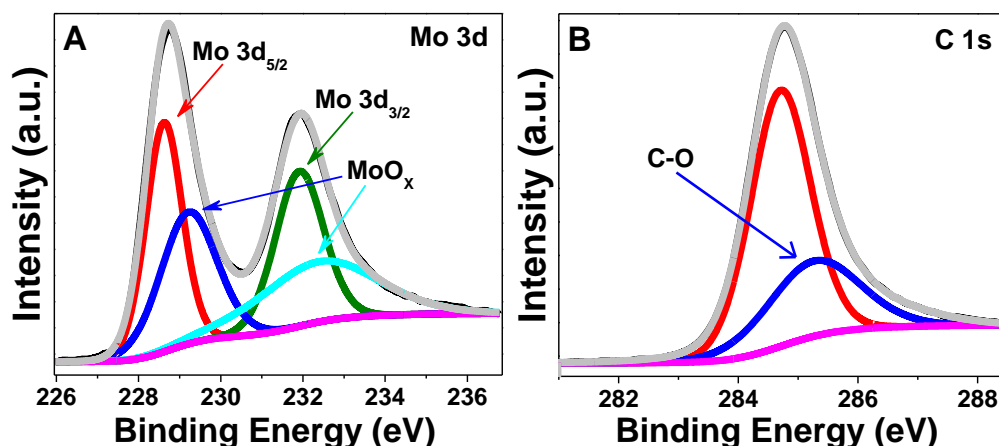


Figure 23: XPS signatures of Mo₂C/C: (A) Mo 3d, (B) C 1s.

The reduction of cathodic overpotential for H₂ evolution particularly in alkaline media is of great interest in alkaline water electrolysis cells and during some industrial productions such as chlor-alkali and chlorate cells [115]. In this study, therefore, the electrocatalytic performance of as-prepared samples was evaluated in 1.0 M KOH solution. The cathodic polarization (current density vs. potential) profiles for Mo₂C/C prepared at different annealing temperatures, such as 750, 800, 900, and 1000 °C, are shown in Figure 24A. The current density was calculated based on the geometric area of the glassy carbon electrode in all results reported here unless it is otherwise specified. As can be seen, the activity increased with increase in temperature from 750 to 800 °C followed by a decrease at higher temperature such as 900 and 1000 °C. Since electrocatalytic HER reaction is predominantly surface-dictated, it could be governed by various physicochemical features of catalyst including crystallinity and area of surface, which are primarily determined by the process temperature. XRD diffraction patterns of all the samples were recorded and

found to be similar, which suggested the formation of β - Mo_2C nanoparticles, except the improvement in crystallinity with the increasing process temperature (Figure 25).

In addition, BET analysis indicated a substantial drop in the surface area of catalyst after heat treatment, and this reduction in the surface area continued with the increasing temperature presumably due to particle sintering at high temperature. Surface area of MOF was measured to be $1165 \text{ m}^2\text{g}^{-1}$, while for $\text{Mo}_2\text{C}/\text{C}$ obtained at different temperatures such as 750, 800, 900, and 1000 °C was 202, 168, 113 and $58 \text{ m}^2\text{g}^{-1}$ respectively. The electrochemical active area of $\text{Mo}_2\text{C}/\text{C}$ annealed at different temperatures was quantified through the measurement of double layer capacitance (C_{dl}) of cyclic voltammograms recorded at different scan rates (Figure 26). Highest double layer capacitance (24 mFcm^{-2}) was possessed by the sample prepared at 750 °C, and it decreased with increasing process temperature. Usually, higher C_{dl} is demonstrated as higher electrochemical active area [53, 120, 121]. Although the sample prepared at 750 °C had the highest C_{dl} , $\text{Mo}_2\text{C}/\text{C}$ synthesized at 800 °C showed better performance. Higher C_{dl} or electrochemical active area could also result from higher real surface area, and inferior activity could be attributed to its low crystalline structure as indicated by XRD. The electrochemical activity can also be represented as specific activity ($\text{mA}/\text{cm}^2 \text{ real}$), normalized to the real area of the active materials. Potentiodynamic curves of specific activity or specific current density calculated with respect to real surface area of $\text{Mo}_2\text{C}/\text{C}$ composite are shown in Figure 24. $\text{Mo}_2\text{C}/\text{C}$ prepared at 800 °C showed the highest specific activity, though the real area ($168 \text{ m}^2\text{g}^{-1}$) was lower as compared to the sample prepared at 750 °C. The trend of specific current density with respect to temperature agreed well with that of current density. The higher electrocatalytic activity (with a small overpotential of 165 mV at 10 mA cm^{-2}),

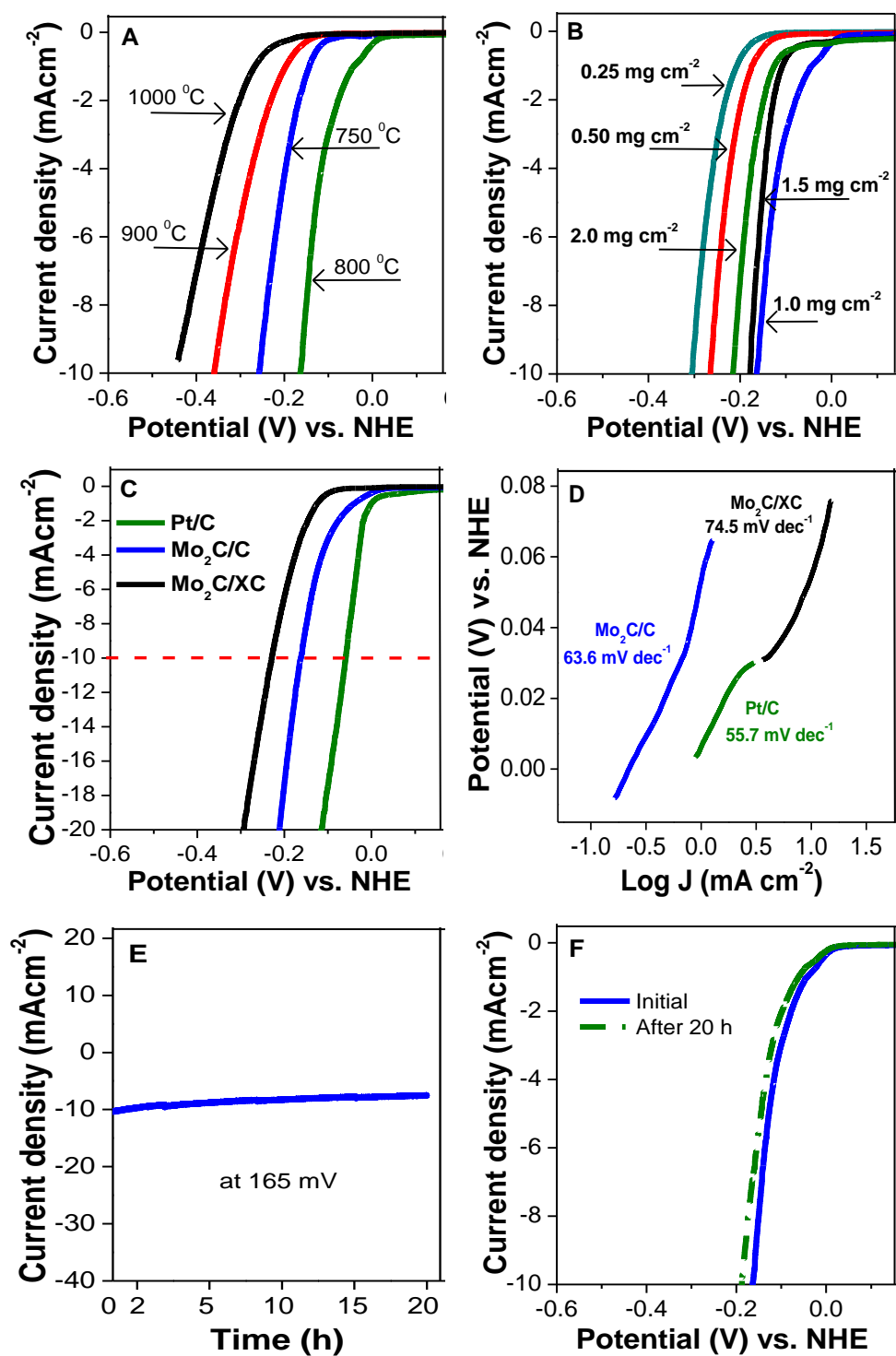


Figure 24: (A) Potentiodynamic curves showing the effect of carburization temperature and (B) catalyst loading on GCE. (C) Comparative current-potential curves of Pt/C, Mo₂C/C and Mo₂C/XC72 and (D) their Tafel plots. (E) A time-dependent profile of current density at $\eta = 165$ mV for 20 h, and (F) polarization curves before and after durability test.

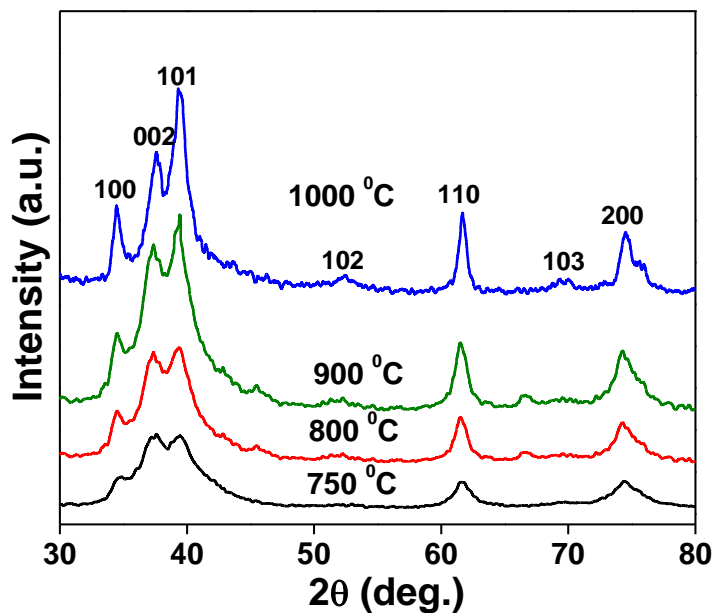


Figure 25: XRD spectra of Mo₂C/C carburized at different temperature.

shown by samples annealed at 800 °C, seems to be due to optimal compromise between the surface area and degree of crystallinity. The lower activity at lower temperature (750 °C) could be due to poor degree of crystallinity, which is not compensated by the positive effect given by its high surface area. This reinforces the notion that surface area is not entirely responsible for high activity. The lower activity of Mo₂C/C prepared at 900 and 1000 °C could presumably be attributed to sintering of particles, as indicated by the significant drop in BET area of the composite.

Since catalyst loading on the electrodes is an important factor to take into account in determining the current density, its effect was studied and the results are shown in Figure 24B. The current density increased monotonically with the increase in loading from 0.25 to 1.0 mg cm⁻².

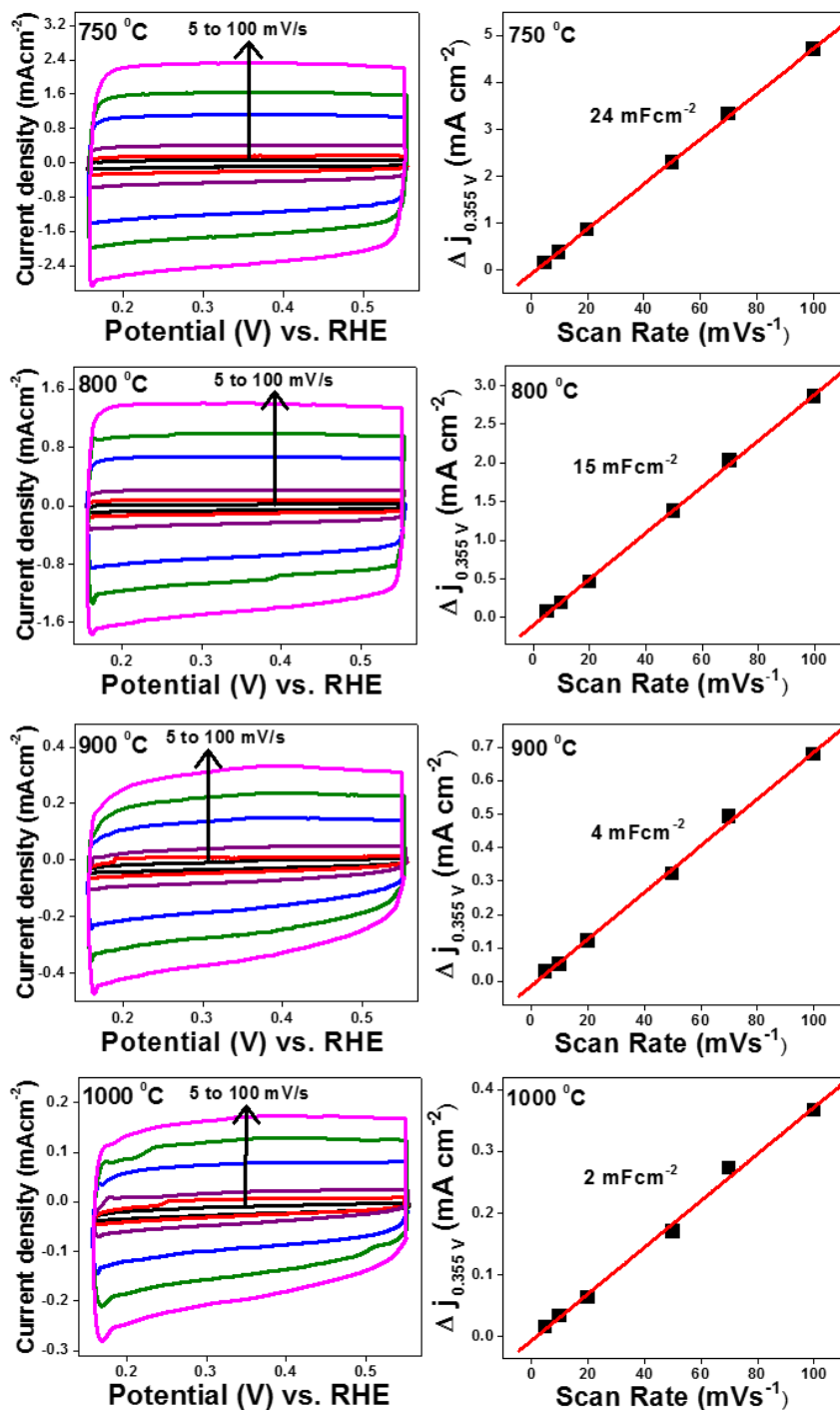


Figure 26: Effect of annealing temperature on cyclic voltammograms (CVs) of $\text{Mo}_2\text{C}/\text{C}$ recorded at different scan rates from 5 to 100 mV s^{-1} , and their corresponding plots of the current density at 0.355 V_{RHE} vs. scan rate. CVs were recorded in non-faradic region. The linear slopes are equivalent to twice of the electrochemical double layer capacitance (C_{dl}).

However, a further increase in the catalyst loading, such as 1.5 and 2.0 mg.cm⁻², resulted in the decrease in current density. An increase in the current density could presumably be rationalized in terms of increased number of active sites. Similar activity behavior with respect to catalyst loading are reported elsewhere (put references). It is most likely that such a behavior has a direct relationship with mass transport through thin-film electrode. In our case, it seems that loadings higher than 1 mg/cm² can cause mass transport limitation; be it diffusion of electrolyte to or release of hydrogen from active sites in the thin-film electrode. Thickness of electrode depends on density of materials (Mo₂C/C) and loading as well.

Since the catalyst prepared at 800 °C with 1 mg.cm⁻² loading showed the best electrocatalytic activity towards H₂ evolution reaction, its performance was compared with

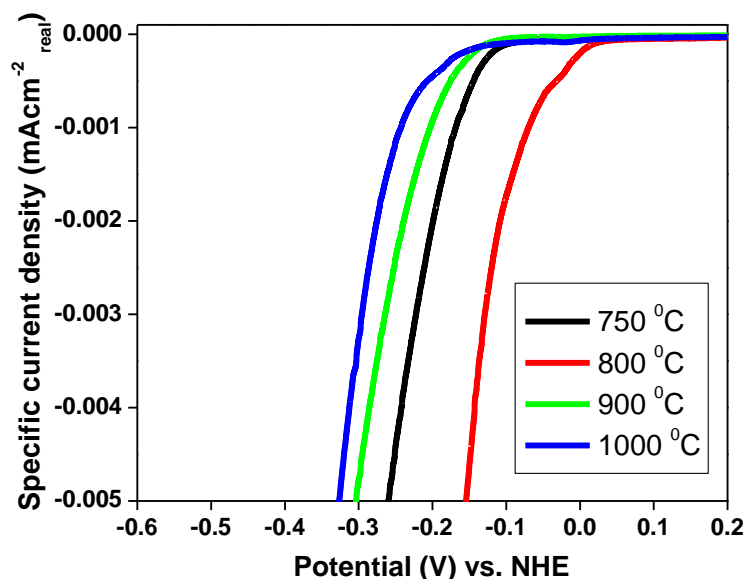


Figure 27: Potentiodynamic curves showing the effect of temperature on specific current density calculated with real surface area.

that of commercial electrocatalyst Pt/C. Furthermore, to perceive the significance of using metal organic framework as source of carbon and support, Mo₂C supported on high surface area carbon black (XC72R) was also synthesized under identical synthesis conditions (800 °C, 2 h) and its activity was also compared. The comparative electrocatalytic study was carried out under identical experimental conditions with same mass of catalyst loading on GC electrode (Figure 24C). As could be seen, for 10 mA current density, the required potentials for Pt/C, Mo₂C/C and Mo₂C/XC72 were recorded to be ~57, 165 and 229 mV, respectively. As expected, Pt/C electrocatalyst still shows the best performance followed by the as-prepared catalyst Mo₂C/C and Mo₂C/XC72. In virtue of the unique metal-support interaction presumably owing to smaller particle size with fair dispersion, Mo₂C/C exhibited excellent electrocatalytic activity for HER in alkaline media. Moreover, the Tafel plots, presented in Figure 24D, showed a fairly low Tafel slope of 63.6 mV per decade for Mo₂C/C, higher than 55.7 mV per decade for the Pt/C but lower than 74.5 mV per decade for the Mo₂C/XC72.

To investigate the durability of as-prepared electrocatalyst, experiment was conducted under the identical conditions, but at constant potential (165 mV) for 20 h. Figure 24E shows the change in current density with respect to time. As observed, the drop in current density was insignificant after 20 h demonstrating the stability of Mo₂C/C under applied experimental conditions. Furthermore, after 20 h of reaction, the used electrode was re-polarized and current density was quantified as a function of potential. The comparative polarization curves recorded before and after potential hold test are shown in Figure 24F. It was noticed that the overvoltage corresponding to current density of 10 mA/cm² has increased by 20 mV. It is known, however, that metal carbides in aqueous

solutions can passivate and form oxycarbide layer on the surface and this may contribute in enhancing electrical resistance in the thin-film electrode. More investigation is underway to better understand the loss in HER activity after holding potential at 165 mV.

Further kinetic insights about electrode process and charge transfer were obtained by electrochemical impedance spectroscopy (EIS) studies. All the measurements were conducted from 10^5 Hz to 0.01 Hz with ac amplitude of 10 mV at different overpotential ($\eta = 0$ to 200 mV vs. NHE) in alkaline solution of 1.0 M KOH. A representative Nyquist plot of $\text{Mo}_2\text{C}/\text{C}$ as a function of electrode overpotential is shown in Figure 28A. The plot indicated the existence of two semicircles, an enlarged view is presented in Figure 28B, at all applied overpotential. A typical Bode plot, depicted in Figure 28C, further confirms the presence of two-time constants in the catalyst system. In the reported investigations, EIS results for hydrogen evolution reaction have been predominantly construed by three types of electrical equivalent circuit models; one-time constant model [116], two-time constant parallel model [34, 117] and two-time constant serial model [118]. In this study, the two-time constant parallel model, which consists of solution resistance (R_s) in series with two parallel constant phase element-resistance, was exercised to fit the experimental data (inset figure in Figure 28A). According to this model, R_s represents a collective resistance which includes the resistance coming from wiring (R_{wiring}), carbon support (R_{carbon}), resistance of Mo_2C (R_{carbide}), and the solution resistance (R_{soln}) [118]. The semicircle observed at higher frequency could be attributed to the surface porosity (corroborates BET observation), while the other semicircle at lower frequency corresponds to the charge transfer process of hydrogen evolution reaction [118]. Results demonstrated significant dependency of charge transfer process on the applied potential; charge transfer resistance (R_{ct}) decreases with

increasing overpotential suggesting a faster charge transfer kinetics at high overpotential. R_{ct} values decreased noticeably from 145 Ω at 100 mV to 8 Ω at 200 mV overpotential. A comparative EIS response of Mo₂C/C and Mo₂C/XC at 100 and 150 mV overpotentials are depicted in Figure 28D. Moreover, a comparative analysis of Z (Ω) and phase angle as a function of frequency is illustrated in Figure 28E. Nyquist plots of Mo₂C/XC also revealed the presence of two-time constants as could be clearly seen in Bode plots presented in Figure 28E.

Existence of two-time constants in Mo₂C/XC catalyst was also found in previous investigation [34]. The results shown in Figures 28D and E suggested faster charge transfer kinetics on Mo₂C/C surface as compared to Mo₂C/XC; the R_{ct} for Mo₂C/XC and Mo₂C/C were 34.5 Ω and 24.6 Ω , respectively at $\eta = 150$ mV. This could presumably be attributed to the mesoporous surface of MOF-derived carbon in Mo₂C/C, which could render faster desorption of H₂ from active surface sites following Volmer-Heyrovsky mechanism as discussed below.

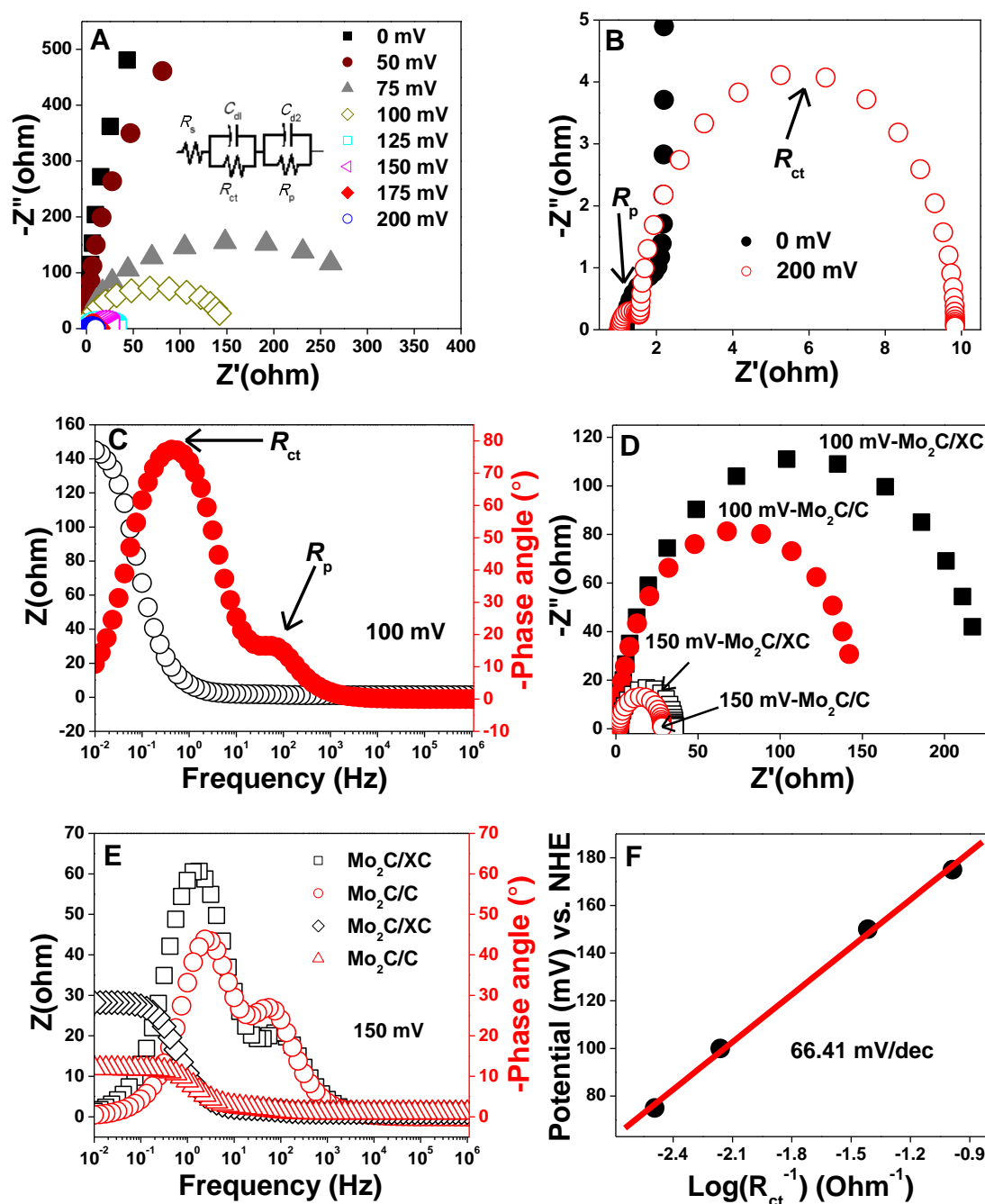


Figure 28: (A) Nyquist plots recorded at different potential (vs. NHE), (B) Nyquist plots with enlarged region showing two semicircles, (C) Bode plots showing two two-time constants, (D) comparative Nyquist plots of $\text{Mo}_2\text{C}/\text{C}$ and $\text{Mo}_2\text{C}/\text{XC}$ at $\eta = 100$ mV and 150 mV, (E) comparative Bode plots of $\text{Mo}_2\text{C}/\text{C}$ and $\text{Mo}_2\text{C}/\text{XC}$ at $\eta = 100$ mV, and (F) Tafel plot. Inset figure in 25A – electrical equivalent circuit model used to fit the EIS results (also in Figure 29).

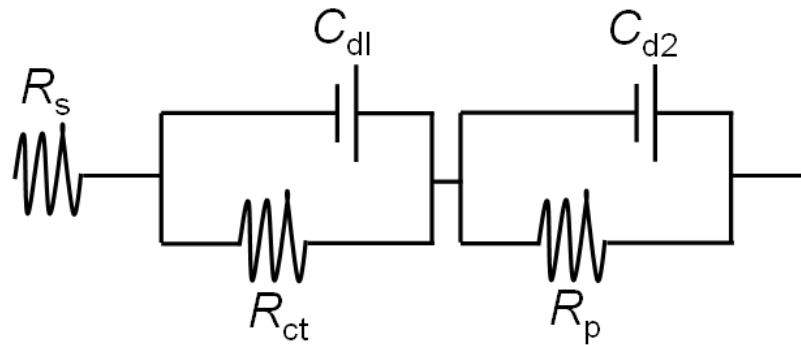


Figure 29: Two-time constant electrical equivalent circuit model utilized to fit the electrochemical impedance (EIS) results of hydrogen evolution reaction. R_s – series resistance, C_{dl} and C_{d2} are double layer capacitance, R_{ct} – charge transfer resistance for HER, R_p – resistance related to the surface porosity.

It is known that Tafel analysis of polarization curve suggests the operative mechanism in HER reaction [30, 34, 83]. However, the selection of the actual region of the polarization curve could result in ambiguous interpretation of Tafel slope and consequently the HER mechanism. Hence, EIS measurements were conducted to deduce the Tafel slopes and compare to that derived from polarization curves (linear voltammetry). Computation of the semi-logarithmic values of the inverse of R_{ct} against η resulted in a linear relationship with a gradient, which corresponds to the Tafel slope, of 66.41 mVdec^{-1} (Figure 28F). The results of Tafel slopes obtained from polarization curve and EIS were almost analogous. Such Tafel slopes reveal that HER on the as-synthesized $\text{Mo}_2\text{C}/\text{C}$ using this new approach follows the Volmer-Heyrovsky mechanism, and the rate-determining step could be the step III, which is electrochemical desorption as depicted below:

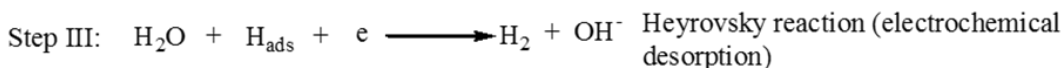
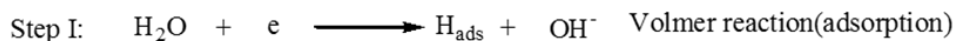


Table 1: Comparison of electrocatalysts (Mo₂C) for HER.

Catalysts	Electrolyte	Overpotential at 10 mA cm ⁻² (mV)	Tafel slope (mVdec ¹)	Catalyst loading (mg.cm ⁻²)
α -Mo ₂ C [16]	0.5 M H ₂ SO ₄	198	56	0.102
α -Mo ₂ C [16]	1 M KOH	176	58	0.102
Mo ₂ C/CNT [119]	0.1 M HClO ₄	250	251	8.2
Mo ₂ C/CXG [119]	0.1 M HClO ₄	170	264	6.3
Mo ₂ C/CNT [35]	0.5 M H ₂ SO ₄	190	63	0.65-0.67
Mo ₂ C/CNT-GR [35]	0.5 M H ₂ SO ₄	130	58	0.65-0.67
Mo ₂ C/GR [34]	0.5 M H ₂ SO ₄	242	82	0.65-0.67
Mo ₂ C/CNT [34]	0.1 M HClO ₄	152	55.2	2
Bulk Mo ₂ C [34]	0.1 M HClO ₄	~300	87.6	2
3DHP-Mo ₂ C [15]	0.5 M H ₂ SO ₄	97	60	0.28
Mo ₂ C/NCNTs [120]	0.5 M H ₂ SO ₄	147	71	3
Mo ₂ C/CNTs [120]	0.5 M H ₂ SO ₄	179	65	3
Mo ₂ C/RGO [121]	0.5 M H ₂ SO ₄	130	57.3	0.285
MoC _{x-2} [122]	0.5 M H ₂ SO ₄	160	93	0.354
Mo ₂ C nanowires [33]	0.5 M H ₂ SO ₄	200	52	0.21
Mo ₂ C/CC [123]	0.5 M H ₂ SO ₄	140	124	1.5
Mo ₂ C [112]	0.1 M HClO ₄	>250	120	0.28
Mo ₂ C-carbon [106]	0.05 M H ₂ SO ₄	>270	-	0.25
Mo ₂ C [124]	1 M H ₂ SO ₄	~210	56	1.4
Mo ₂ C [124]	1 M KOH	~190	54	0.8
Mo₂C/C^a	1 M KOH	165	66.41	1.0

a=This work

3.4 Conclusion:

Large-scale production of H_2 by electrochemical water splitting is discerned as one of the most economical and viable approaches and designing Pt-less electrocatalysts remain at the forefront of the technology development. Herein, *in-situ* transformation of metal organic frameworks (MOF), impregnated with molybdenum precursor, into a porous and rigid carbon support and molybdenum carbide (Mo_2C) is demonstrated to fabricate highly active and stable β - Mo_2C/C heterostructure for electrocatalytic H_2 evolution. The two-step synthesis approach involved the impregnation of molybdenum source into frameworks of MOF (namely MIL-53(Al)) followed by nucleation and growth of Mo_2C nanocrystals into confined porous texture through carburization. Characterization revealed the formation of mesoporous carbon embodied with crystalline nanoparticles of β - Mo_2C (between 5 and 10 nm). A probable mechanism for the formation of Mo_2C/C nanocomposite is proposed. The propensity of the catalyst was tested towards electrocatalytic H_2 evolution reaction (HER) under alkaline aqueous media (1M KOH). The electrocatalyst showed a remarkable HER activity as compared to the benchmark electrocatalyst Pt/C and $Mo_2C/XC72$ black catalysts at 10 mA/cm^2 , and stability for 20 h at the same current density. Electrochemical impedance spectroscopy results of Mo_2C/C was construed by two-time constants, porosity and charge transfer, and HER reaction followed the Volmer-Heyrovsky mechanism.

CHAPTER 4

Rational Growth of High-Performance Molybdenum Carbide on Carbon Nanotubes for Electrochemical Hydrogen Evolution Reaction

4.1 Introduction:

From environmental and energy viewpoints, production of hydrogen (H_2) using electrical energy and water offers great promises. However, the technological development of water electrolysis to achieve a high flow rate of hydrogen is essentially decelerated by the requirement of high overvoltage. Development of catalysts that can lower the overpotential for hydrogen generation could contribute substantially in overall electrocatalytic process. Currently, platinum (Pt) is known as a state-of-the-art electrocatalyst for the hydrogen evolution reaction (HER) and oxygen reduction reaction (ORR). However, due to high cost, development of Pt-less electrode materials is central to electrochemical energy conversion devices, such as H_2 fuel cells and electrolyzers. Consequently, a variety of electrodes comprised of non-precious metals, such as metal carbides (Mo_2C [34, 82, 83] and WC [84, 85]), metal sulfides & selenides (MoS_2 [30, 86], WS_2 [87, 88], Ni_3Se_2 nanoforest/Ni foam [100] and $CoSe$ [89, 90]), metal phosphides (Ni_2P and Ni_5P_4 [91–93], Cu_3P [94], FeP [95, 96], CoP [125] and $CoPS$ [126]), metal nitrides ($Co_{0.6}Mo_{1.4}N_2$ [97] and $NiMoN_x/C$ [98]), metal oxides (WO_x –carbon [99] and MoO_{3-x} [127]) have been explored. Metal carbides, especially carbides of tungsten (W) and molybdenum (Mo) due to the unique d-band electronic structure, have been reported to exhibit catalytic activities that can be analogous to that of Pt [27, 128, 129]. These metal

carbides show platinum-like catalytic activity for the HER reaction. Yet, functional and robust catalysts operating with reasonable current densities (J) at low overpotentials are scarce.

Due to superior performance and low cost, supported catalysts remain favored model for further investigation and performance amelioration. In the case of supported catalytic systems, coupling between functional sites and support may induce unique metal-support-interaction which may have significant impact on critical electrode processes such as the interfacial equilibrium, adsorption and/or desorption of reactive species and their interaction with electrocatalysts surface, electrical conductivity, and so forth. While uniform dispersion of active sites on conductive support translates into improved activity and minimizes the consumption of metals, limited efforts, however, are exerted to improve the dispersion of Mo₂C on support. For instance, Li and co-workers dispersed Mo₂C nanoparticles on hierarchical carbon microflowers through self-polymerization of dopamine, and achieved ameliorated HER performance [129]. In another study, quantum dots of Mo₂C were embedded within chitosan-derived nitrogen-doped carbon to obtain high-performance electrocatalyst [130]. Attempt was also made to inhibit the agglomeration and coalescence of Mo₂C using porous frameworks [131].

Controlling agglomeration of Mo₂C is particularly challenging, owing to the fact that Mo₂C crystallization occurs at high temperature (>750 °C). In addition, in the absence of any structure-guiding agents, unrestricted propagation of crystallites occurs which produces catalysts with low surface area and less-exposed active sites. Hence, developing protocol which could warrant controlled nucleation & growth and thus mitigate the agglomeration and the coalescence of Mo₂C on support is of great significance.

Herein, we demonstrate a simple oxalate-based complexation strategy to achieve improved dispersion and narrow particle size distribution of Mo₂C nanoparticles onto the surface of carbon nanotubes (CNTs). Complexation of molybdenum with oxalate inhibited the agglomeration and coalescence of Mo₂C, which are predominant at high temperature. Formation of molybdenum–oxalate complex was confirmed by proton and carbon nuclear magnetic resonance spectroscopy. Structural details of electrocatalyst were obtained by various techniques, and electrocatalytic property for HER reaction was investigated in acidic condition (0.5 M H₂SO₄). Electrocatalytic activity of Mo₂C/CNT prepared in the presence of oxalic acid was compared to that of Mo₂C/CNT prepared in the absence of oxalic acid and commercial electrocatalyst Pt/C. Electrochemical impedance spectroscopy (EIS) and electrochemical active surface area (ECSA) were used to explicate the observed electrode kinetics and variation in HER activities.

4.2 Experimental:

4.2.1 Synthesis of Mo₂C/CNT electrocatalyst:

Firstly, a homogeneous suspension consisting of carbon nanotubes (CNTs, 50 mg) and anhydrous ethanol (10 mL) was prepared in a closed vial. Then, a calculated amount of molybdenum chloride (MoCl₅, 142 mg) was dissolved, and the solution was kept under stirring for 2 h. After complete dissolution of MoCl₅, oxalic acid (was added and the solution was kept under stirring. The stirring was carried out at 80 °C for 12 h to achieve maximum complexation of molybdenum with oxalate group (C₂O₄²⁻). After reaction, vial was opened and ethanol was allowed to evaporate under a vigorous stirring, leaving behind

a black powder. The resulting product was dried in oven at 110 °C for overnight, and finally carburized in a tubular furnace in the flow of H₂/Ar mixture (10:90) at desired temperature (with a heating rate of 5 °Cmin⁻¹) for 2 h. The flow of mixture gas was maintained 50 mLmin⁻¹ with mass flow controller (Alicat) throughout the calcination process. After the reaction, the black product was collected and used as electrocatalyst for HER reaction. For comparison, Mo₂C/CNT was also synthesized without oxalic acid following identical conditions.

4.2.2 Characterization:

Morphological and detailed microstructural attributes of the materials were discerned with the aid of field emission scanning electron microscope (FE-SEM, Tescan Lyra-3), transmission and high-resolution transmission electron microscope and selected area electron diffraction (TEM/HR-TEM, FEI Tecnai TF20) (SAED). Other techniques employed for characterization of the samples were: X-ray diffractometry (XRD, Rigaku MiniFlex), BET surface area analyzer (Micromeritics ChemiSorb 2750), and X-ray photoelectron spectroscopy (XPS, Thermo Scientific ESCALAB 250Xi).

4.2.3 Evaluation of electrocatalytic activity:

Homogeneous ink solution was prepared by sonicating a suspension consisting of electrocatalyst (10 mg), water and isopropanol (30% V/V) and 37 µl of 1.66 % wt. Nafion® for approximately 30 min. A measured amount (16 µL) of ink was drop-casted on a pre-cleaned glassy carbon (GC) disc electrode (5.0 mm diameter, 0.196 cm², Pine Instruments), and the electrode was allowed to dry under air flow at ambient conditions. The deposition steps were repeated to achieve the desired catalyst loading on GC electrode. Hydrogen

evolution reaction (HER) was studied in a three-electrode cell assembly connected to a potentiostat (EG&G 273A). Saturated calomel electrode (mercury/mercury chloride, SCE) and coiled platinum mesh were used as the reference and counter electrode, respectively. A 0.5 M H_2SO_4 aqueous solution was used as working electrolyte. Linear sweep voltammetry was applied with a scan rate of 5 mV s^{-1} . The SCE electrode was calibrated against normal hydrogen electrode (NHE), and its potential was converted into NHE potential. The current density was calculated against geometric area of the glassy carbon electrode and presented after iR correction. Before and during the cathodic measurement, high purity H_2 gas was used to remove the dissolved O_2 from the solution. Electrochemical impedance spectroscopy (EIS) was performed in 0.5 M H_2SO_4 between the frequency range of 10^5 Hz and 0.01 Hz with ac amplitude of 10 mV. All the EIS data was normalized to geometric surface area of the working electrode.

4.3 Results and discussion:

Schematic of plausible mechanism involving complexation and nucleation with concomitant growth of $\text{Mo}_2\text{C}/\text{CNT}$ is presented in Figure 30. Carbon nanotubes were first suspended in absolute alcohol and sonicated to obtain homogeneous and uniform solution, followed by addition of MoCl_5 . In spite of being seemingly insignificant, the reaction between MoCl_5 and ethanol could be elusive. A detailed investigation on the isolation and identification of intermediates and products formed during reaction of MoCl_5 with ethanol is reported elsewhere [132]. Molybdenum pentachloride reacts rapidly with ethanol producing intermediates and HCl and/or $\text{C}_2\text{H}_5\text{Cl}$. Upon addition of oxalic acid, ion-exchange reaction takes place between ethoxy and oxalate groups producing molybdenum-

oxalate complex. Complex formation between molybdenum and oxalate was indicated by a change of solution color (Figure 31). Also, it was confirmed by ^{13}C and ^1H nuclear magnetic resonance (NMR) spectroscopy (Figure 32). Figure 32 shows the ^{13}C NMR spectrum of oxalic acid dissolved in ethanol. The peak observed at 162.24 ppm is attributed to the resonance caused by carbon of oxalate group. ^{13}C NMR spectrum of the product obtained after reaction

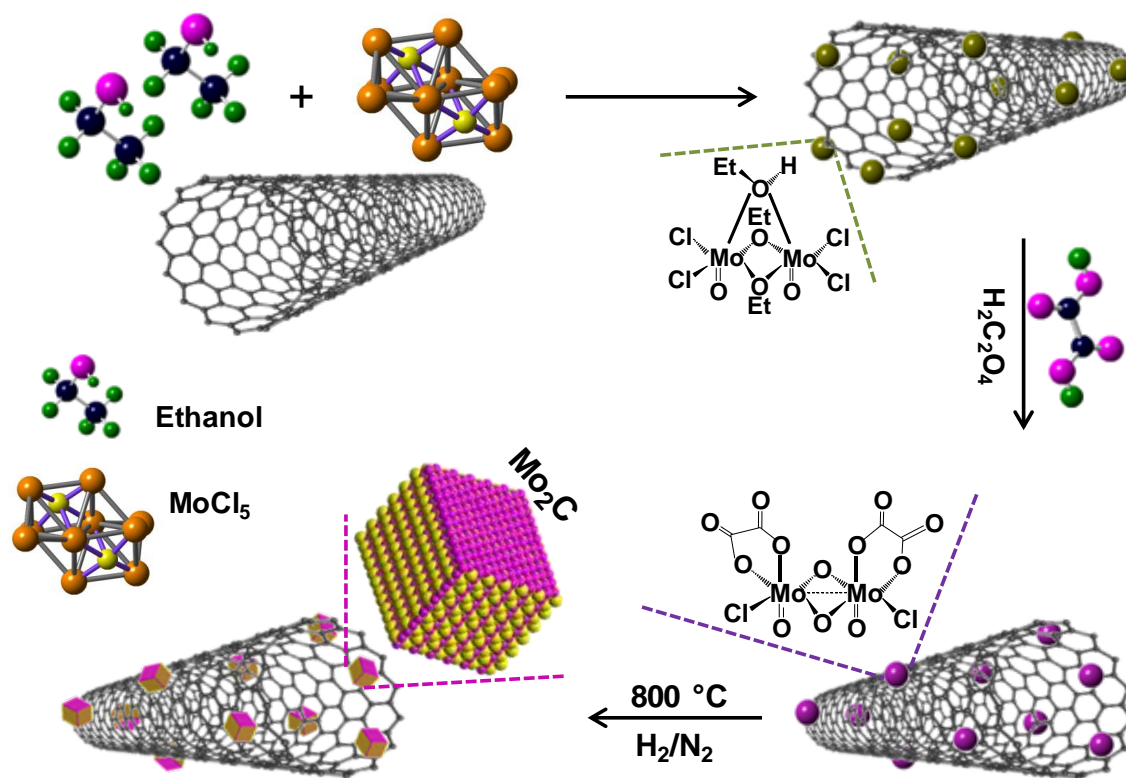


Figure 30: Suggested sequence of complexation, nucleation and concomitant growth of Mo_2C on CNT surface.

between molybdenum chloride and oxalic acid in ethanol is shown in Figure 32B. Evidently, a downfield shift in the resonance of carbon was recorded; the peak shifted to 166.77 ppm indicating a likely interaction between oxalate ($\text{C}_2\text{O}_4^{2-}$) and molybdenum (Mo) metal center, and formation of a molybdenum-oxalate complex. Moreover, only one peak

for carbon was detected. This suggests the presence of similar coordination environment around all carbon coordinated to molybdenum, and the complex has C_2 symmetry center.

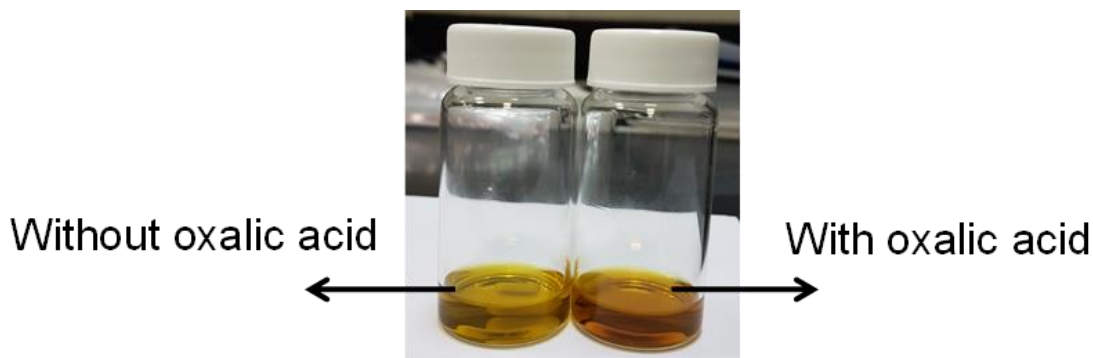


Figure 31: Photographs showing the change in color of MoCl_5 and ethanol solution after addition of oxalic acid.

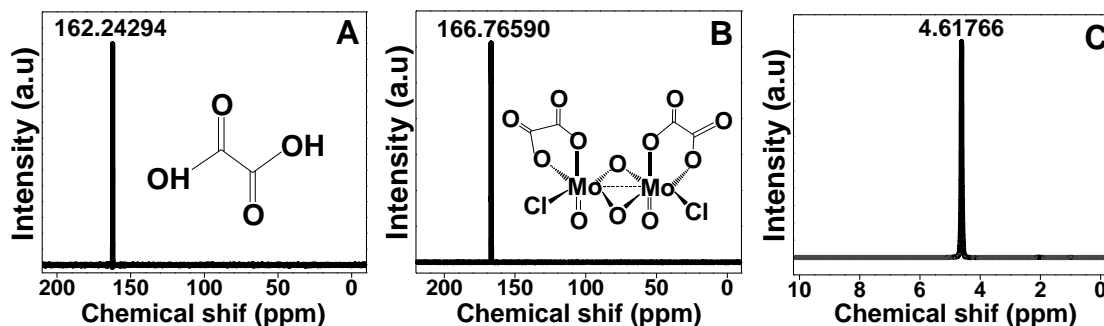


Figure 32: ^{13}C NMR of (A) solution of $\text{H}_2\text{C}_2\text{O}_4$ and $\text{C}_2\text{H}_5\text{OH}$ and (B) solution of MoCl_5 , $\text{H}_2\text{C}_2\text{O}_4$ and $\text{C}_2\text{H}_5\text{OH}$, and ^1H NMR of (C) solution of MoCl_5 , $\text{H}_2\text{C}_2\text{O}_4$ and $\text{C}_2\text{H}_5\text{OH}$.

Furthermore, the presence of any proton in the molybdenum-oxalate complex was corroborated by ^1H NMR as shown in Figure 32C. In ^1H NMR spectrum, only one resonance peak at 4.6 ppm was detected, which is assigned to the deuterated solvent.

Powder X-ray diffractions (XRD) and microscopy images of $\text{Mo}_2\text{C}/\text{CNT}$ prepared at 800°C are shown in Figure 33. Figure 33A confirmed the presence of

CNTs (at 26.1° corresponding to (002) plane) and formation of crystalline Mo_2C structure. The diffraction peaks centered at 34.3° (100), 37.9° (002), 39.4° (101), 52.1° (102), 61.7° (110), 69.6° (103), and 74.5° (200) are attributed to $\beta\text{-Mo}_2\text{C}$ phase with a hexagonal closed packed structure (PDF-00-001-1188) [112]. Figures 33B-D highlight the morphology of molybdenum carbide supported on carbon nanotubes. As evident, the morphology of CNT was retained at high processing temperature such as 800°C . Images shown in Figure 33C and D highlight the size, morphology and homogeneity of Mo_2C . Particles of Mo_2C were almost uniform, near-spherical shape with size in the range of 4 to 8 nm. The electron diffraction and the HR-TEM microscopy images (Figures 33E and F) show polycrystalline nature of sample with high degree of crystallinity. The interplanar distance for the (101) plane was estimated to be 0.23 nm, in good agreement with 0.23 nm based on XRD data. In addition, crystal structure, morphology, size and dispersion of Mo_2C nanoparticles supported on CNT prepared in the absence of oxalic acid were also collected by XRD and TEM (Figure 34). XRD analysis confirmed the formation of crystalline β -phase of Mo_2C . However, TEM revealed a wide particle size distribution, between 5 and 20 nm, of Mo_2C on CNT. This corroborates our assumption that complexation of molybdenum with oxalate modified the self-assembling behavior of molybdenum through steric hindrance, presumably increased the inter-molybdenum-distance, and thus rendered discrete nucleation and growth of Mo_2C . This led to the formation of fine and uniformly dispersed Mo_2C on CNT. Distribution of C, Mo and O in oxalate-derived $\text{Mo}_2\text{C}/\text{CNT}$ was mapped, and results are shown in Figure 35. Molybdenum seemed to be evenly distributed throughout the CNTs surface.

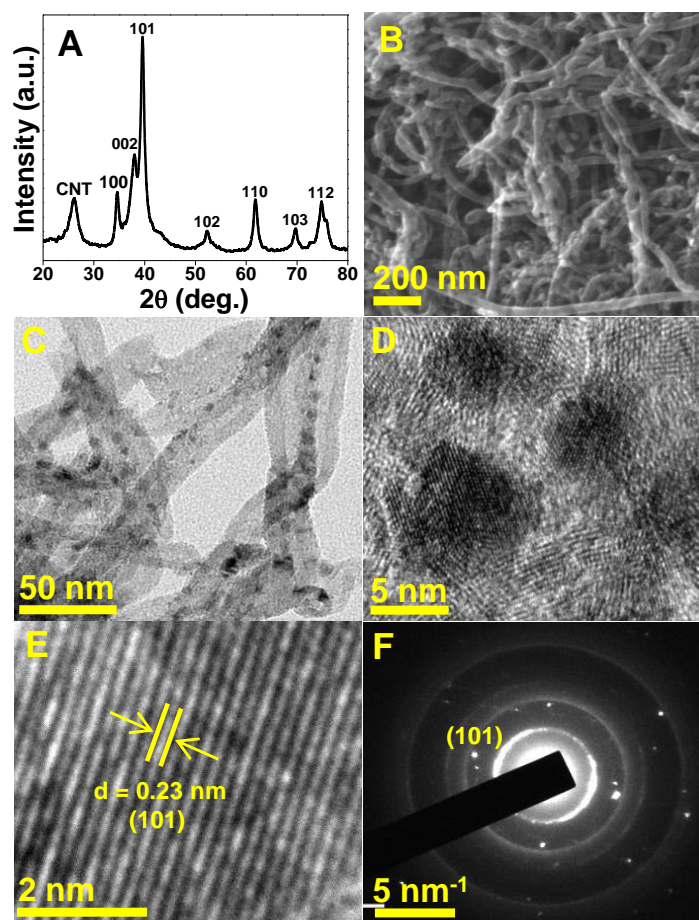


Figure 33: XRD, FESEM, TEM, HR-TEM and SAED of oxalate-derived β -Mo₂C/CNT.

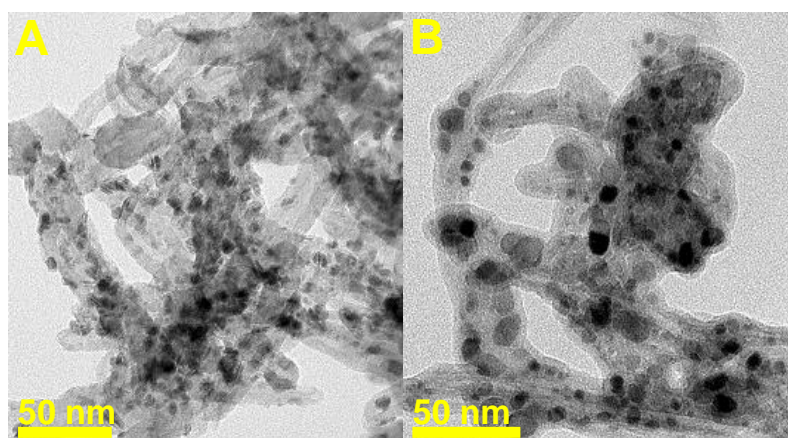


Figure 34: TEM of Mo₂C/CNT obtained in the presence (A) and absence (B) of oxalic acid.

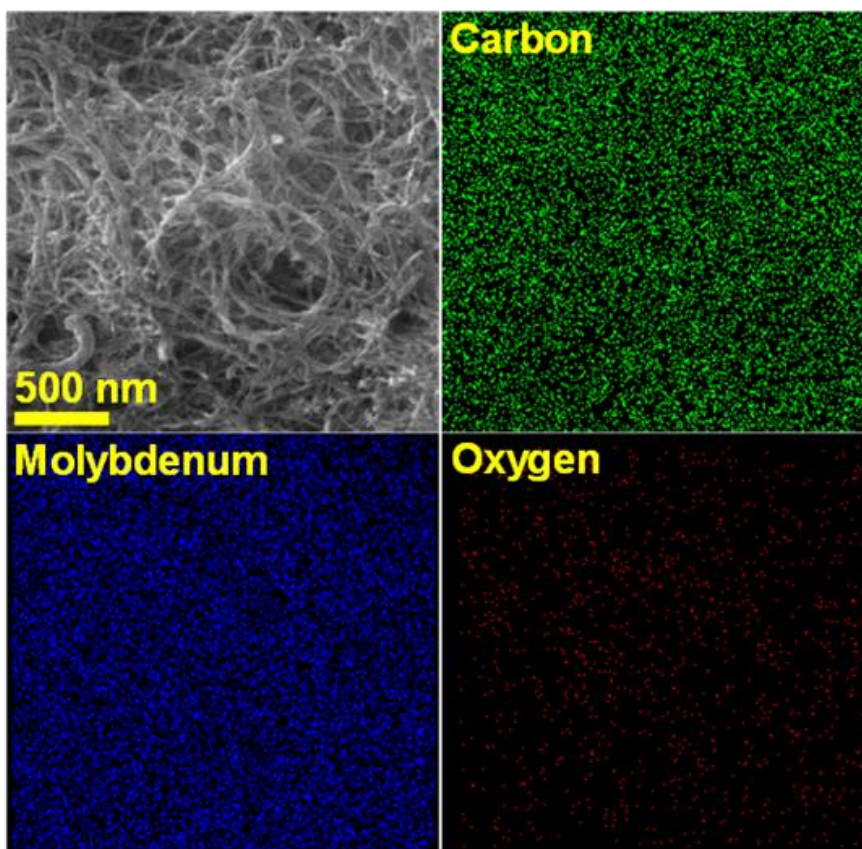


Figure 35: FESEM and elemental mapping of carbon, molybdenum and oxygen present in $\text{Mo}_2\text{C}/\text{CNT}$.

Details of chemical composition and oxidation states were analyzed by X-ray photoelectron spectroscopy (XPS). Signatures of Mo and C are shown in Figure 36. The peaks centered at 228.8 and 231.9 eV account for Mo $3d_{5/2}$ and Mo $3d_{3/2}$ of Mo(II) spectral lines, which agrees well with those reported in the literature for Mo_2C [113, 114]. In addition, peaks at binding energies of 229.3 and 232.3 eV are attributed to oxides of molybdenum. The surface of Mo_2C is susceptible to oxide (MoO_2 and MoO_3) formation when exposed to air atmosphere. Formation of oxides has been observed in previous studies [113, 114]. In addition to characteristic peak of graphitic carbon at 284.7 eV, presence of C–O (at 285.7 eV) groups in the layers of as-prepared $\text{Mo}_2\text{C}/\text{CNT}$ catalyst (Figure 36, C1s spectrum) was also detected.

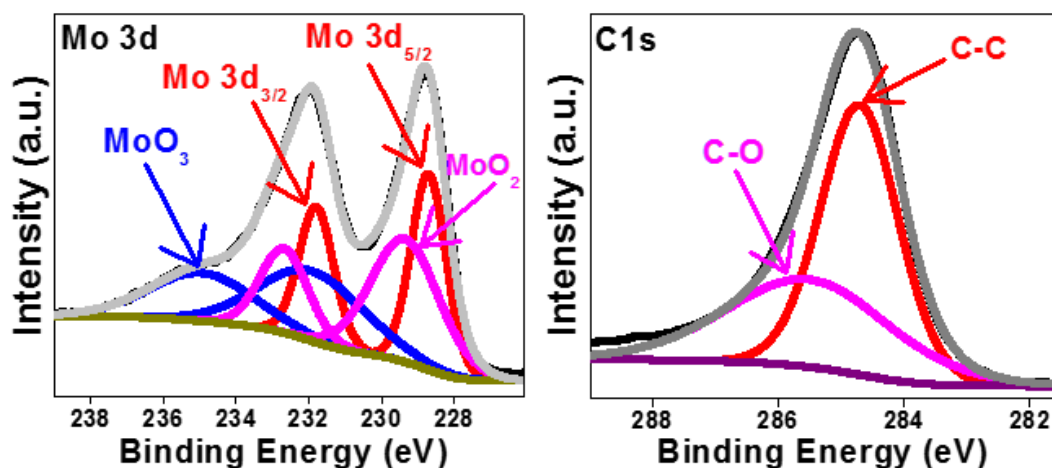


Figure 36: XPS of oxalate-prepared Mo₂C/CNT.

The propensity of electrocatalysts was investigated towards hydrogen evolution reaction in 0.5 M H₂SO₄ aqueous solution. The current density is reported based on the geometric area of the glassy carbon electrode. Profiles of cathodic polarization (current density vs. potential) are shown in Figures 34A-D. Since processing temperature could have significant impact on the physicochemical attributes of electrocatalyst and thus performance, electrochemical activity of Mo₂C/CNT prepared at different temperatures was investigated. Figure 34A compares the performance of electrocatalysts obtained at different temperature, such as 700, 800 and 900 °C. The activity increased with the increase in temperature from 700 to 800 °C, followed by a decrease at higher temperature (900 °C). Such behavior could be attributed to synergistic chemistry brought by optimum crystallinity and surface area. For instance, high processing temperature could lead to formation of electrocatalysts with different crystallinity and surface area, which in turn affect the performance of the catalyst. Evolution in crystallinity was corroborated by XRD diffraction patterns – crystallinity improved with increase in temperature (Figure 38).

However, specific surface area decreased with increasing temperature – corresponding BET surface areas at 700, 800 and 900 °C were measured and found to be 121.2, 93.7, and 67.9 m²g⁻¹. This is presumably due to particle sintering at high temperature. Inferior performance of electrocatalyst synthesized at 700 °C could be due to lower crystallinity, which did not seem to be counterpoised by the higher surface area. Likewise, lower activity of Mo₂C/CNT obtained at higher temperature (900 °C) could be attributed to lower surface area, though the catalyst had better crystallinity.

As the concentration of active sites on supports surface is important from the catalytic viewpoint, composites consisting of different Mo amounts (30, 40, 50 and 60% by weight) were prepared and the performance was evaluated (Figure 34B). The activity improved with increasing active sites, and electrocatalyst with 50% molybdenum exhibited the highest performance. A further increase in the molybdenum caused a drop in the performance. For catalysts carrying 30 and 40% molybdenum, lower activity could presumably be attributed to smaller number of active sites. Whereas, in the case of rather higher concentration of Mo₂C, the drop in activity could be due to reduction in electrochemically active surface area (EASA). Attempt was made to rationalize these findings in terms of electrochemical active surface area (EASA) and surface-charge-transfer.

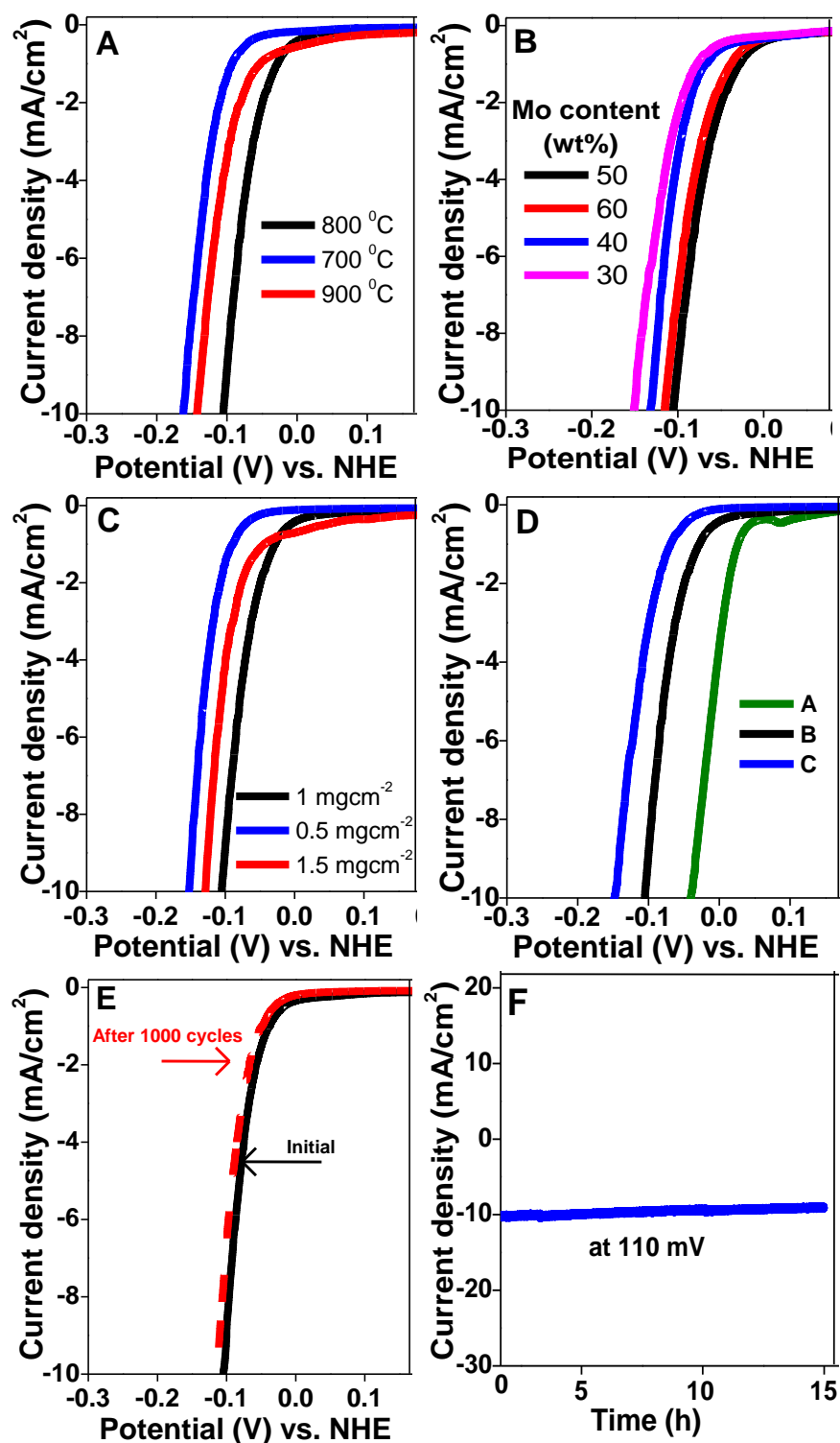


Figure 37: A – effect of synthesis temperature, B – effect of Mo content, C – effect of catalyst loading, D – (A – Pt/C, B & C – Mo₂C/CNT prepared with and without oxalic acid, respectively, E – stability before and after 1000 potentiodynamic sweeps, and F – stability before and after potentiostatic measurement.

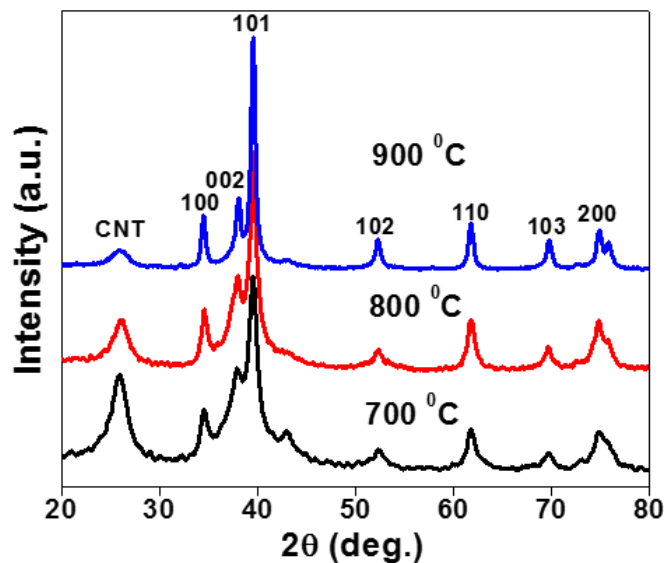


Figure 38: XRD spectra of Mo₂C/CNT obtained at different synthesis temperature.

EASA was determined by measuring double layer capacitance (C_{dl}) of cyclic voltammograms acquired at different scan rates between 5 and 100 mVs⁻¹. Cyclic voltammograms (CVs) and corresponding slopes obtained a function of molybdenum content are shown in Figure 39. Usually, higher C_{dl} corresponds to higher electrochemical active area [15, 39, 52]. EASA increased with increasing Mo up to 50% (28, 34 and 53 mFcm⁻²) followed by a drop (44 mFcm⁻²) at higher molybdenum amount (60%). Higher degree of coalescence and sintering of Mo₂C is likely owing to higher concentration of Mo, which in turn produces less EASA. These findings were further reinforced by electrochemical impedance spectroscopy. Measurements were conducted in the frequency range of 10⁵ - 0.01 Hz with an AC amplitude of 10 mV at $\eta = 90$ mV vs. NHE in 0.5 M H₂SO₄ aqueous solution. Nyquist plot (real vs. imaginary impedance) constructed as a function of Mo contents is shown in Figure 39. Significant dependency of interfacial charge

transfer on the amount of Mo was registered – charge transfer resistance (R_{ct}) decreased with increase in Mo up to 50%, implying faster charge transfer kinetics. R_{ct} values were calculated to be 115 Ω , 88 Ω and 49 Ω for 30, 40 and 50% Mo, respectively. Contrary, slightly higher R_{ct} value, 56 Ω , was estimated for Mo₂C/CNT with 60% Mo. As stated above, the increase in surface-charge-transfer-resistance could originate from diminished electrical conductivity of heterostructure owing to lesser amount of CNTs. Carbon nanotubes are endowed with higher electrical conductivity, and reduction in CNTs amount is likely to affect electrical conductivity of heterostructure unfavorably. To this end, both the EASA and the electrochemical impedance results expounded the activity response recorded as a function of molybdenum contents. Another important factor which determines the current density is the catalyst mass immobilized on the glassy carbon electrode. The variation in current density as a function of catalyst loading, 0.5, 1.0 and 1.5 mg.cm⁻², is shown in Figure 34C. Apparently, the current density increased with the increase in loading from 0.5 to 1.0 mg.cm⁻², while a further increase in the catalyst amount (1.5 mg.cm⁻²) was unfavorable. An increase in the current density could be attributed to the increased number of active sites. Similar activity behavior with respect to catalyst loading is noted in earlier studies [73, 130]. It is highly likely that such behavior has a direct relationship with mass transport through thin-film electrode. In our case, it seems that catalyst amount more than 1 mg.cm⁻² undergo mass transport limitation. This may include diffusion of electrolyte to active sites, or release of hydrogen from active sites in the thin-film electrode. Thickness of electrode depends on both the density of materials (Mo₂C/CNT) as well as deposited amount. Mo₂C/CNT electrocatalyst synthesized at 800 °C with 1 mg.cm⁻² catalysts loading and 50% molybdenum showed the best performance

towards H_2 evolution reaction. Its performance, therefore, was compared with that of commercial electrocatalyst Pt/C.

In addition, to highlight the significance of oxalate-guided protocol, electrocatalytic performance of Mo_2C/CNT (at 800 °C with 50 wt% Mo) prepared without oxalic acid is also compared (Figure 34D). Comparative electrocatalytic performance was carried out under identical experimental conditions with same mass of catalyst loading on GC electrode. To achieve a geometrical current density of 10 mA, the recorded overpotentials for Pt/C, oxalate-derived Mo_2C/CNT and Mo_2C/CNT (without oxalic acid) were ~41, 110 and 144 mV, respectively. As expected, Pt/C electrocatalyst exhibited the best performance. Electrocatalyst obtained through complexation method exhibited significant reduction in overpotential (34 mV) than that of prepared without oxalic acid. Superior performance of Mo_2C/CNT could be rationalized in terms of smaller particle size and better dispersion of active sites onto the surface of CNT. For electrocatalysts endowed with such desirable feature, improved interfacial charge transfer and higher electrochemically active surface area could be anticipated. Bulk conductivity as well as the charge transport property of Mo_2C/CNT prepared with and without oxalic acid was investigated employing electrochemical impedance spectroscopy (EIS). Potential-dependent evolution in Nyquist plots are shown in Figure 40A and C, respectively. Plots were constructed as a function of overpotential ($\eta = 0, 30, 50, 70, 90, 110, 130$ and 150 mV). The semicircular dispersion of impedance is indicative of an interfacial phenomenon operative near the electrode surface. Shorter semicircular arcs indicate faster charge transfer at the interface and vice versa. Apparently, charge transfer resistance (R_{ct}) decreased significantly with increasing overpotential, implying faster charge transfer kinetics at high overpotential.

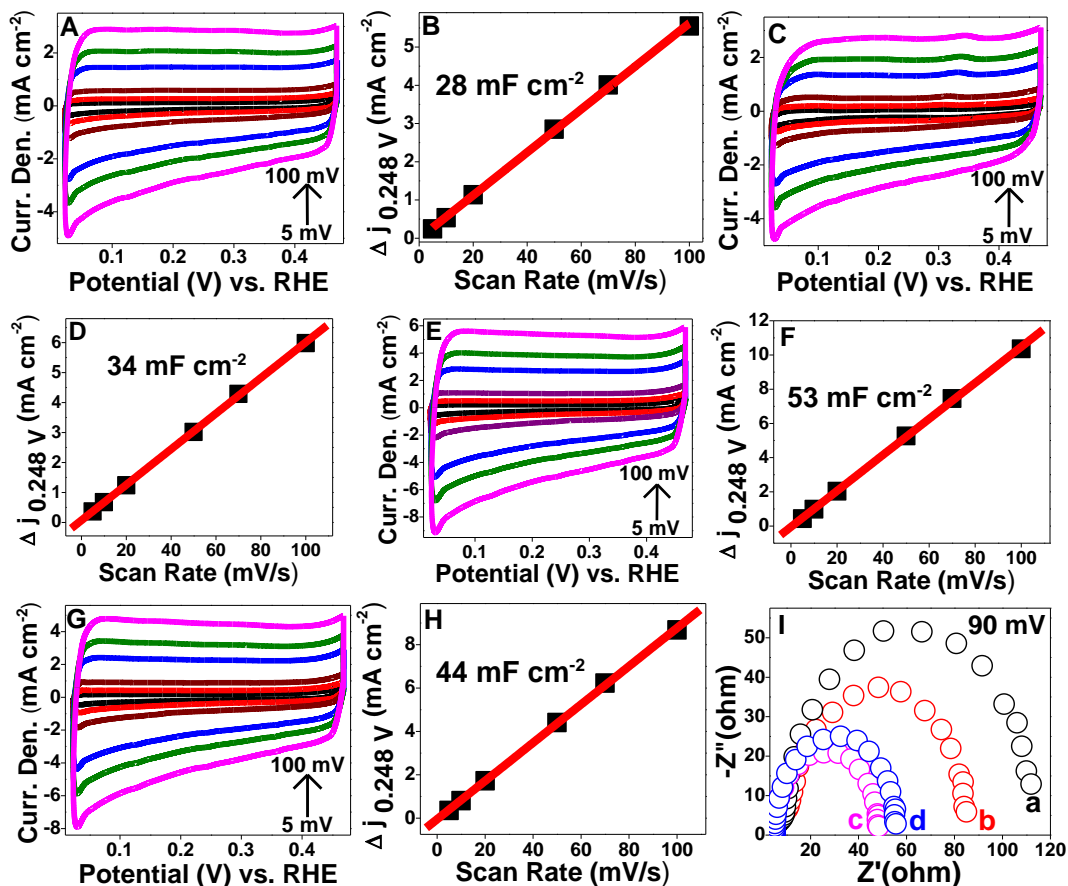


Figure 39: Cyclic voltammograms (A, C, E, G) of Mo₂C/CNT recorded at different scan rates from 5 to 100 mVs⁻¹, and their corresponding plots (B, D, F, H) of the current density at 0.248 V_{RHE} vs. scan rate as a function of Mo₂C content. CVs were recorded in non-faradic region. The linear slopes are equivalent to twice of the electrochemical double layer capacitance (C_{dl}). (I) Nyquist plot as a function of molybdenum contents.

As expected, charge transfer kinetics in oxalate-derived Mo₂C/CNT was more dominant as compared to that of prepared in absence of oxalic acid at all applied potential. For instance, an enlarged view of Nyquist plots recorded at $\eta = 150$ mV for both the samples are compared in Figure 40E. R_{ct} was smaller ($<16 \Omega$) in oxalate-derived Mo₂C/CNT than that of sample obtained in the absence of oxalic acid (24Ω). This could presumably be attributed to the smaller particle size and improved dispersion of active sites (Mo₂C) on CNT surface, as observed by TEM study.

In addition to smaller R_{ct} , Nyquist plots indicated the presence of two-time constants in the catalytic systems under investigation. This was corroborated by Bode plots - corresponding Bode plots obtained at $\eta = 150$ mV are shown in Figure 40B and D. For both the electrocatalysts, Nyquist as well as Bode data constitute two semicircles, though it was more dominant in Mo₂C/CNT prepared without oxalic acid. For electrochemical hydrogen evolution reaction, EIS observations are predominantly interpreted by three types of electrical equivalent circuit models; one-time constant model [116], two-time constant parallel model [34, 117] and two-time constant serial models [118]. In this study, the two-time constant parallel model consisting of solution resistance (R_s) in series with two parallel constant phase element-resistance was used to fit the experimental EIS data. According to this equivalent circuit model (Figure 41), R_s depicts a collective resistance, which includes the resistance from wiring (R_{wiring}), carbon support (R_{carbon}), resistance of Mo₂C ($R_{carbide}$) and resistance of solution (R_{soln}) [118]. Furthermore, charge transfer resistance, resistance arising from porous surface texture, and capacitance are denoted by R_{ct} , R_p and C_{dl} , respectively. The semicircle noticed at higher frequency accounts for the surface porosity, while the near-semicircle appeared at lower frequency corresponds to the charge transfer process for the hydrogen evolution reaction [118]. Attenuation of R_p signal, Figure 40D, in oxalate-derived Mo₂C/CNT could presumably be attributed to presence of carbon emanated from pyrolysis of oxalate group.

In addition to interfacial charge transfer kinetics, variation in the performance was also investigated in terms of specific and electrochemical active surface area. Specific surface area was measured by BET method, while electrochemical active area was

quantified through the measurement of double layer capacitance (Cdl) of cyclic voltammograms recorded at different scan rates. Nitrogen sorption isotherms of

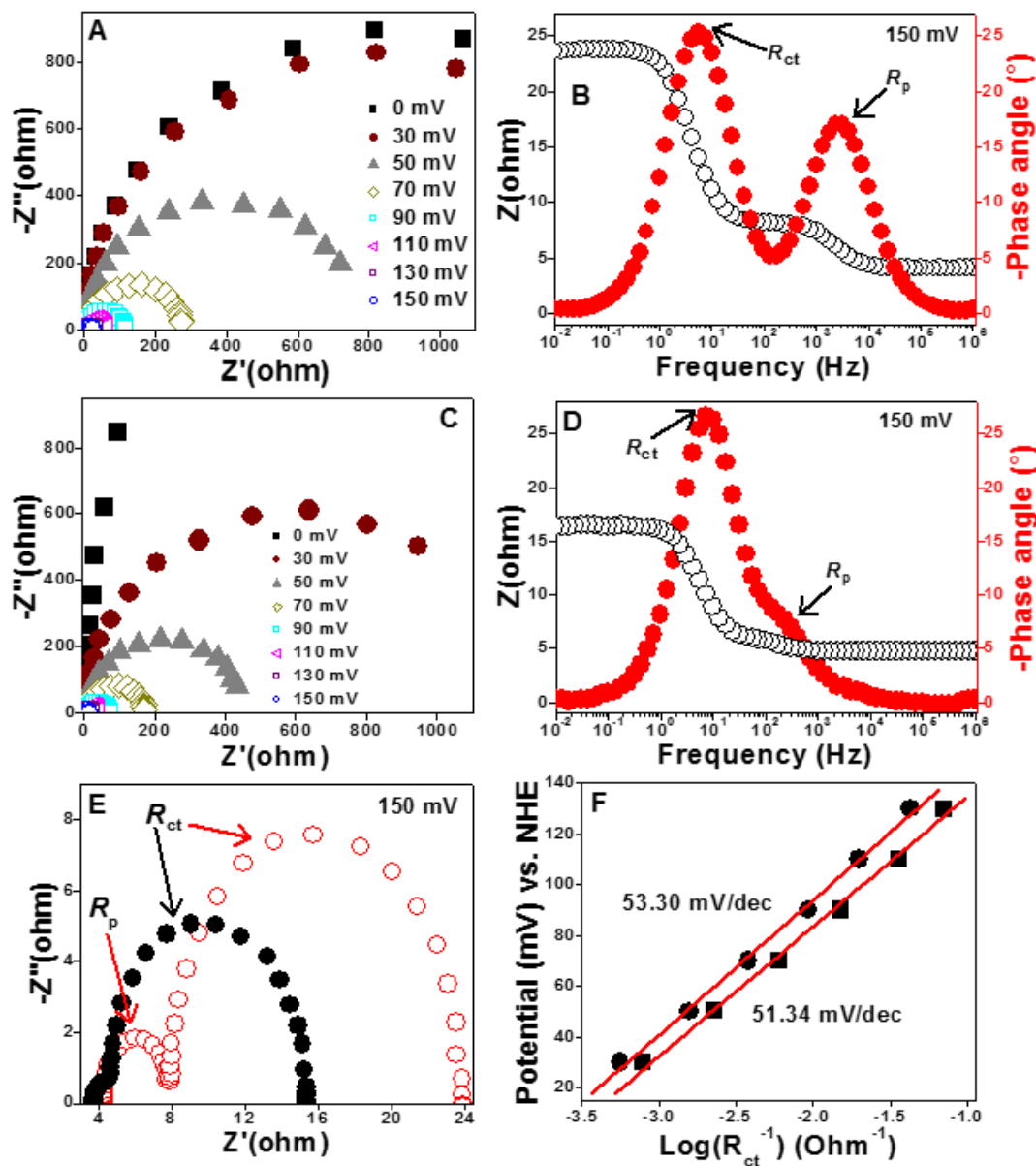


Figure 40: Nyquist and Bode plots for Mo₂C/CNT: (A) & (B) – prepared in the absence of oxalic acid, (C) & (D) – prepared in the presence oxalic acid. (E) Enlarged view of Nyquist plots showing two semicircles, (F) comparative Tafel plots for Mo₂C/CNT prepared with (51.3 mVdec⁻¹) and without (53.3 mV/dec⁻¹) oxalic acid.

Mo₂C/CNT prepared with and without oxalic acid are shown in Figure 42. BET surface area was measured to be 93.7 and 76.3 m²g⁻¹ respectively, while the electrochemically active area was determined to be 53 and 22 mFcm⁻².

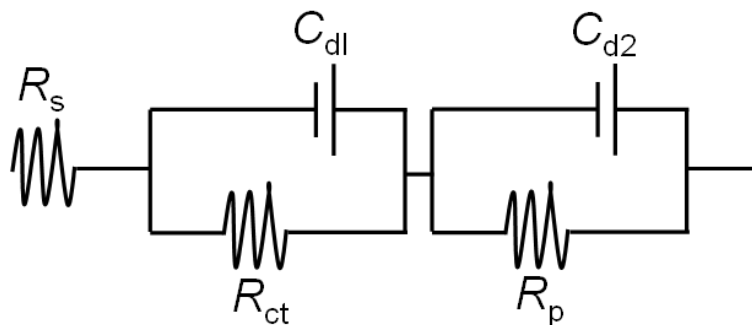


Figure 41: Two-time constant electrical equivalent circuit model utilized to fit the electrochemical impedance(EIS) results of hydrogen evolution reaction. R_s – series resistance, C_{dl} and C_{d2} are double layer capacitance, R_{ct} – charge transfer resistance for HER, R_p – resistance related to the surface porosity.

Cyclic voltammograms (CVs) of Mo₂C/CNT electrocatalysts recorded at different scan rates from 5 to 100 mVs⁻¹, and their corresponding plots of the current density at 0.248 V_{RHE} vs. scan rate are shown in Figure 43. Higher C_{dl} indicated higher EASA. Both BET and EASA results further substantiated EIS findings and reinforce that oxalate-derived Mo₂C/CNT is endowed with more active sites, a desirable feature for high-performance catalysts.

Stability of oxalate-derived Mo₂C/CNT was investigated under the identical experimental conditions – Mo₂C/CNT with 50 wt% Mo, catalyst loading 1 mg.cm⁻², 0.5 M H₂SO₄. Two experimental modes were exercised to assess the stability of electrodes – (1) chronoamperometry and (2) chronopotentiometry. Former was performed between 0.100 and -0.285 V V_{RHE} with a scan rate of 20 mVs⁻¹ for 1000 cycles, while chronopotentiometry

was conducted at 110 mV for approximately 15 h. After 1000 cycles, the used electrode was re-polarized and the current density was quantified as a function of potential.

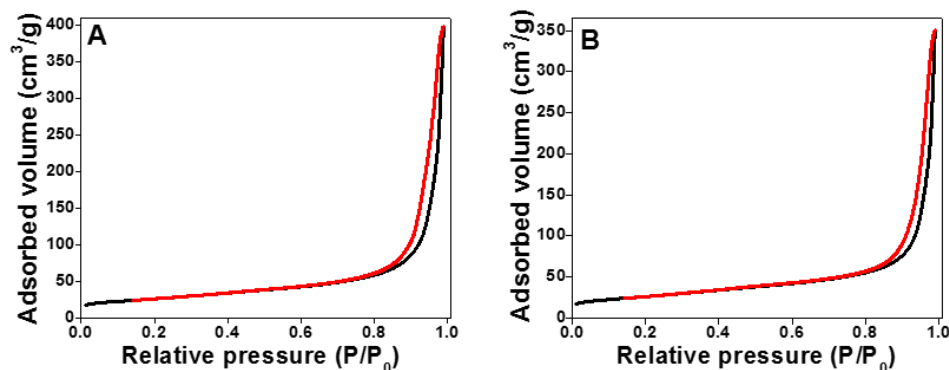


Figure 42: N₂ adsorption-desorption isotherms of Mo₂C/CNT prepared in the presence (A) and absence (B) of oxalic acid.

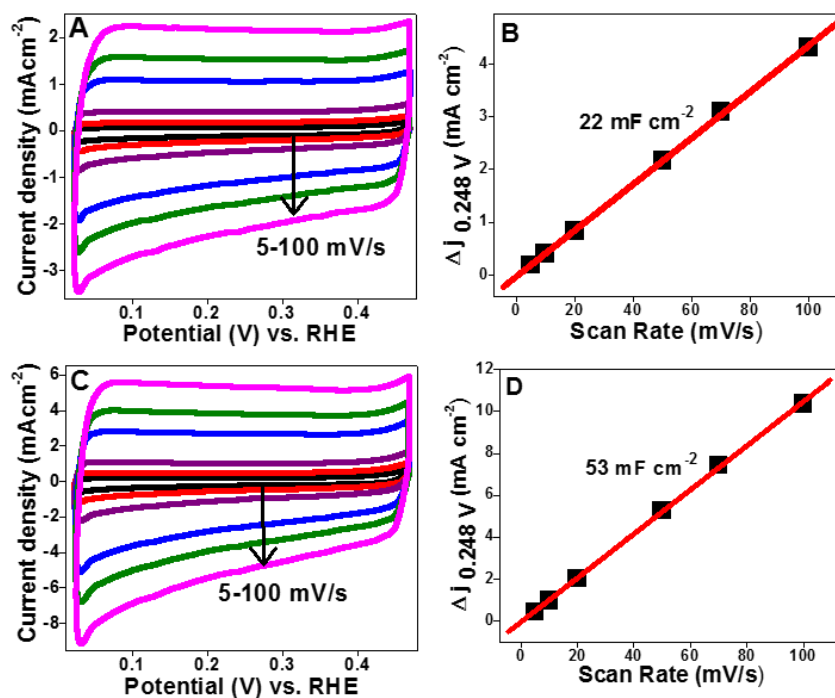


Figure 43: Cyclic voltammograms (CVs) of Mo₂C/CNT recorded at different scan rates from 5 to 100 mVs⁻¹, and their corresponding plots of the current density at 0.248 V_{RHE} vs. scan rate. (A) & (B) – prepared in the absence of oxalic acid, (C) & (D) – prepared in the presence oxalic acid.

The polarization profiles (current density vs. potential) recorded before and after 1000 cycles are shown in Figure 37E. The required overpotential to drive a current density of 10 mA remained almost intact after 1000 cycles, highlighting the durability of the electrode. On the other hand, the time-dependent profile of current density obtained at static overpotential of 110 mV is delineated in Figure 37F. Evidently, a steady current generation was noted and drop in current density was insignificant after 15 h, implying the stability of Mo₂C/CNT electrode under applied electrochemical conditions. Re-polarization of electrode after potentiostatic experiment did not indicate any noticeable alteration in the requirement of η to produce equal magnitude of current.

Tafel slopes deduced from EIS measurements are shown in Figure 40F. Although Tafel slopes of polarization curve are good indicative of the operative mechanism in HER reaction [30, 34, 83], the selection of inappropriate region of the polarization curve could lead to equivocal interpretation and consequently the HER mechanism. However, Tafel values obtained through EIS measurements are more valid. Calculation of the semi-logarithmic values of the inverse of R_{ct} against η resulted in a linear relationship with a gradient, which corresponds to the Tafel slope of 51.34 and 54.30 mVdec⁻¹ for Mo₂C/CNT prepared with and without oxalic acid, respectively. These values indicate that Volmer-Heyrovsky mechanism was operative in HER in the case of both the electrocatalysts. In lieu of this, the rate determining step is the step III, which is an electrochemical desorption as given below:

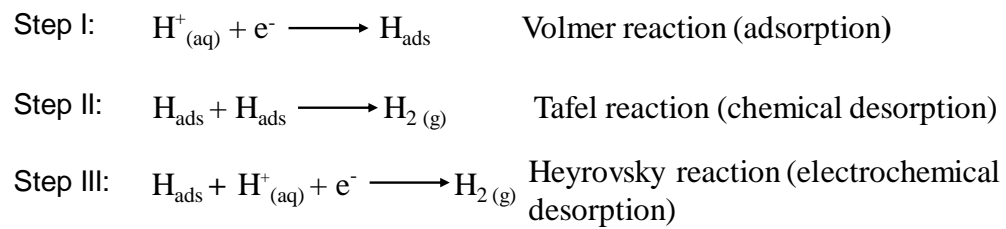


Table 2: Comparison of electrocatalysts (Mo₂C) for HER.

Catalysts	Electrolyte	η at 10 mAcm ⁻² (mV)	Tafel slope (mVdec ¹)	Catalyst loading (mgcm ⁻²)
α -Mo ₂ C [16]	0.5 M H ₂ SO ₄	198	56	0.102
α -Mo ₂ C [16]	1 M KOH	176	58	0.102
Mo ₂ C/CNT [119]	0.1 M HClO ₄	250	251	8.2
Mo ₂ C/CXG [119]	0.1 M HClO ₄	170		6.3
Mo ₂ C/CNT [35]	0.5 M H ₂ SO ₄	190	63	0.66
Mo ₂ C/CNT-GR [35]	0.5 M H ₂ SO ₄	130	58	0.66
Mo ₂ C/GR [34]	0.5 M H ₂ SO ₄	242	82	0.66
Mo ₂ C/CNT [34]	0.1 M HClO ₄	152	55.2	2.0
Bulk Mo ₂ C [34]	0.1 M HClO ₄	~300	87.6	2.0
3DHP-Mo ₂ C [15]	0.5 M H ₂ SO ₄	97	60	0.28
Mo ₂ C/NCNTs [120]	0.5 M H ₂ SO ₄	147	71	3.0
Mo ₂ C/CNTs [120]	0.5 M H ₂ SO ₄	179	65	3.0
Mo ₂ C/RGO [121]	0.5 M H ₂ SO ₄	130	57.3	0.285
MoC _{x-2} [122]	0.5 M H ₂ SO ₄	160	93	0.354
Mo ₂ C nanowires [33]	0.5 M H ₂ SO ₄	200	52	0.21
Mo ₂ C/CC [123]	0.5 M H ₂ SO ₄	140	124	1.5
Mo ₂ C [112]	0.1 M HClO ₄	>250	120	0.28
Mo ₂ C [16]	1 M KOH	176	58	0.102
Mo ₂ C-carbon [106]	0.05 M H ₂ SO ₄	>270	-	0.25
Mo ₂ C [124]	1 M H ₂ SO ₄	~210	56	1.4
Mo ₂ C [124]	1 M KOH	~190	54	0.8
Mo ₂ C/C [131]	1 M KOH	165	66.41	1.0
Mo ₂ C/C [52]	0.5 M H ₂ SO ₄	142	53	-
Mo ₂ C/C [52]	1 M KOH	151	59	-
Mo ₂ C/GR [82]	0.5 M H ₂ SO ₄	150	57	0.8
Mo ₂ C/NCF [129]	0.5 M H ₂ SO ₄	144	55	0.28
Mo ₂ C/NC [130]	0.5 M H ₂ SO ₄	136	68.4	2.0
Mo ₂ C/G [133]	0.5 M H ₂ SO ₄	135	58	0.27
MoC-Mo ₂ C [134]	0.5 M H ₂ SO ₄	126	43	-
MoC-Mo ₂ C [134]	1 M KOH	120	42	-
Mo ₂ C nanotubes [135]	0.5 M H ₂ SO ₄	172	62	0.75
Mo₂C/CNT^a	0.5 M H₂SO₄	110	51.3	1.0

a= This work

4.4 Conclusion:

Designing transition-metal-based electrocatalysts for large-scale production of H_2 through water electrolysis remains at the forefront of electrochemical technology development. For supported catalytic systems, dispersion of active sites on support is a predominant feature that determines the performance. Here, a facile method is demonstrated to obtain uniformly dispersed and fine nanoparticulates of molybdenum carbide (Mo_2C) on carbon nanotubes (CNTs). Molybdenum reacted with oxalate forming molybdenum-oxalate complex, which presumably increases the inter-molybdenum-distance and thus inhibits the agglomeration and coalescence during crystallization.

A probable mechanism is proposed for the growth of on CNT via molybdenum-oxalate complex formation. The propensity of the catalyst towards electrocatalytic H_2 evolution reaction (HER) was tested under acidic aqueous media (0.5 M H_2SO_4). The oxalate-derived Mo_2C/CNT exhibits remarkable activity with low onset potential and overpotential, and small Tafel slope. The electrode was stable at least for 15 h under continuous hydrogen production, and the performance remained intact after 1000 potentiodynamic sweeps. The Tafel slope estimated by electrochemical impedance spectroscopy confirmed the Volmer–Heyrovsky mechanism as the rate-determining step. Effect of processing temperature, concentration of functional sites and catalyst's mass on HER was investigated. Variation in activity was rationalized in terms of electrochemical active surface area and interfacial charge transfer kinetics.

Chapter 5

Oxalate-directed growth of molybdenum phosphide on carbon nanotube as high-performance and durable electrocatalyst for hydrogen evolution reaction

5.1 Introduction:

Large-scale production of H₂ via photoelectrochemical or electrochemical processes has great prospect due to its low energy consumption, high purity of H₂ and environmentally benign features. Currently, platinum (Pt) is used as the electrocatalyst. In addition to the cost, Pt-based electrocatalysts suffer from performance loss during the course of operation as a result of catalyst degradation and corrosion of carbon support. Development of electrocatalysts alternative to Pt remains at the forefront of the technology development. Developed cathodes could be employed in photoelectrochemical and/or electrochemical water electrolysis process. Consequently, considerable amount of research is underway to develop cathodes consisting of transition metal-based electrocatalysts for hydrogen evolution reaction. A variety of materials consisting of non-precious metals, such as metal carbides [82-85], metal sulfides [30, 86] WS₂ [87], selenides [89, 90], metal nitrides [98, 137], metal oxides [99], metal borides [137], metal phosphides [55, 60, 91, 92, 94, 95, 139, 140] and so forth, have been explored aiming to reduce the overpotential of hydrogen evolution reaction (HER) [101, 102, 103, 104, 105, 141]. Although noticeable reduction in overpotential has been achieved, there exists tremendous opportunity to further push this to lower threshold (closer to Pt) [79]. Recently, transition metal phosphides are reported to show high and stable HER with lower overpotential, and endeavored as potential alternative to noble metal-based electrocatalysts. Fundamentally,

the overpotential can be substantially lowered, in first hand, by choosing appropriate composition of electrocatalysts. To this end, due to unique d-band electronic structure, molybdenum phosphide seems a potential electrocatalyst for hydrogen evolution reaction. Yet, it remains rather less investigated as HER electrocatalyst.

Here, we report a facile oxalate-mediated nonhydrolytic method for growing MoP on CNTs surface. Oxalate group mitigated the coalescence and agglomeration of MoP on CNT surface, guiding the formation of heterostructure with higher dispersion of active sites. The electrocatalytic activity of oxalate-derived MoP-CNT towards HER reaction was examined and compared with that of MoP-CNT prepared in the absence of oxalate group and benchmark electrocatalyst Pt/C. Interfacial charge transfer process was accessed and the rate-determining step was discerned employing electrochemical impedance spectroscopy.

5.2 Experimental:

5.2.1 Synthesis of MoP/CNT electrocatalyst:

Firstly, a homogeneous suspension consisting of carbon nanotubes (CNTs) and anhydrous ethanol was prepared in a closed vial. Then, a calculated amount of molybdenum chloride (MoCl_5) was dissolved, and the solution was kept under stirring for 2 h. After complete dissolution of MoCl_5 , oxalic acid and certain amount of phosphoric acid were added, and the solution was kept under stirring. The stirring was carried out at 80 °C for 12 h to achieve maximum complexation of molybdenum with oxalate group ($\text{C}_2\text{O}_4^{2-}$). After reaction, vial was opened and ethanol was allowed to evaporate under a vigorous stirring, leaving behind a black powder. The resulting product was dried in oven

at 110 °C for overnight, and finally carburized in a tubular furnace in the flow of H₂/Ar mixture (10:90) at desired temperature (with a heating rate of 5 °C/min) for 2 h. The flow of mixture gas was maintained 100 mL/min with mass flow controller (Alicat) throughout the calcination process. After the reaction, the black product was collected and used as electrocatalyst for HER reaction. For comparison, MoP/CNT was also synthesized without oxalic acid following identical conditions.

5.2.2 Characterization:

Morphological and detailed microstructural attributes of the materials were discerned with the aid of field emission scanning electron microscope (FE-SEM, Tescan Lyra-3), transmission and high-resolution transmission electron microscope and selected area electron diffraction (TEM/HR-TEM, FEI Tecnai TF20) (SAED). Other techniques employed for characterization of the samples were: X-ray diffractometry (XRD, Rigaku MiniFlex), ¹H and ¹³C nuclear magnetic resonance (NMR LAMBDA 500 spectrophotometer), BET surface area analyzer (Micromeritics ChemiSorb 2750), and X-ray photoelectron spectroscopy (XPS, Thermo Scientific ESCALAB 250Xi).

5.2.3 Evaluation of electrocatalytic activity:

Homogeneous ink solution was prepared by sonicating a suspension consisting of electrocatalyst (10 mg), water and isopropanol (30% V/V) and 37 µL of 1.66 % wt. Nafion® for approximately 30 min. A measured amount (16 µL) of ink was drop-casted on a pre-cleaned glassy carbon (GC) disc electrode (5.0 mm diameter, 0.196 cm², Pine Instruments), and the electrode was allowed to dry under air flow at ambient conditions. The deposition steps were repeated to achieve the desired catalyst loading on GC electrode. Hydrogen

evolution reaction (HER) was studied in a three-electrode cell assembly connected to a potentiostat (EG &G 273A). Saturated calomel electrode (mercury/mercury chloride, SCE) and coiled platinum mesh were used as the reference and counter electrode, respectively. A 0.5 M H_2SO_4 aqueous solution was used as working electrolyte. Linear sweep voltammetry was applied with a scan rate of 5 mV s^{-1} . The SCE electrode was calibrated against normal hydrogen electrode (NHE), and its potential was converted into NHE potential. The current density was calculated against geometric area of the glassy carbon electrode and presented after iR correction. Before and during the cathodic measurement, high purity H_2 gas was used to remove the dissolved O_2 from the solution. Electrochemical impedance spectroscopy (EIS) was performed in 0.5 M H_2SO_4 between the frequency range of 105 Hz and 0.01 Hz with ac amplitude of 10 mV. All the EIS data was normalized to geometric surface area of the working electrode.

5.3 Results and discussions:

A plausible mechanism showing complexation and nucleation with concomitant growth of MoP/CNT is illustrated in Figure 44. A rapid reaction between molybdenum chloride and ethanol produces $[\text{Cl}_2\text{OMo}(\mu\text{-OEt})_2(\mu\text{-HOEt}) \text{ MoOCl}_2]$ and HCl and/or $\text{C}_2\text{H}_5\text{Cl}$ [132]. Upon addition of oxalic acid, ion-exchange reaction takes place between ethoxy and oxalate groups producing molybdenum-oxalate complex. Formation of molybdenum oxalate complex was indicated by a change of solution color (inset figure of Figure 45B). It was confirmed by C^{13} and H^1 nuclear magnetic resonance (NMR) spectroscopic techniques (Figure 45). The NMR spectrum of oxalic acid dissolved in D_2O is shown in Figure 45A. The peak at 162.24 ppm is assigned to the resonance of carbon of

oxalate group. For comparison, the NMR spectrum of the product obtained reaction between molybdenum chloride and oxalic acid in ethanol is presented in Figure 45B. A downfield shift in the resonance of carbon was noticed; the peak shifted to 166.77 ppm due to a likely interaction between oxalate ($\text{C}_2\text{O}_4^{2-}$) and molybdenum (Mo) metal center, forming a molybdenum-oxalate complex. Moreover, only one peak for carbon was detected in both the cases. This suggested the presence of similar coordination environment around all carbon coordinated to molybdenum, and C_2 symmetry center in the complex. The possibility of any proton coordinated to this molybdenum-oxalate complex was corroborated by ^1H NMR as shown in Figure 45 C. Only one resonance peak at 4.6 ppm corresponding to deuterated solvent was recorded, implying the absence of any proton in the molybdenum-oxalate complex. Due to rather bulky nature of oxalate group, a disseminated self-assembling of molybdenum with defined inter-atomic-distance is likely. This discrete molecular assembly seems to mitigate the agglomeration of molybdenum and steer a controlled nucleation and growth. When heated, molybdenum oxalate decomposes and molybdenum reacts with PO_4^{3-} forming molybdenum phosphate. At higher temperature, molybdenum phosphate is reduced and transformed into molybdenum phosphide. All these processes occurred onto the surface of CNTs.

Powder X-ray diffractions (XRD) of oxalate-derived MoP is presented in Figure 46. The diffraction peak at 26.1° corresponds to 002 plane of CNTs, while diffractions centered at 27.9° (001), 31.2° (100), 43.1° (101), 57.5° (110), 65.0° (111), 67.0° (102), and 74.3° (201) are indexed to MoP with a hexagonal closed packed structure (PDF-24-0771) [141]. (P6m2) in which Mo 6-coordinated by P atoms. XRD analysis MoP prepared without oxalic acid did not show any noticeable difference as compared to oxalate-derived MoP.

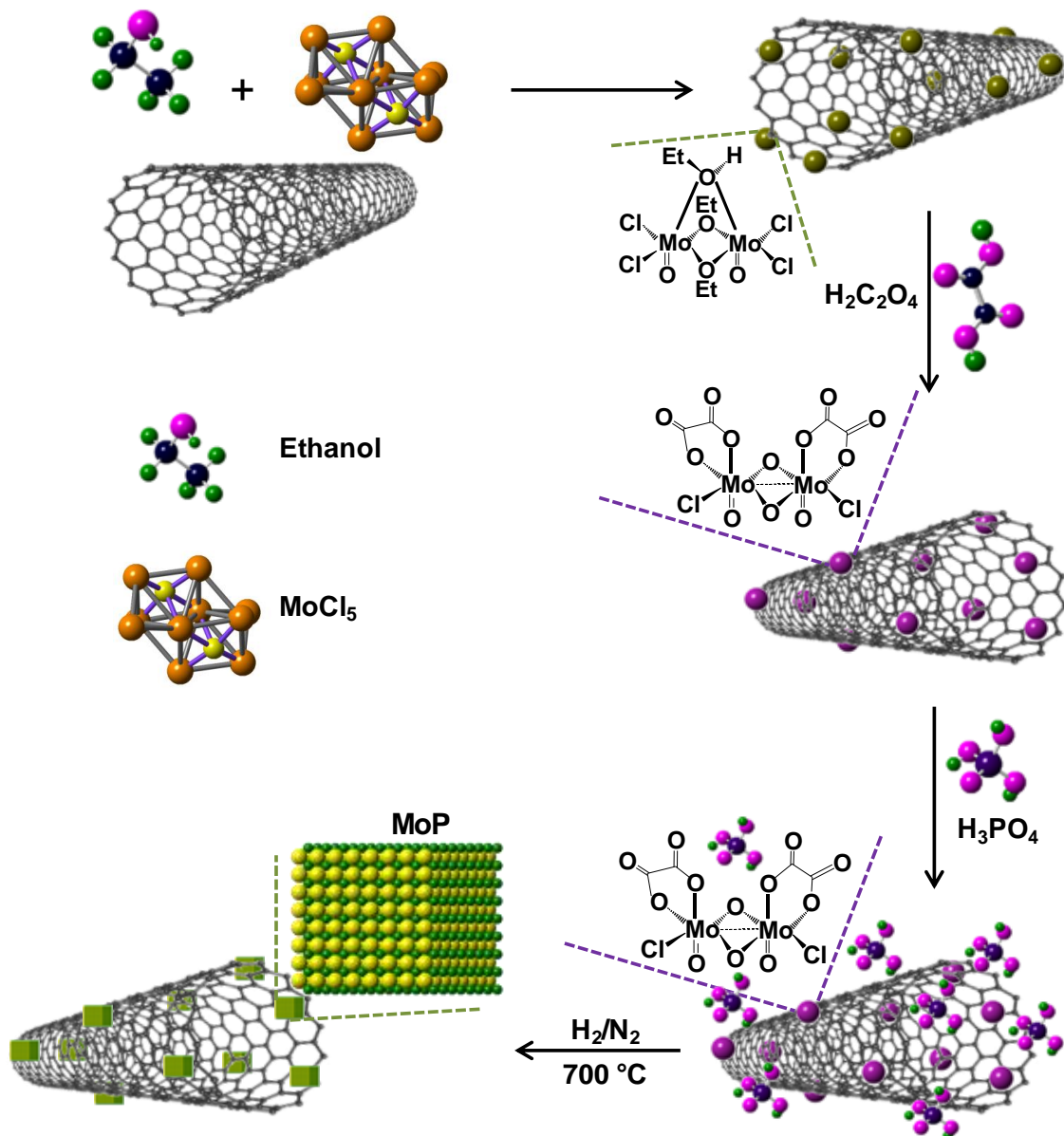


Figure 44: A representative scheme shows proposed reaction mechanism steps; complexation, nucleation and concomitant growth of MoP on CNT surface.

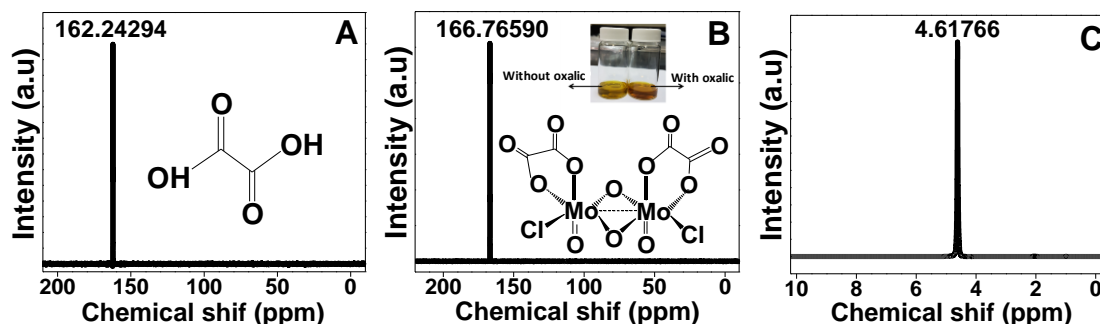


Figure 45: ^{13}C NMR of (A) solution of $\text{H}_2\text{C}_2\text{O}_4$ and $\text{C}_2\text{H}_5\text{OH}$ and (B) solution of MoCl_5 , $\text{H}_2\text{C}_2\text{O}_4$ and $\text{C}_2\text{H}_5\text{OH}$, inset photographs showing the change in color of MoCl_5 and ethanol solution after addition of oxalic acid, and ^1H NMR of (C) solution of MoCl_5 , $\text{H}_2\text{C}_2\text{O}_4$ and $\text{C}_2\text{H}_5\text{OH}$.

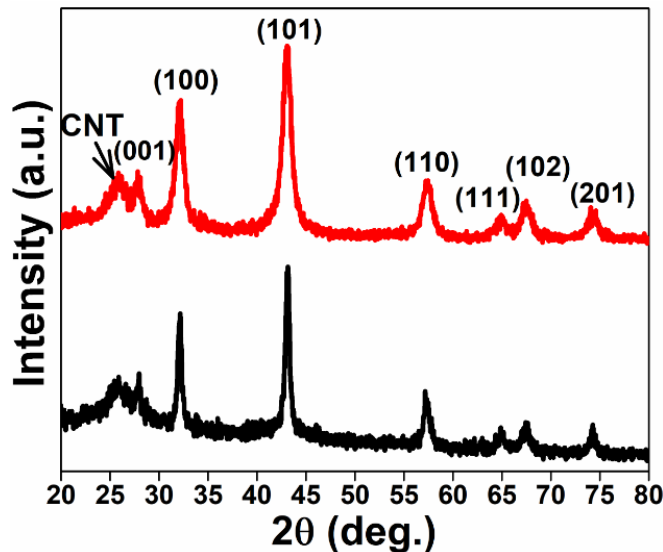


Figure 46: Comparative XRD of MoP/CNT prepared without oxalic acid (black) and prepared with oxalic acid (red).

Details of chemical composition and oxidation states of electrocatalyst were obtained by XPS. Elemental survey spectrum and Signatures of C 1s, Mo 3d and P 2p of as-synthesized MoP are shown in Figure 47a, b, c and d, respectively. XPS survey confirms the presence of carbon, molybdenum, phosphorous and oxygen in the sample. Besides the presence of graphitic carbon at 284.7 eV, characteristic signal of C–O (at 285.7 eV) was

also detected. XPS spectrum in the Mo 3d region suggests the presence of Mo in different oxidation states. Peaks centered at ~235.6 and 232.4 eV account for Mo 3d_{3/2} and Mo 3d_{5/2} of Mo⁶⁺ (MoO₃) spectral lines, which agrees well with those reported MoP. Although located at slightly higher value than that of metallic Mo, peaks at 228.4 and 231.6 eV account for MoP [62, 141, 142].

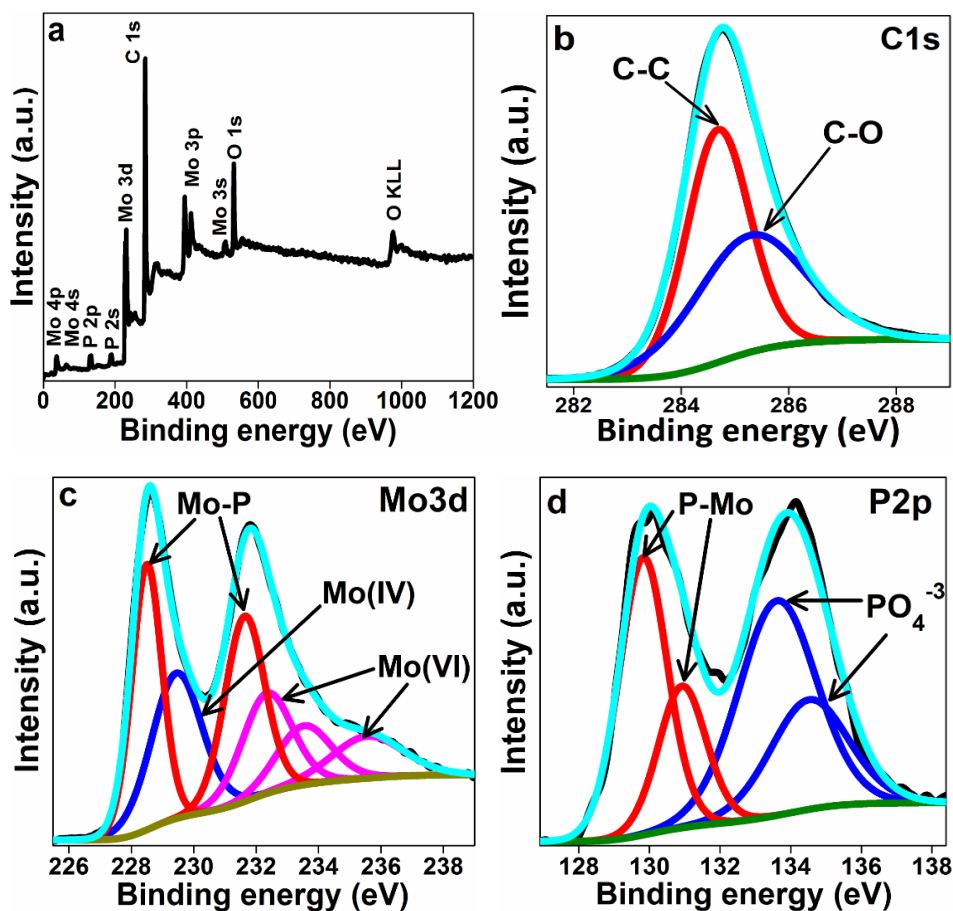


Figure 47: XPS spectra of; (a) Survey of MoP/CNT, (b) C1s, (c) Mo3d and (d) P 2p.

In addition, peaks at binding energies of 229.3 and 232.3 eV are attributed to oxides of molybdenum. The surface of MoP is susceptible to oxide (MoO₂ and MoO₃) formation when exposed to air atmosphere. Formation of oxides has been observed in previous studies [113, 114]. The morphology and dispersion of MoP on CNTs are highlighted in

Figure 48. The morphology of CNTs was retained at high processing temperature such as 700 °C. For comparison, morphological and dispersion qualities of MoP prepared in the absence and presence of oxalic acid was examined by TEM. Microscopy images shown in Figure 48a highlights the size, morphology, and homogeneity of MoP obtained without oxalic acid.

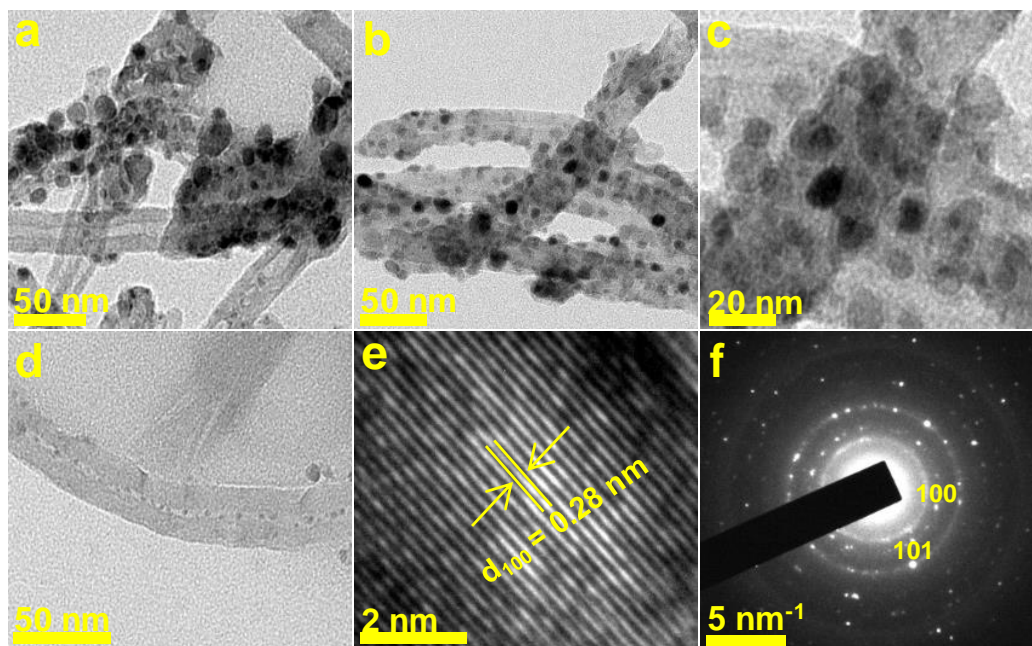


Figure 48: TEM images of (a) MoP/CNT without oxalic acid, (b-d) MoP/CNT with oxalic acid, (e) HRTEM and (f) SAED

Scanning revealed a wide particle size distribution, between 5 and 20 nm, of MoP on CNT. Contrary, particles of oxalate-derived MoP were near-spherical shape and uniformly distributed with size in the range between 5 and 15 nm (Figures 48b and c). Furthermore, some of MoP particles seemed to grow inside the carbon nanotubes (Figure 48d). Highly uniform and ultrafine size (~ 2 nm) implies that MoP nucleation and growth occurred inside the tubular confinement. Microscopy observations reinforce our assumption that complexation of molybdenum with oxalate renders discrete inter-molybdenum-complex-

distance, and thus controlled nucleation and growth of MoP nanoparticles. This led to the formation of fine and uniformly dispersed MoP on CNT. Distribution of C, O, P and Mo and in oxalate-derived MoP/CNT was mapped, and results are shown in Figure 49. Molybdenum seemed to be evenly distributed throughout the surface. The electron diffraction and the HR-TEM microscopy images (Figures 48e and f) show polycrystalline nature of sample with high degree of crystallinity. The interplanar distance was estimated to be 0.28 nm, which corresponds to (100) plane. This is in good agreement with 0.28 nm, obtained from XRD diffraction peak at 31.2° .

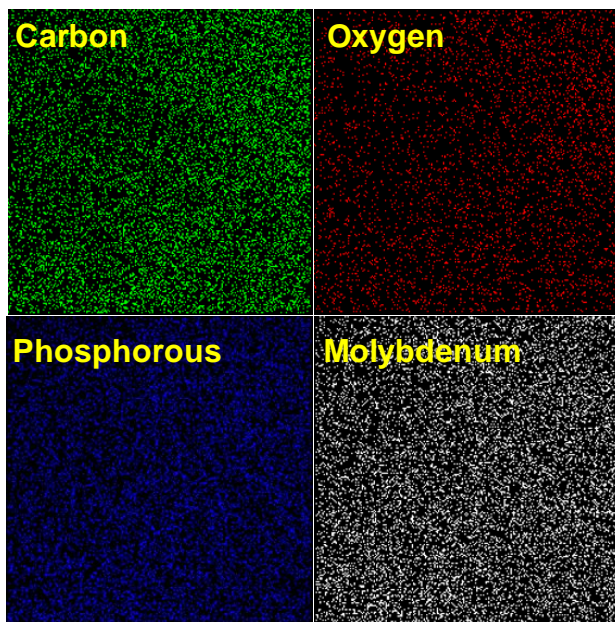


Figure 49: Elemental mapping of carbon, oxygen, phosphorous and molybdenum present in MoP/CNT.

Performance of as-synthesized electrocatalysts was tested towards hydrogen evolution reaction from water, both in 0.5 M H_2SO_4 and 1.0 M KOH aqueous solutions. The current density is normalized to geometric area of the glassy carbon electrode. Before recording the linear sweep voltammograms, working electrodes were swept for 10 cycles

between +0.1 and -0.3 V to allow interface to attain equilibrium, if any. Performance of oxalate-derived MoP/CNTs was compared with that of MoP/CNT, obtained without oxalic acid, and Pt/C. Comparative electrocatalytic performance was carried out under identical experimental conditions with same mass of catalyst loading on GC electrode. Cathodic polarization (current density vs. potential) profiles under acidic and basic media are shown in Figures 50a and b, respectively. Under acidic conditions, the overpotentials, recorded to produce current density of 10 mA cm^{-2} , for Pt/C, oxalate-derived MoP/CNT and MoP/CNT (without oxalic acid) were ~41, ~115 and ~160 mV, respectively. Overpotential of oxalate-derived MoP/CNT compares favorably to other Pt-less electrocatalysts under acidic medium (Table 2). A similar activity trend, though requiring higher potential, was discerned under basic media. For the identical current density, respective potentials were calculated to be ~65, ~170 and 220 mV. As expected, commercial Pt/C exhibited the best HER activity. Oxalate-derived electrocatalyst required much lower potential as compared to that of MoP/CNT prepared in the absence of oxalic acid. This could presumably be attributed to smaller size and improved dispersion of active sites, as observed through microscopy. Besides the number of increased active sites, improved dispersion on support is likely to influence specific surface area owing to its smaller size. In addition, it could also affect surface-charge-resistance and electrochemical active surface area.

In order to gain further insights into improved performance of oxalate-derived sample, BET surface area, charge transport behavior and electrochemical active surface area were investigated. Specific surface area of MoP/CNT, prepared with and without oxalic acid, was measured to be 72.4 and $61.8 \text{ m}^2\text{g}^{-1}$ respectively. Higher surface area could

presumably be due to smaller particle size of MoP. Respective nitrogen sorption isotherms are shown in Figure 52.

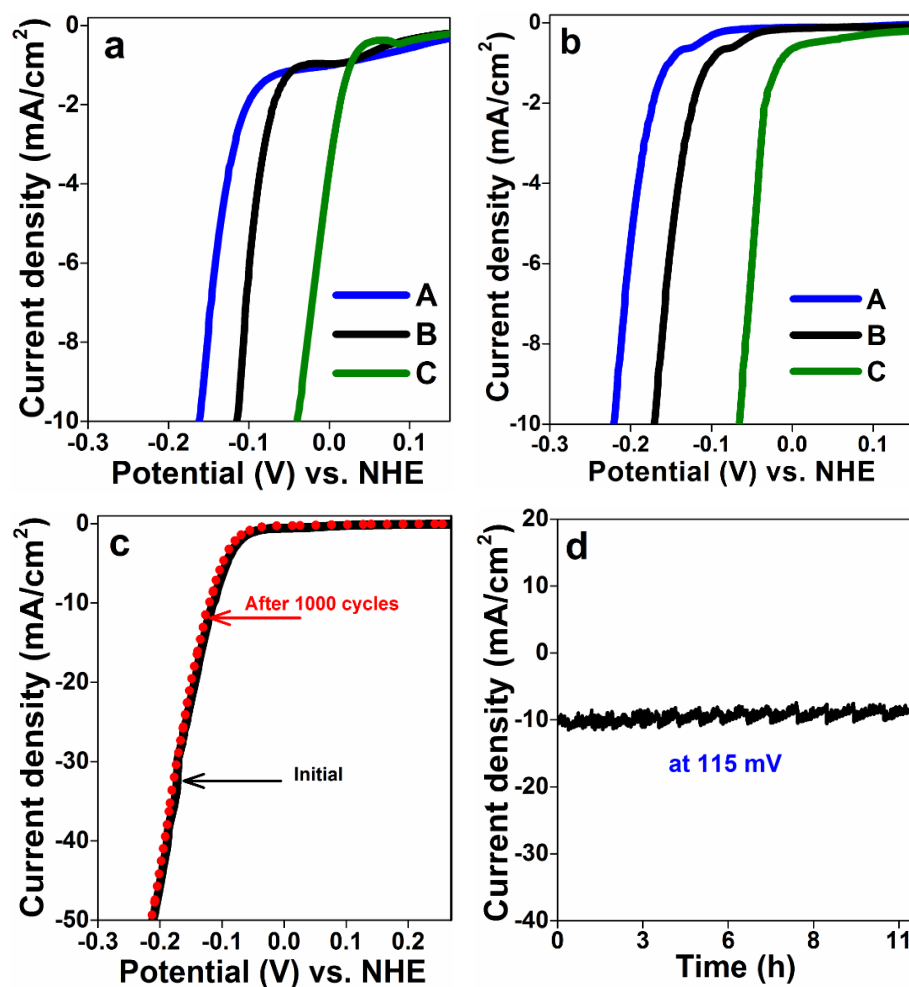


Figure 50: a) Linear sweep voltammograms of A- MoP/CNT prepared in absence of oxalic acid, B- prepared in presence of oxalic acid and C- Pt/C recoded in 0.5M H_2SO_4 and (b) recorded in 1M KOH solution. c) Polarization curves before and after 1000 sweeps and d) a time-dependent profile of current density at $\eta = 115 \text{ mV}$ for 11 h

Bulk conductivity as well as surface-charge-resistance of MoP/CNT nanocomposites were investigated by employing electrochemical impedance spectroscopy (EIS). Measurements were conducted in the frequency range of 105 - 0.01 Hz with an AC amplitude of 10 mV in 0.5 M H_2SO_4 aqueous solution. For electrochemical hydrogen

evolution reactions, EIS findings are predominantly explained by three types of electrical equivalent circuit models; one-time constant model [116], two-time constant parallel model [34, 117] and two-time constant serial models [118]. Herein, the two-time constant parallel model consisting of solution resistance (R_s) in series with two parallel constant phase element-resistance was used to fit the experimental data (Figure 41). According to this equivalent circuit model, R_s is a collective resistance, which incorporates resistances from wiring (R_{wiring}), carbon support (R_{carbon}), MoP (R_{MoP}) and solution (R_{solution}) [118]. Furthermore, charge transfer resistance and capacitance are denoted by R_{ct} and C_{dl} , respectively. Representative potential-dependent Nyquist plots (real vs. imaginary impedance) are shown in Figure 51a and b, respectively. Plots were constructed as a function of overpotential ($\eta = 0, 30, 50, 70, 90, 110, 130$ and 150 mV). The semicircular dispersion of impedance is characteristic of an interfacial phenomenon occurring near the electrode surface. Shorter semicircular arcs imply faster charge transfer at the interface and vice versa. As evident, surface-charge-resistance (R_{ct}) was found to be a function of overpotential. R_{ct} decreases with increasing overpotential, implying faster charge transfer kinetics at higher η . Furthermore, R_{ct} , at all applied potentials, in oxalate-derived MoP/CNT were enumerated to be lower as compared to that of prepared in absence of oxalic acid. For instance, an enlarged view of Nyquist plots constructed with $\eta = 150$ mV for both the electrocatalysts is compared in Figure 51c. R_{ct} was smaller ($\sim 19 \Omega$) in oxalate-derived MoP/CNT than that of obtained in the absence of oxalic acid ($\sim 30 \Omega$). In addition to smaller R_{ct} , Nyquist plots indicated the presence of two semicircles or two-time constants. This was corroborated by Bode plots - corresponding Bode plots obtained at $\eta = 150$ mV are shown in Figures 51d. Nyquist as well as Bode data constitute two

semicircles, though it was much more perceptible in oxalate-derived MoP/CNT. The semicircle recorded at higher frequency originates from surface porosity, while the near-semicircle appeared at lower frequency accounts for charge transfer involved in hydrogen evolution reaction. Similar findings are reported earlier [118].

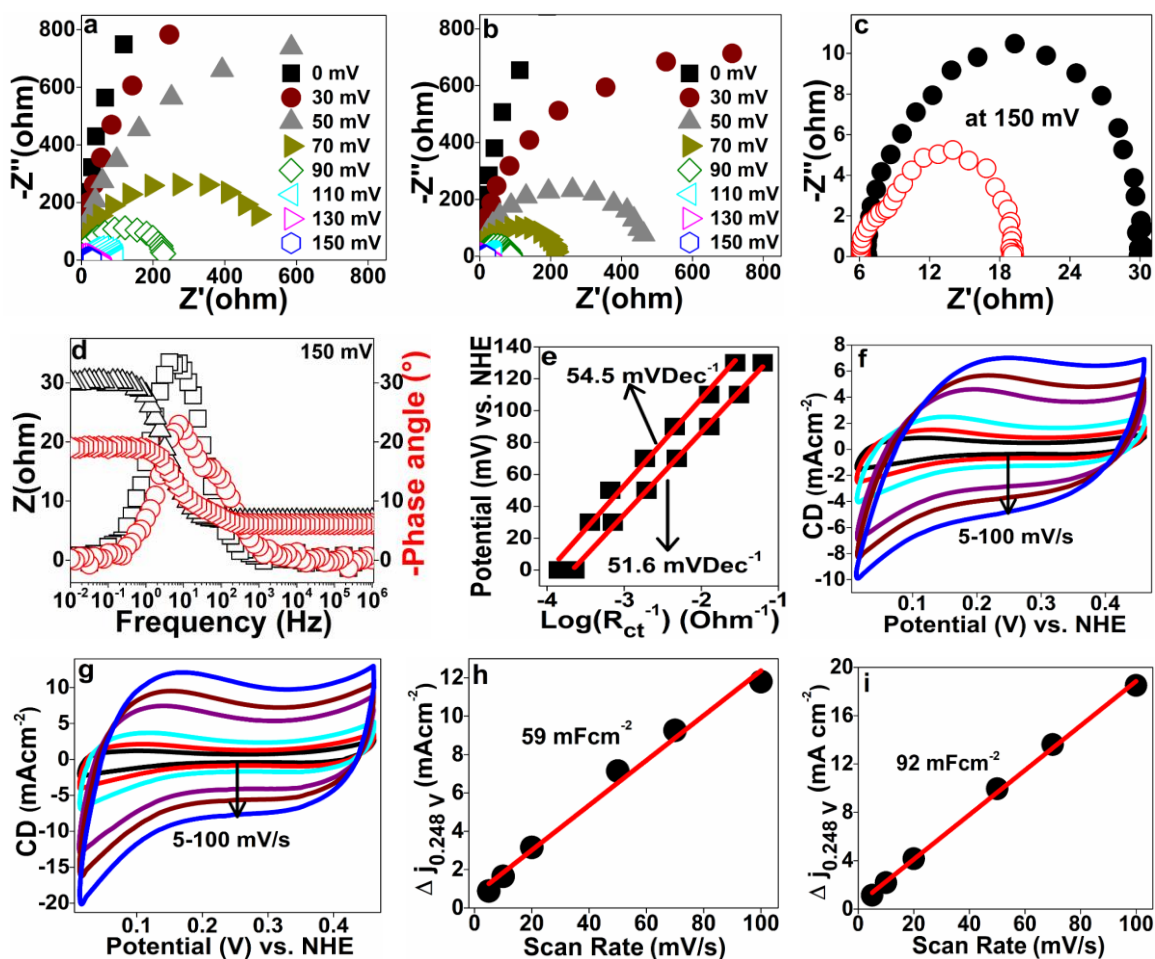
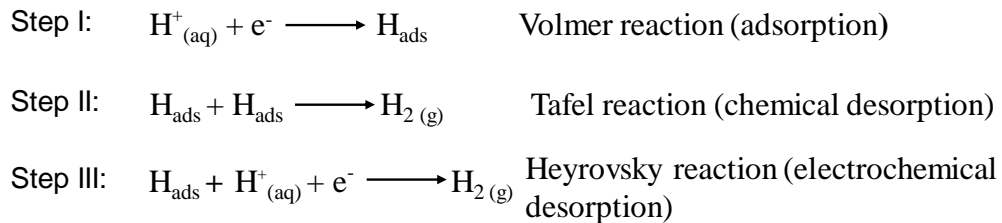


Figure 51: Nyquist plots for MoP/CNT: (a)– prepared in the absence of oxalic acid, ((b))– prepared in the presence oxalic acid. (c) Enlarged view of Nyquist plots showing two semicircles, and (d) their comparative Bode plots at $\eta = 150$ mV. (e) comparative Tafel plots for MoP/CNT prepared with (51.6 mVdec $^{-1}$) and without (54.5 mV/dec $^{-1}$) oxalic acid. (f) & (g) Cyclic voltammograms of MoP/CNT recorded at different scan rates from 5 to 100 mVs $^{-1}$, and (h) & (g) their corresponding plots of the current density at 0.248 V $_{RHE}$ vs. scan rate. CVs were recorded in non-faradic region. The linear slopes are equivalent to twice of the electrochemical double layer capacitance (C_{dl}).

Under acidic conditions, HER reaction proceeds via two different pathways involving three probable reactions – (1) Volmer reaction (adsorption), (2) Tafel reaction (chemical desorption) and (3) Heyrovsky reaction (electrochemical desorption). The operative mechanism could be determined by estimating Tafel slope, either from polarization curve or EIS measurements. Although Tafel slope computed from polarization curve is well-founded [19, 143, 144], selection of inappropriate region of polarization curve could lead to ambiguous interpretation and consequently the HER mechanism. However, Tafel values obtained through EIS measurements are more persuasive [144]. Tafel slopes, therefore, were calculated from EIS results to determine the reaction mechanism (Figure 51e). Calculation of the semi-logarithmic values of the inverse of R_{ct} against η resulted in a linear relationship with a gradient, which is attributed to the Tafel slope of 51.6 and 54.5 mV dec⁻¹ for MoP/CNT synthesized with and without oxalic acid, respectively. Such values imply that Heyrovsky mechanism was operative, and the rate determining step was electrochemical desorption as described by following equations:



Since electrochemical hydrogen evolution reaction is a predominantly surface-dictated process, usually high surface area (specific and electrochemical active surface area (EASA)) of electrocatalysts is desirable. Specific surface area was measured by BET method, whereas electrochemical active area was quantified through the measurement of double layer capacitance (C_{dl}) of cyclic voltammograms (CVs). CVs were recorded at

different scan rates from 5 to 100 mVs⁻¹. CVs together with corresponding plots for MoP/CNT prepared in the absence and presence of oxalic acid is shown in Figures 51f, g, h and i. Electrochemical active areas were determined to 59 and 92 mFcm⁻², respectively. Usually, higher C_{dl} is discerned as higher EASA and thus activity. Although MoP prepared without oxalic acid had higher C_{dl} or electrochemical active area, oxalate-derived electrocatalyst exhibited better performance.

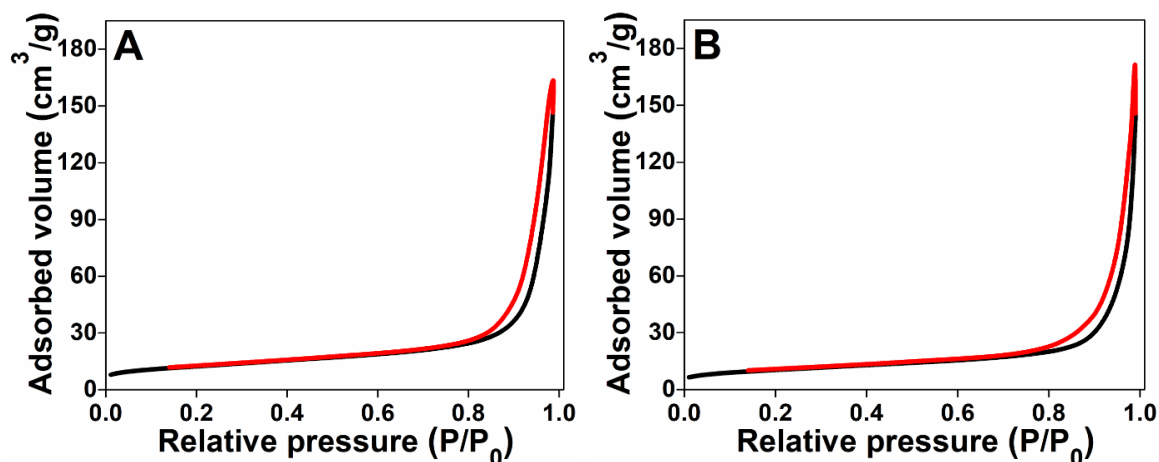


Figure 52: N₂ adsorption-desorption isotherms of MoP/CNT prepared in the presence (A) and absence (B) of oxalic acid.

Durability of oxalate-derived electrode was investigated under identical experimental conditions; MoP/CNT with 50 wt% Mo, catalyst loading 1 mg.cm⁻², 0.5 M H₂SO₄. Two assessment methods were pursued to evaluate the stability of the electrode; (1) chronoamperometry (between 0.1 and -0.285 V_{RHE} with a scan rate of 20 mVs⁻¹ for 1000 cycles) and (2) chronopotentiometry (at overpotential of 115 mV for approximately 15 h). After 1000 scans, the used electrode was re-polarized and the current density was quantified as a function of potential. The polarization curves (current density-potential curve) before and after continuous cycles are compared in Figure 50c. The required overpotential to produce similar current density remained almost intact after 1000 cycles,

indicating excellent endurance of the electrode. On the other hand, the time-dependent profile of current density at constant applied potential of 115 mV is depicted in Figure 50d. A steady current flow was recorded and the drop in current density was insignificant after 15 h. Moreover, re-polarization of electrode after potentiostatic measurement did not indicate any noticeable modification in the requirement of η to produce equal magnitude of current density.

Table 3: Comparison of electrocatalysts (MoP) for HER in acidic medium.

Catalysts	Electrolyte	Overpotential at 10 mA cm ⁻² (mV)	Tafel slope (mV/dec)	Catalyst loading (mg/cm ²)
Graphite-MoP [145]	0.5 M H ₂ SO ₄	260	63	0.64
MoP/SN [146]	0.5 M H ₂ SO ₄	104	45	0.5
MoP/SNG-20 [146]	0.5 M H ₂ SO ₄	99	54	0.5
MoP/CC [147]	0.5 M H ₂ SO ₄	148	55	-
Amorphous MoP/Ti [148]	0.5 M H ₂ SO ₄	110	45	1
MoP [149]	0.5 M H ₂ SO ₄	150	50	0.1
Bulk MoP [65]	0.5 M H ₂ SO ₄	140	54	0.68
MoP flakes [150]	0.5 M H ₂ SO ₄	141	71.8	1.425
Bulk MoP [151]	0.5 M H ₂ SO ₄	246	60	0.071
MoP NP [67]	0.5 M H ₂ SO ₄	125	54	0.63
3D MoP sponge [141]	0.5 M H ₂ SO ₄	105	126	0.35
MoP/porous carbon [152]	0.5 M H ₂ SO ₄	126	68.5	0.243
MoP/rGO [153]	0.5 M H ₂ SO ₄	119	58	0.337
MoP/NP-CNTs [154]	0.5 M H ₂ SO ₄	116	51	3
MoP/CC [155]	0.5 M H ₂ SO ₄	124	58	2.5
MoP/NC [156]	0.5 M H ₂ SO ₄	115	65	2
MoP ₂ /Mo [157]	0.5 M H ₂ SO ₄	143	57	0.18
MoP/rGO [158]	0.5 M H ₂ SO ₄	152	88	1.6
MoP/CF [142]	0.5 M H ₂ SO ₄	200	56.4	0.36
MoP/PC [159]	0.5 M H ₂ SO ₄	153	66	0.41
MoP/CNT^a	0.5 M H₂SO₄	115	51.6	1

a= This work

5.4 Conclusion:

In conclusion, a novel method is demonstrated to form ultrafine and uniformly dispersed MoP on CNT surface. In this method, the highly complexing agent oxalate group played a vital role to impede the agglomeration & coalescence and offer controllable nucleation & growth of MoP nanocrystals. A plausible mechanism involving complexation, nucleation with concomitant growth of MoP on CNT surface was proposed. Oxalate-derived MoP/CNT shows high electrocatalytic hydrogen evolution performance and strong stability in acidic medium. promoted catalytic activity was originated from the following attributes; high dispersion of active sites improved the surface area & exposed more catalytic sites and rapid charge surface capability feature can lead to efficient HER reaction. The catalytic mechanism was determined by kinetic parameter

CHAPTER 6

Hollow and Interconnected Scaffold of CoP and Carbon Nanotubes as High Performance Electrocatalyst for Hydrogen Evolution Reaction

6.1 Introduction:

The prospects of global energy demand and adverse climate change are driving scientists to explore sustainable and eco-friendly sources of energy. In this context, molecular hydrogen (H_2) is perceived as one of the most potential future energy carriers, owing to its highest gravimetric energy density. In addition, use of H_2 as an energy carrier is environmentally benign – produces only water as the by-product. Currently, large-scale production of H_2 is achieved through steam–methane reforming ($CH_4 + H_2O \rightleftharpoons CO + 3H_2$). This is an energy-intensive process and consumes fossil fuel and, more importantly, adds to CO_2 emission through water – gas shift reaction ($CO + H_2O \rightleftharpoons CO_2 + H_2$). One of the potential pathways, based on carbon-free footprints, to generate a high - flow of hydrogen is through electrocatalysis [12, 77, 79, 160]. However, the technological development of water electrolysis to achieve a high flow rate of hydrogen is essentially decelerated by the requirement of high overvoltage. Development of a catalyst that can lower the overpotential for hydrogen generation could contribute substantially to the overall electrocatalytic process. Currently, platinum (Pt) is known as a state-of-the-art electrocatalyst for hydrogen evolution reaction (HER) and oxygen reduction reaction (ORR). However, due to high cost and its instability in the electrochemical power systems,

development of Pt-less electrode materials is central to electrochemical energy conversion devices, such as photoelectrochemical cells, electrolyzers etc. As a result, a variety of electrode materials comprising non-precious compositions, such as carbides [34, 71, 130], sulfides [30, 87, 161], nitrides [98, 97], phosphides [55, 60, 93, 96] and borides [137, 162] of transition metals, have been explored.

The activation potential can be substantially lowered at first hand by choosing the appropriate elemental composition of electrocatalyst. This requirement can further be alleviated by designing nanostructured catalysts endowed with favorable features. It has now been established that achieving control of the architecture of nanoscaled materials could lead to the development of new materials and systems with enhanced physical and chemical properties. The potential for success lies in appropriate tailoring and engineering of the nanomaterials and their resulting devices for a given application. A number of approaches are pursued to produce engineered nanostructures, including size and shape control [163, 164] tailored composition or doping [165, 166] creating porous morphology [167, 76] and so forth. Creating porosity in electrocatalysts is interesting, particularly for hydrogen evolution reaction, as it could enhance the utilization of the active sites as well as ease the release of hydrogen molecules formed on electrode surfaces. Owing to high porosity, large surface area and most accessible active sites, low mass density, efficacious mass transport (diffusion of reactants and products), fast electrical and ionic transport, and so forth, hollow nanostructures hold great potential for a variety of technological applications including hydrogen evolution reaction [168].

Although preparation of hollow cobalt phosphide, both supported and unsupported on carbon, are reported earlier, the employed synthesis protocols were multistep. For

instance, hollow CoP supported on nitrogen-doped graphene was prepared in three steps – (1) reduction of cobalt oxide under Ar, (2) oxidation under air and (3) phosphidation in the presence of sodium hypophosphite (NaPO_2H_2) [169]. Similarly, the hollow polyhedron of CoP was produced by pyrolysis of metal-organic frameworks [170].

Herein, we demonstrate a novel method to fabricate hollow CoP dispersed on carbon nanotubes (CNTs). The method is simple and single-step, which involves direct phosphidation of as-prepared cobalt–hexamethylenetetramine complex in the presence of phosphine (PH_3) gas, produced in situ from the decomposition of NaPO_2H_2 , at low-temperature. Moreover, the hollow nanospheres were predominantly interconnected, which is a desired feature from the electrical conductivity viewpoint. Endowed with such intriguing features, CoP/CNT exhibited remarkable performance for HER. Performance of electrode comprising hollow CoP/CNT was compared with those of Pt/C and non-hollow CoP/CNT, and durability was examined. Fundamental activity-regulating features, such as specific surface area, electrochemical active surface area, electrical conductivity and interfacial charge transfer kinetics, and turnover frequency, were investigated and correlated to the performance.

6.2 Experimental:

6.2.1 Synthesis of cobalt phosphide/carbon nanotubes (CoP/CNT)

electrocatalyst:

A measured amount of cobalt acetate tetrahydrate was dissolved in homogeneous suspension comprising carbon nanotubes and anhydrous ethanol in a capped vial. The

solution was kept under stirring for 2 h at room temperature. Then, hexamethylenetetramine (HMT) was dissolved, and the solution was kept under stirring for another 12 h to achieve a maximum complexation of cobalt with HMT. Subsequently, the solution was poured into a petri dish and the solvent was allowed to evaporate under a vigorous stirring. As the solvent evaporated, a black powder was obtained which was dried at 110 °C for overnight. Finally, desired amount of as-prepared powder and sodium NaPO_2H_2 were placed in two separate alumina crucibles and transferred in a tube furnace under the flow of Argon (75 mLmin⁻¹). NaPO_2H_2 was placed at the upstream side of the furnace. The furnace was raised to the desired temperature with heating rate of 5 °Cmin⁻¹, and maintained for 2 h. After the reaction, the product was collected and used as electrocatalyst for HER reaction. For comparison, non-hollow CoP/CNT was also prepared following the same method, but in the absence of HMT.

6.2.2 Characterization:

Morphological and detailed microstructural attributes of the materials were discerned with the aid of transmission and high-resolution transmission electron microscope and selected area electron diffraction (TEM/HR-TEM, FEI Tecnai TF20) (SAED). Other techniques employed for characterization of the samples were: X-ray diffractometry (XRD, Rigaku MiniFlex), ¹H and ¹³C nuclear magnetic resonance (NMR LAMBDA 500 spectrophotometer), BET surface area analyzer (Micromeritics ChemiSorb 2750) and X-ray photoelectron spectroscopy (XPS, Thermo Scientific ESCALAB 250Xi).

6.2.3 Electrochemical characterization:

Performance was evaluated in a three-electrode cell configuration connected to a potentiostat (EG&G 273A) at ambient conditions. Working electrode was prepared sonicating slurry consisting of electrocatalyst (10 mg), water and ethanol (50% V/V) and 37 μL of 1.66 % wt. Nafion® for approximately 30 min. 16 μL of sonicated solution was dropped on a pre-cleaned glassy carbon (GC) disc electrode (5.0 mm diameter, 0.196 cm^2 , Pine Instruments), and dried under ambient conditions. The deposition steps were repeated to achieve desired catalyst loading. Saturated calomel electrode (Hg/HgCl_2 , SCE) and coiled platinum wire were used as reference and the counter electrode, respectively. The SCE potential was converted and presented against normal hydrogen electrode (NHE). Linear sweep voltammetry was performed in a 1.0 M KOH or 0.5 M H_2SO_4 aqueous solution at a scan rate of 5 mV s^{-1} . All current density was normalized to the geometric area of the glassy carbon electrode and presented after iR compensation. Electrochemical impedance spectroscopy (EIS) measurements were carried out in 0.5 M H_2SO_4 between the frequency range of 10^5 Hz and 0.01 Hz with ac amplitude of 10 mV. All the EIS data was normalized to the geometric area of the working electrode. The EIS data were fitted by ZSimpWin.

6.2.4 Calculation of turnover frequency (TOF):

To elucidate the active sites, TOF was estimated using the following equation;

$$\text{TOF} = JA/2FN \quad (3)$$

Where, J (A/cm^2) is the geometric current density recorded during the LSV measurement in 0.5 M H_2SO_4 , A is the geometric area of the glassy carbon electrode GC (0.196 cm^2), $1/2$ denotes that two electrons are required to form one hydrogen molecule from water, F

is the Faradic constant (96485 Cmol^{-1}), N is the number of active sites (mol). N was determined by carrying out CV measurements between -0.2 V and $+0.6 \text{ V}_{\text{NHE}}$ in 1.0 M phosphate buffer solution with a scan rate of 20 mV s^{-1} . While it is difficult to assign the observed peaks to a given redox couple, N should be proportional to the integrated charge over the whole potential range. Assuming a one electron redox reaction, the upper limit of active sites was calculated as given by the following equation:

$$N = Q/2F \quad (4)$$

Where Q is voltammetric charge.

6.3 Results and discussions:

X-ray diffractions (XRD) of hollow and non-hollow CoP/CNT are compared in Figure 53. Similar diffractions were observed for both, indicating the formation of crystalline phase. Diffraction peaks centered at $2\theta = 31.7$ (011), 36.3 (111), 46.5 (112), 48.2 (211), 52.3 (103), 56.1 (020), and 56.7 (301) are attributed to crystalline orthorhombic cobalt monophosphide (CoP) phase (JCPDS-29-0497). The broad peak at $2\theta = 26.1^\circ$ corresponds to (002) plane of carbon nanotubes (CNT) [171].

Details of surface composition and oxidation state were collected with the aid of X-ray photoelectron spectroscopy (XPS), and results are shown in Figure 54. Survey spectrum (Figure 54A) verified the elemental composition of CoP/CNT, which comprises carbon (C), cobalt (Co), phosphorous (P), and oxygen (O). In the spectrum shown in Figure 54B, the peaks centered at 284.7 and 285.5 eV are assigned to graphitic carbon (C-C) and oxygenated carbon (C-O), respectively. The deconvoluted Co 2p XPS profile consists of several peaks (Figure 54C). The peaks at 779.1 eV (Co $2p_{3/2}$) and 793.9 eV (Co $2p_{1/2}$) are

ascribed to cobalt bonded to phosphorous in CoP, whereas spectral lines at 783.2 and 799.3 eV account for cobalt oxide or surface oxidized cobalt. In addition, there are other peaks

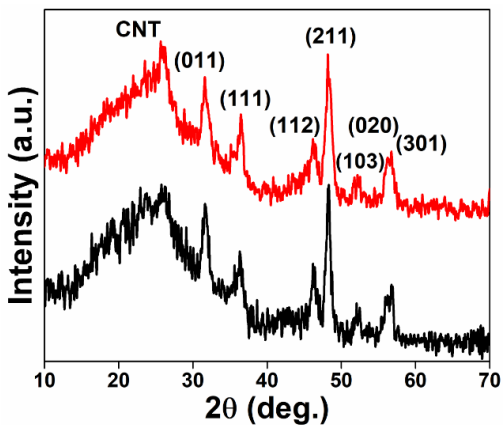


Figure 53: Powder XRD patterns for (A) hollow CoP/CNT (red) and (B) non-hollow CoP/CNT (black).

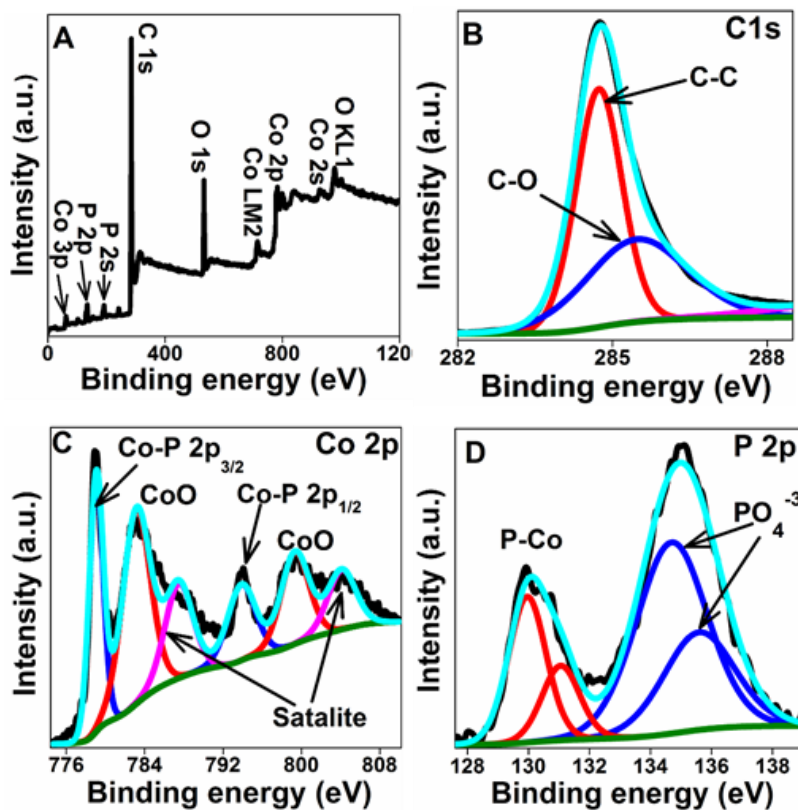


Figure 54: (A) XPS survey scan and high-resolution spectra of (B) C 1s, (C) Co 2p and (D) P 2p for CoP/CNT

(at 787.5 and 804.1 eV) known as “satellite” peaks, usually observed in CoP [61, 172]. Deconvolution of P 2p spectrum (Figure 54D) reveals two spectral signals at lower binding energy (peaks at 129.9 and 130.9 eV), corresponding to phosphorous anion bonded to cobalt in CoP, and at higher binding energy (peaks at 134.7 and 135.6 eV), accounting for phosphate species [61, 172]. The surface of CoP usually remains unstable and tend to oxidize under atmospheric environment, forming an oxide and phosphate moieties [70, 173]. When taken in combination, the Co 2p signal appeared at higher binding energy of 779.1 eV as compared to that of metallic cobalt (778.1 eV), whereas P 2p peak (129.9 eV) was recorded at lower binding energy as compared to that of elemental phosphorous (130.2 eV). This is interpreted in terms of slightly positive centers on cobalt and negative sites on phosphorous, due to electron transport between two entities in the crystal of CoP [125]. It has been anticipated, therefore, that HER performance originates from the CoP rather than oxidized compositions of Co or P [125].

Morphological features of CNT-supported CoP prepared with and without hexamethylenetetramine (HMT) were discerned by high-resolution transmission electron microscopy (HR-TEM), as shown in Figure 55. Figures A and B55 show the shape and morphology of CoP/CNT prepared in the absence of HMT. Particles were in the nanometer range (<20 nm) with semispherical shape and high degree of agglomeration. Moreover, the formation of elongated CoP, though few, were also observed as shown in Figure 55B. The images shown in Figures 55C and D highlight the morphological features of CoP/CNT obtained in the presence of HMT. Analyses confirmed the formation of the hollow nanospheres of CoP. In addition, such spheres were mostly interconnected and possessed

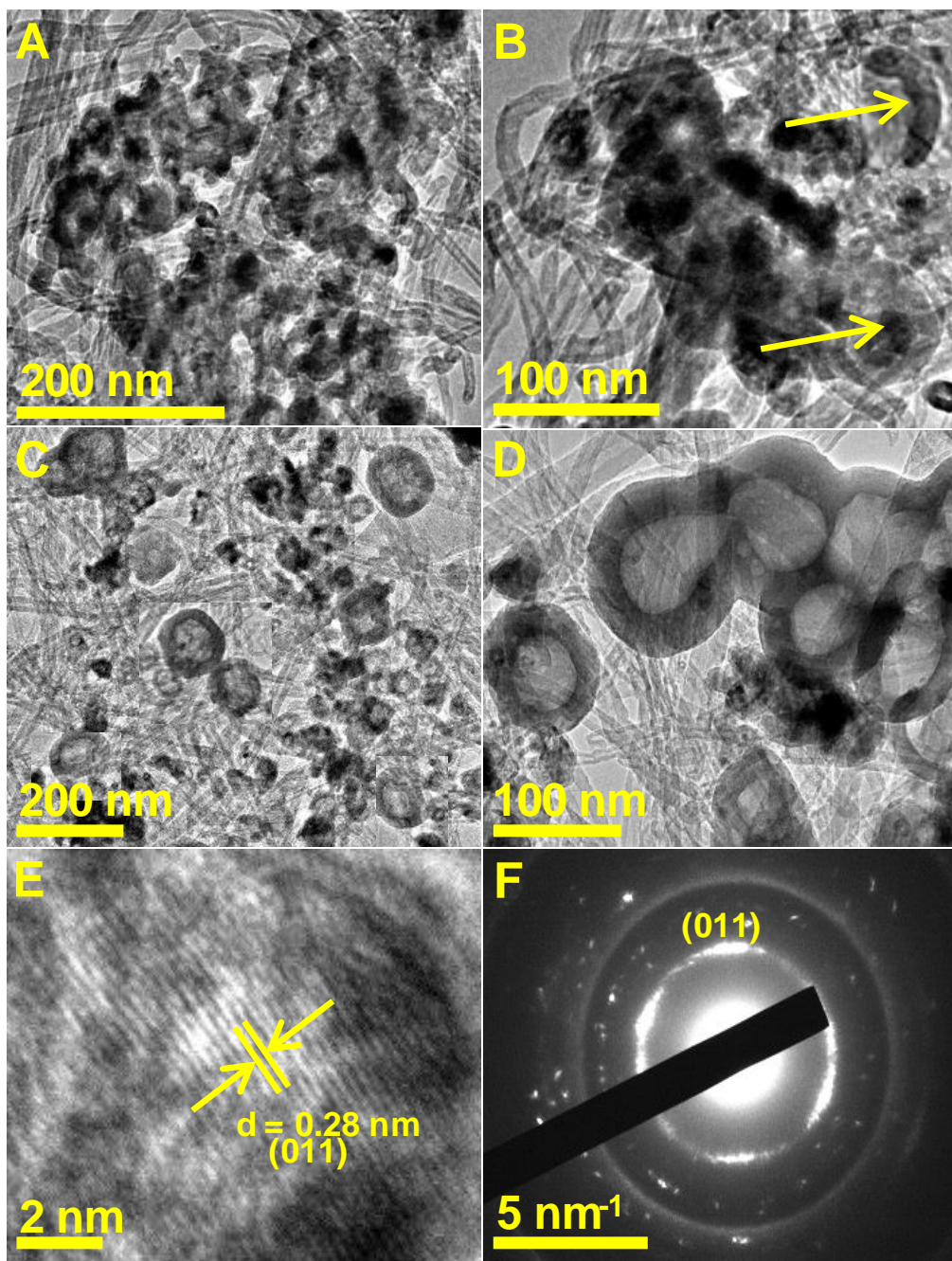


Figure 55: (A) low and (B) high-magnified TEM images of CoP/CNT. (C) low and (D) high magnified-TEM, (E) HR-TEM and (F) SAED images of hollow CoP/CNT.

well-developed outer shells, as shown in Figure 55 D. Size distribution was broad, ranging from 20 to 70 nm with a shell thickness of approximately 30 nm. Note, however, that hollow

structures co-existed with fine spherical nanoparticles of CoP. EDS elemental mapping of carbon, oxygen, phosphorus and cobalt in hollow CoP/CNT were taken (Figure 58), and Co was found to be well distributed on the hollow surface. The notion that hollow structures are CoP was strengthened by HR-TEM (Figure 55E), which also substantiates the high crystallinity seen in its diffraction pattern. The interplanar distance was estimated to be 0.28 nm, in good agreement with 0.28 nm based on XRD data for the (011) plane. The selected area electron diffraction (SAED) patterns, as shown Figure 55F, indicated a high degree of crystallinity and the polycrystalline nature of CoP/CNT.

Based on these findings, a plausible schematic showing the growth of the hollow nanospheres of CoP is delineated in Figure 56. Firstly, cobalt acetate and hexamethylenetetramine undergo ion-exchange reaction, forming cobalt-hexamethylenetetramine (Co-HMT) complex, in ethanol. Such a ligand exchange is quite facile and can occur even at room temperature (often indicated by a color change from dark to pale pink). Formation of the complex was investigated by ^1H and ^{13}C nuclear magnetic resonance (NMR) spectroscopic techniques. For comparison, two samples were prepared: (1) by dissolving HMT in ethanol followed by solvent evaporation, (2) by dissolving HMT and cobalt source in ethanol followed drying (Co-HMT complex). ^1H -NMR spectra are shown in Figure 57A. As could be seen, a single resonance peak at 4.53 ppm was observed in the case of HMT sample, which corresponds to equivalent protons of CH_2 motifs of highly symmetrical HMT. Analysis of Co-HMT complex gave two signals at 4.69 and 4.31 ppm. As compared to pure HMT sample, the peaks shift, more downfield and upfield, is caused by the interaction between HMT and cobalt metal center to form a Co-HMT complex. This notion was strengthened by carbon NMR analyses. In the case of ^{13}C NMR

of HMT sample (Figure 57B), one peak at 74.71 ppm was recorded evincing that all carbons were in a similar coordination field. On the other hand, analysis of the Co-HMT sample gave two prominent carbon signals suggesting the presence of carbon in the different coordination environment. The signals, at 78.5 and 68.35 ppm, were shifted toward downfield and upfield region, due to deshielding and shielding effect of cobalt center. This confirms a strong coordination bond between metal and HMT, leading to the formation of a stable Co-HMT complex onto the surface of the CNT.

As prepared Co-HMT/CNT was heated (350 °C) in the presence of sodium hypophosphite (NaPO_2H_2) to obtain CoP/CNT. This transformation proceeds via formation of cobalt oxide. As the process temperature was increased, Co-HMT complex decomposed and transformed into CoO. Formation of the oxide was confirmed by XRD of sample heated at 250 °C (Figure 59), for instance. Since, at 250 °C, decomposition of NaPO_2H_2 was not observed, CoP did not form. As the temperature was further raised (>300 °C), cobalt oxide was transformed into cobalt phosphide. Formation of cobalt phosphide endowed with a hollow structure could be interpreted by nanoscale Kirkendall effect. Owing to highly reactive traits, phosphine (PH_3) gas produced by decomposition of NaPO_2H_2 at 275 °C can readily react with surface of cobalt oxide, forming water (vapor) and protective thin surface layers of CoP and Co_2P as observed by XRD. This stage could presumably be explained by a core-shell model; CoP and Co_2P as shell and CoO as core. As the temperature is further increased to approximately 350 °C, Co^{2+} and/or P^{3-} ions tend to diffuse, outward and inward respectively, through the preformed phosphide layer as a result of the chemical potential and concentration gradient. It seems outward diffusion of

cobalt outperforms the inward diffusion of P^{3-} ions, resulting in the formation of hollow structure.

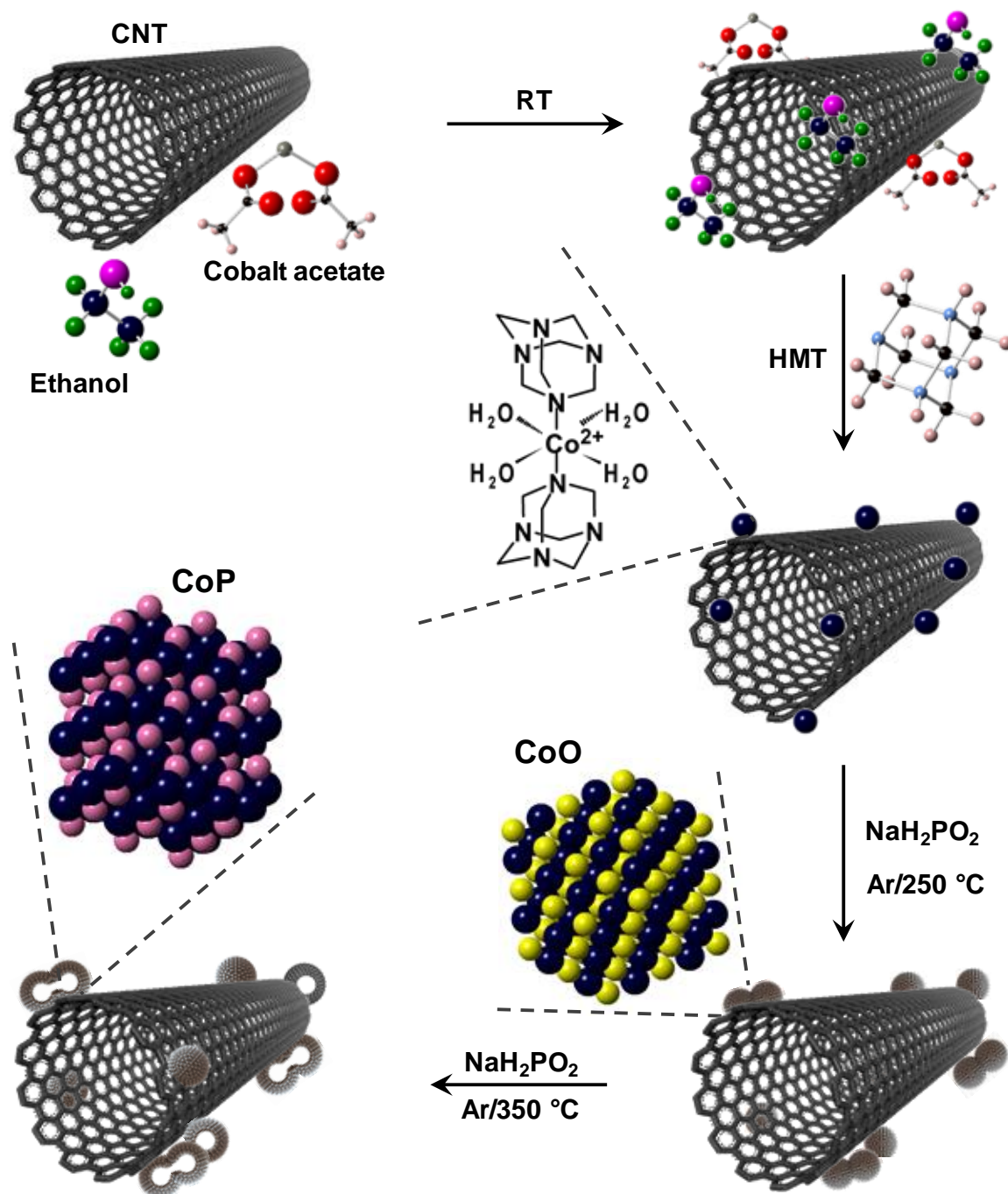


Figure 56: Preparation process of HMT-derived CoP/CNT electrocatalyst.

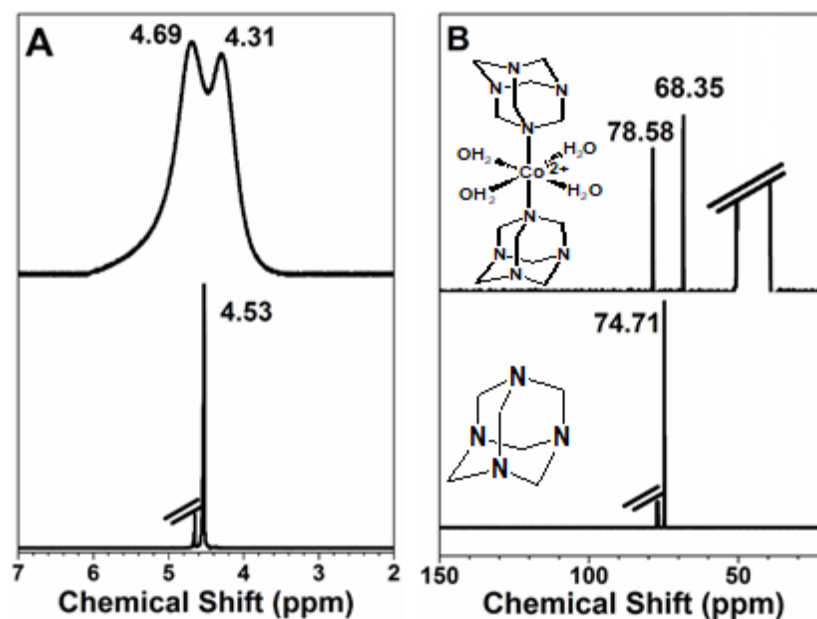


Figure 57: (A) ^1H NMR spectra of HMT (bottom) and its solution with $\text{Co}(\text{CH}_3\text{COO})_2 \cdot 4\text{H}_2\text{O}$ and ethanol (top) (B) ^{13}C NMR spectrum of HMT (bottom) and its solution with $\text{Co}(\text{CH}_3\text{COO})_2 \cdot 4\text{H}_2\text{O}$ and ethanol (top).

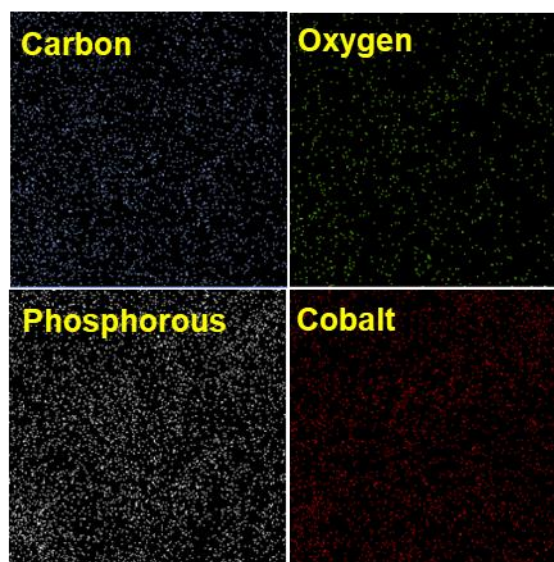


Figure 58: EDS elemental mapping of carbon, oxygen, phosphorous and cobalt present in CoP/CNT.

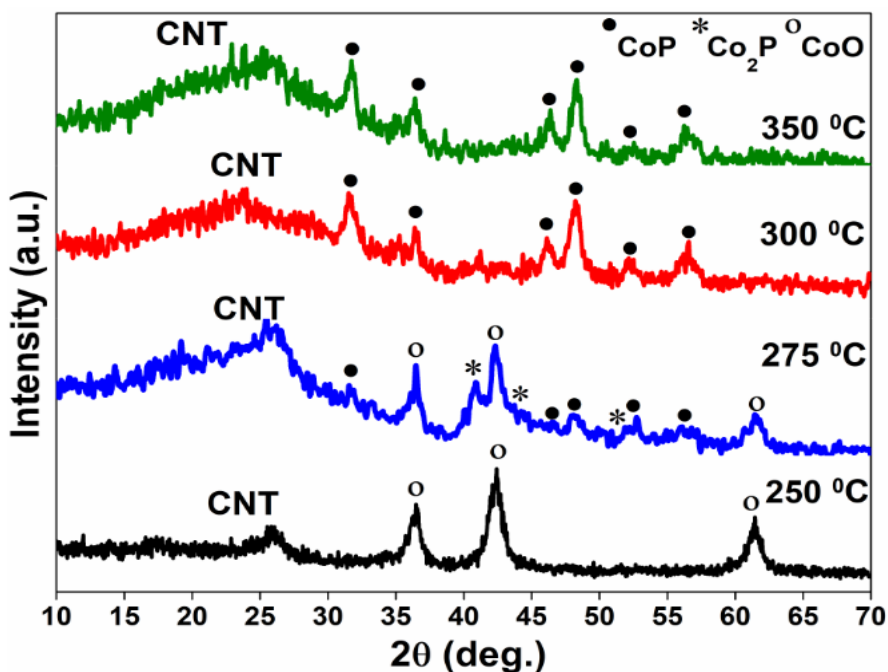


Figure 59: XRD of CoO/CNT obtained at 250 °C, CoO@Co_xP/CNT core-shell structure formed at 275 °C and CoP/CNT prepared at temperature of 300 and 350 °C

The propensity of electrocatalysts was investigated towards hydrogen evolution reaction (HER) in 0.5 M H₂SO₄ or 1.0 M KOH aqueous solution. The current density is estimated against the geometric area of the glassy carbon electrode. Findings of polarization studies (current density vs. potential) are shown in Figure 61. Since the phase evolution of cobalt phosphide is strongly dependent on processing temperature, temperature-dependent variation in performance is shown in Figure 61A. The activity increased with increase in temperature up to 350 °C followed by decrease at higher temperature such as 400 °C. The increasing activity trend could be ascribed to the structural evolution of CoP phase, the most active composition among cobalt phosphides. Significantly low performance of CoP/CNT prepared at 250 °C is due to molybdenum oxide, as indicated by XRD patterns, which is inactive for HER reaction (figure 60). Since

CoP/CNT prepared at 350 °C exhibited the best performance, samples for further study were prepared at this temperature.

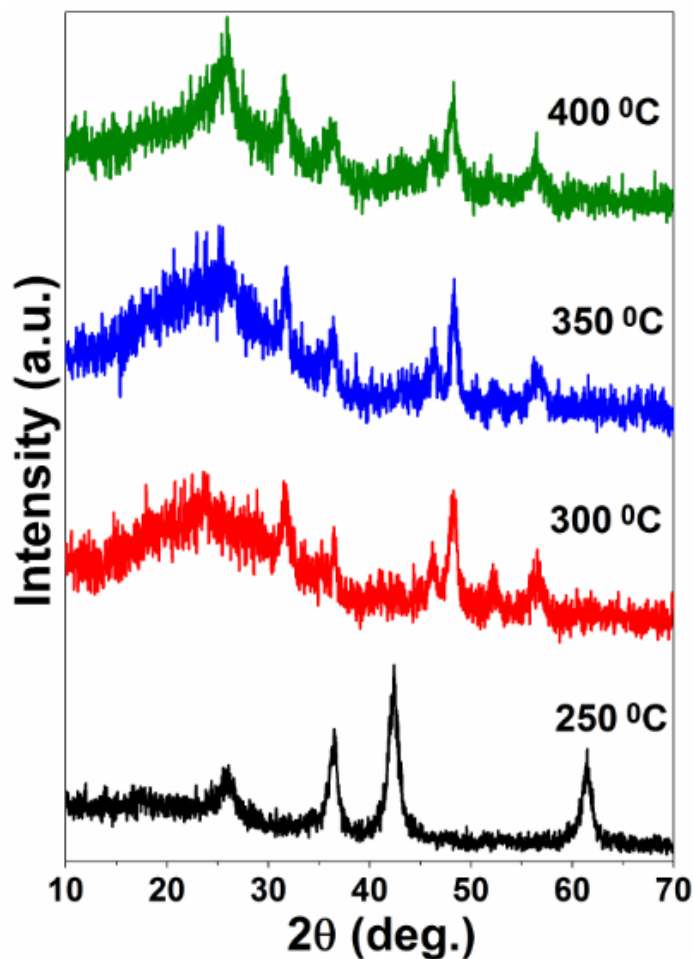


Figure 60: Powder XRD patterns of sample prepared at different temperatures (250,300, 350 and 400 °C).

Comparative polarization curves of Pt/C and hollow CoP/CNT recorded in acidic and basic media are also included in Figures 61C and D. In addition, to elucidate the significance of hollow morphology, performance of non-hollow CoP/CNT (prepared at 350 °C with 40 wt% Co) is also included. Tests were conducted under identical experimental conditions with the same mass of catalyst loading on GC electrode. In acidic

solution, the overpotentials to achieve a current density of 10 mAcm^{-2} were recorded to be 41, 70 and 118 mV for Pt/C, Hollow and non-hollow CoP/CNT, respectively. A similar activity trend was discerned in 1.0 M KOH solution, respective potentials needed to produce 10 mAcm^{-2} for Pt/C, the hollow CoP/CNT and CoP/CNT were 65, 123 and 175 mV. Apparently, Pt/C exhibited the best HER activity. While onset potential of Pt/C is very small and efficiently catalyzes the HER, its capability to produce large current densities is severely affected by generated H_2 bubbles (bubble effect) in acidic solution. Consequently, when compared for 15 mAcm^{-2} , both Pt/C and hollow CoP/CNT exhibited analogous overpotential 87 and 88 mV respectively. The bubble effect was not discerned with the electrode comprising Hollow CoP/CNT, even for current density $>120 \text{ mA}$. This signifies that the as derived hollow CoP/CNT is endowed with excellent mass transport property. Moreover, hollow CoP/CNT required substantially less (48 mV) overpotential than that of non-hollow counterpart to produce 10 mA current density.

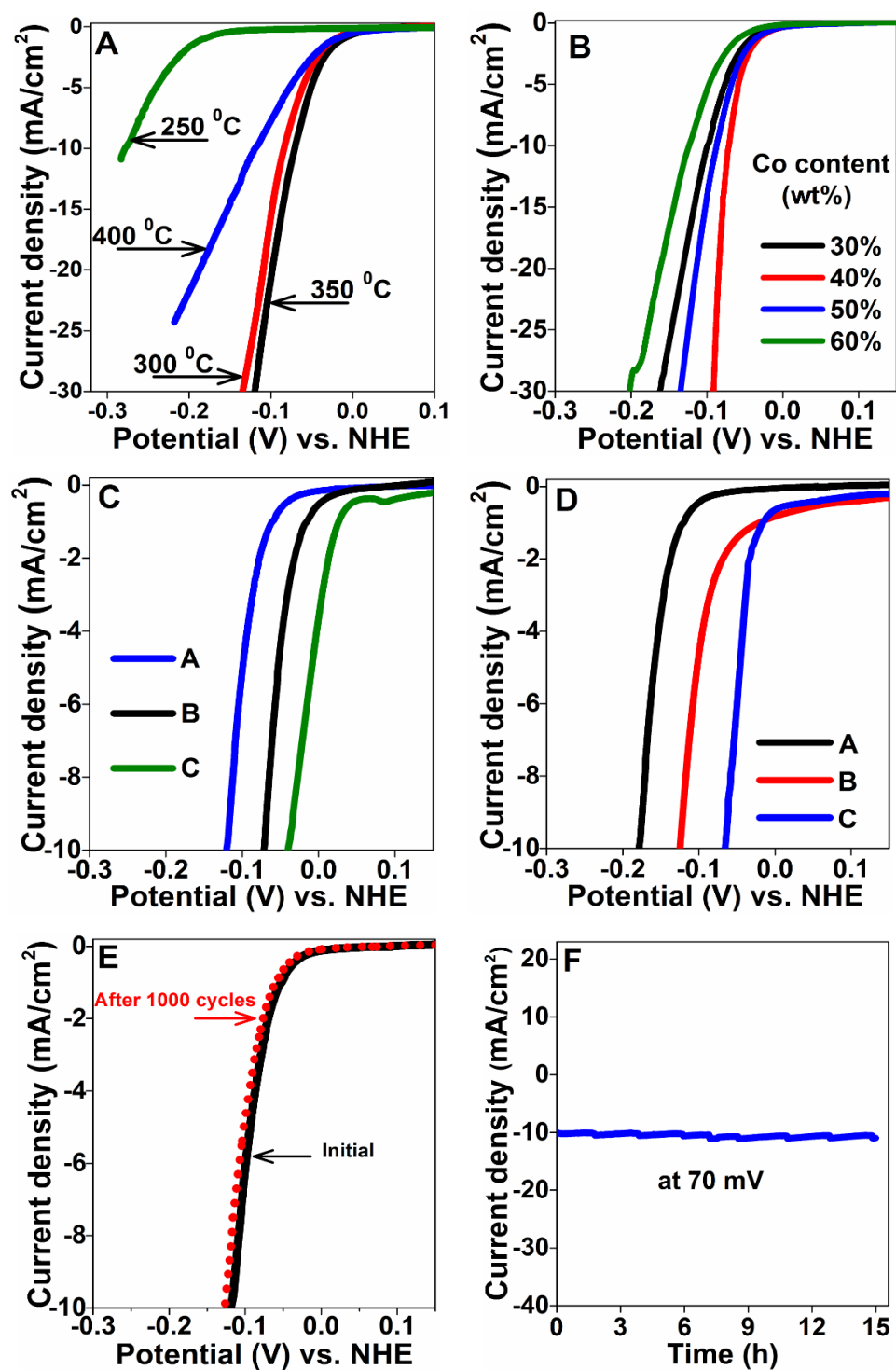


Figure 61: (A) Effect of phosphorization temperatures. (B) effect of Co content. (C) LSV curves of A-Pt/C, B- Hollow nanospheres CoP/CNT and C- nonhollow CoP/CNT in 0.5 M H₂SO₄ and (D) in 1M KOH (D). (E) stability before and after 1000 potentiodynamic sweeps, and (F) Time-dependent potentiostatic measurement.

Attempt was made to rationalize the augmented performance of the hollow CoP/CNT in terms of electrochemical active surface area (ECSA), specific surface area, electrochemical impedance and turnover frequency (TOF). BET surface areas for hollow CoP/and CoP/CNT were measured to be 65.3 and 56.3 m²g⁻¹ (Figure 63), while ECSA were estimated to be 12.5 and 17 mFcm⁻², respectively. EASA was quantified by measuring double layer capacitance (C_{dl}) of cyclic voltammograms (CVs). CVs were recorded at different scan rates ranging from 5 to 150 mVs⁻¹ (Figures 64A and C), and their corresponding plots of the current density at 0.245 V_{RHE} vs. scan rate are shown in Figures 64B and D. Usually, higher C_{dl} is demonstrated as higher electrochemical active area. When taken in combination, both specific surface area and ECSA are more favorable for hollow CoP/CNT. Since electrochemical hydrogen evolution reaction is a predominantly surface-dictated process, usually a higher surface area (specific and EASA) of electrocatalysts translate into better performance.

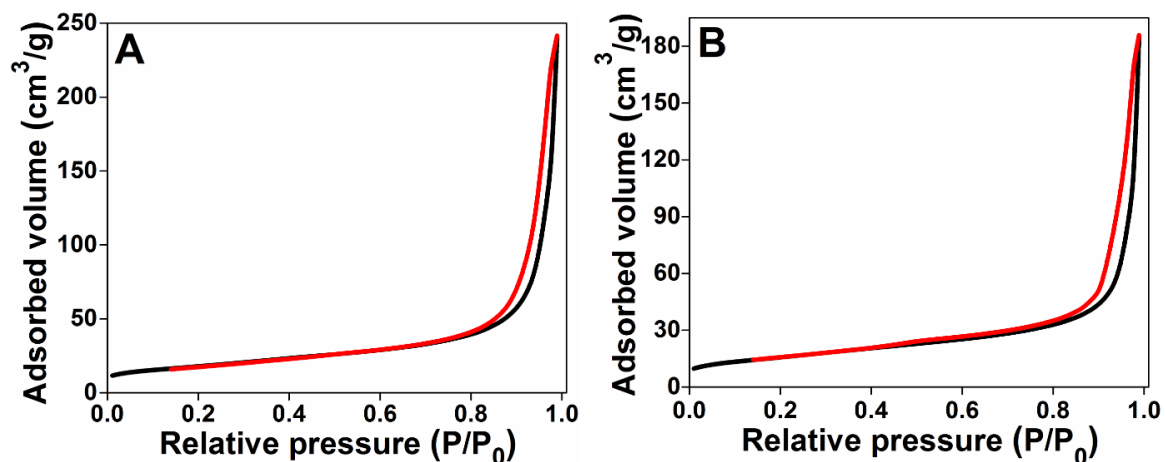


Figure 62: N₂ sorption isotherms of (A) hollow CoP/CNT and (B) nonhollow CoP/CNT.

Bulk conductivity as well as the charge transport property of as-prepared electrocatalysts was probed by electrochemical impedance spectroscopy (EIS). For HER,

EIS data are usually fitted by three types of electrical equivalent circuit models – one-time constant model [110], two-time constant parallel model [76] and two-time constant serial models [174]. In this study, the two-time constant parallel model consisting of solution resistance (R_s) in series with two parallel constant phase element-resistance was used. According to this equivalent circuit model, R_s denotes a collective resistance including the resistance of wiring (R_{wiring}), carbon support (R_{carbon}), CoP (R_{Cop}) and solution (R_{soln}) [175]. Furthermore, charge transfer resistance, resistance of porous surface, and capacitance are symbolized by R_{ct} , R_p and C_{dl} , respectively. Potential-dependent evolution in Nyquist plots, with corresponding Bode plots recorded at 130 mV, are shown in Figures 65C and A for hollow and non-hollow CoP/CNT. Plots were constructed as a function of overpotential ($\eta = 0, 10, 30, 50, 70, 90, 110$ and 130 mV). The semicircular dispersion of impedance is indicative of an interfacial phenomenon operative near the electrode surface. Shorter semicircular arcs indicate faster charge transfer at the interface and vice versa. Apparently, an inverse relationship between η and charge transfer resistance (R_{ct}) was observed – R_{ct} decreased significantly with increasing η . This implies faster charge transfer kinetics at high overpotential. When compared, charge transfer kinetics in hollow CoP/CNT was more dominant at all applied potential. For instance, an enlarged view of Nyquist plots recorded at $\eta = 0$ and 130 mV for both catalysts are compared in Figure 65E. Lower R_{ct} translates into better performance.

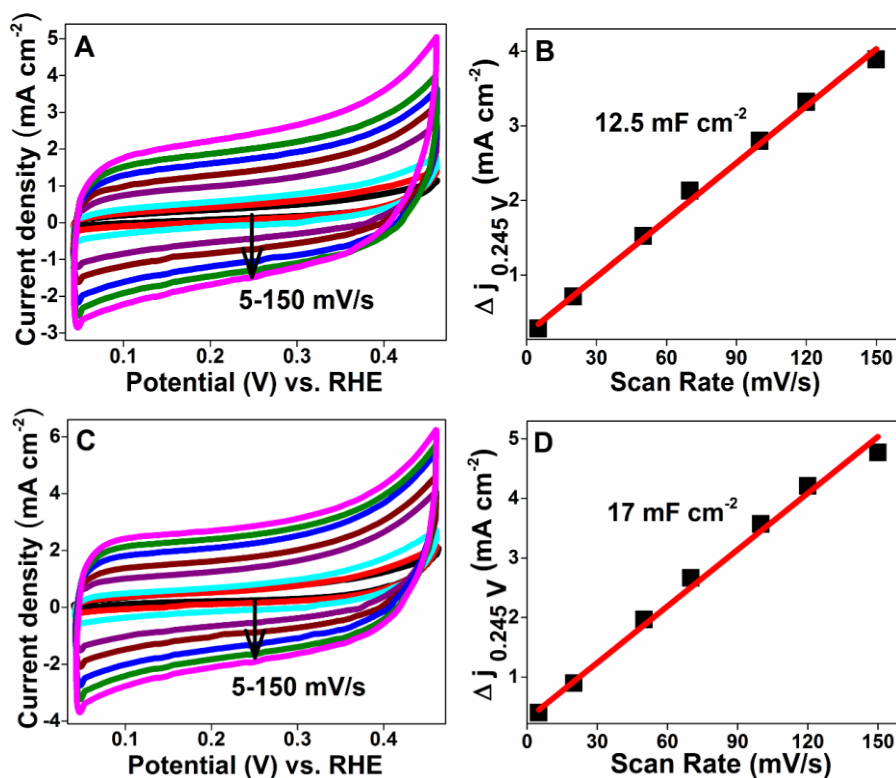
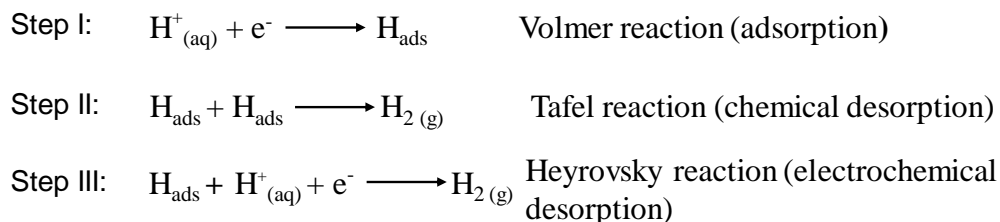


Figure 63: Cyclic voltammograms (CVs) of CoP/CNT recorded at different scan rates from 5 to 150 mVs⁻¹, and their corresponding plots of the current density at 0.245 VRHE vs. scan rate. (A) & (B) – Hollow CoP/CNT, (C) & (D) – nonhollow CoP/CNT. CVs were recorded in non-faradic region. The linear slopes are equivalent to twice of the electrochemical double layer capacitance (Cdl).

Under acidic conditions, HER reaction takes places following two different routes, which involve three probable reactions namely (1) Volmer reaction (adsorption), (2) Tafel reaction (chemical desorption) and (3) Heyrovsky reaction (electrochemical desorption), as shown below:



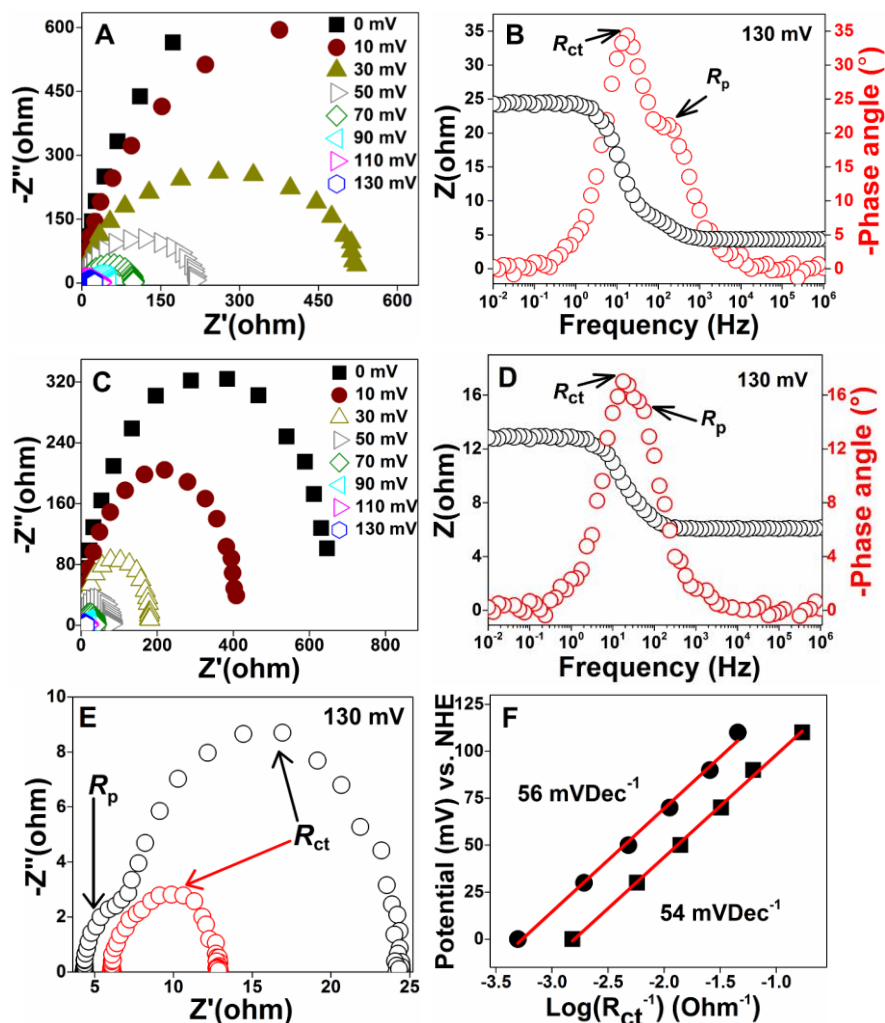


Figure 64: Nyquist and Bode plots for CoP/CNT: (A) & (B) – Solid CoP/CNT, (C) & (D) – Hollow CoP/CNT, (E) Enlarged view of Nyquist plots showing two semicircles, and (F) Their Tafel plots of 54 mVdec⁻¹ and 56 mVdec⁻¹, respectively.

By estimating Tafel slope, the reaction mechanism could be elucidated. Calculation of the semi-logarithmic values of the inverse of R_{ct} against η results in a linear relationship with a gradient, which is attributed to the Tafel slope. Moreover, Tafel slopes estimated by EIS represent entirely charge transport kinetics. Respective slopes of hollow and non-hollow CoP/CNT calculated from EIS statistics are shown in Figure 65F. The values are 54 and 56 mVdec⁻¹. Such values suggest that HER reaction proceeds via Volmer-Heyrovsky

mechanism, in which the electrochemical desorption of hydrogen ion and atom (Heyrovsky step) is more likely the rate-determining step.

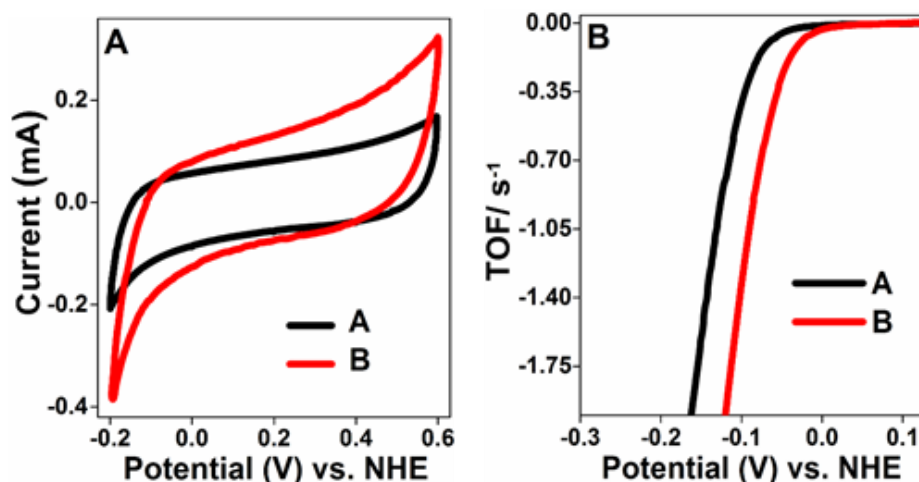


Figure 65: (A) The Cyclic voltammograms recorded between -0.2 and 0.6 V vs. NHE with scan rate of 20 mV/s for A- Non-Hollow CoP/CNT and B- Hollow CoP/CNT and (B) their corresponding TOF Vs overpotentials profiles.

In order to further evaluate the catalytic ability of as-synthesized electrocatalysts, turnover frequency (TOF) was calculated. TOF signifies the number of reactant molecules reacted per active site in unit time. Higher TOF values denote higher catalytic ability of electrocatalyst. Since electrocatalytic performance is dependent on catalysts mass deposited on the electrode (catalyst loading) and usually investigated with different mass loadings, estimation of TOF would allow the comparison of catalytic performance of as-synthesized electrocatalysts with those reported in the literature. Firstly, the number of active sites was quantified by electrochemical method [166]. Figure 66A compares the cyclic voltammograms of hollow and non-hollow electrocatalysts recorded between -0.2 V and +0.6 V_{NHE}. Measurements were performed in neutral phosphate buffer solution (PH=7) with a scan rate of 20 mVs⁻¹. The number of active sites for hollow and non-hollow

CoP/CNT was estimated to be 2×10^{-8} and 1.3×10^{-8} mole, respectively. The number of active sites was used to determine TOF using equation 3, and resulting TOF were plotted against potential, as shown in Figure 66B. At $\eta=70$ mV (the required potential to generate a geometric current density of 10 mA), electrode consisting of hollow CoP/CNT exhibits significantly higher TOF (0.59 s^{-1}) as compared to non-hollow CoP/CNT (0.12 s^{-1}).

Table 4: Comparison of electrocatalysts (CoP) for HER.

Catalysts	Electrolyte	Overpotential (mV)		Tafel slope (mVdec ¹)	Catalyst loading (mg cm ⁻²)
		η_{10}	η_{20}		
CoP@NPC [75]	0.5 M H ₂ SO ₄	123	156	69	0.255
CoP/Ti [176]	0.5 M H ₂ SO ₄	-	85	50	2
CoP/carbon cloth [125]	0.5 M H ₂ SO ₄	67	100	51	0.92
Co ₂ P nanorod/ Ti [177]	0.5 M H ₂ SO ₄	134	167	71	1
CoP/CNTs [171]	0.5 M H ₂ SO ₄	122	160	54	0.285
CoP/C [173]	0.1 M KOH	-	250	-	-
CoP nanosheet/C [178]	1 M KOH	111	139	70.9	0.71
Porous CoP/Ti [179]	1 M KOH	-	150	71	0.8
Porous CoP/Ti [179]	0.5 M H ₂ SO ₄	-	95	65	0.8
CoP/CNT [180]	0.1 M NaOH	215	-	56	0.285
CoP cluster [181]	0.5 M H ₂ SO ₄	85	-	50	-
CoP/NC [182]	1 M KOH	154	173	51	1
CoP/CNTs [183]	0.5 M H ₂ SO ₄	139	-	52	0.84
CoP/RGO [184]	0.5 M H ₂ SO ₄	~260	-	104.8	0.29
CoP nanowires [68]	0.5M H ₂ SO ₄	110	142	54	0.35
CoP nanosheets [68]	0.5 M H ₂ SO ₄	164	-	61	0.35
CoP nanotubes [185]	0.05 M H ₂ SO ₄	129	-	60	0.2
Hollow CoP/NG [169]	1 M KOH	83	100	57	2.5
CoP/NCNT [61]	0.5 M H ₂ SO ₄	79	99	58.5	~0.2
CoP/CNT^a	0.5 M H₂SO₄	70	96	54	1

a= This work.

6.4 Conclusion:

In summary, a single-step protocol was developed to fabricate hollow and interconnected nanospheres of CoP supported on CNTs. Structural evolution included the formation of cobalt-hexamethylenetetramine complex, decomposition and transformation in oxide form followed by phosphide phase consisting of hollow structure. While interconnected nexus rendered good electrical conductivity, hollow structure intensified the mass transport property and increased the density of active sites, in addition to higher specific and electrochemical active surface area. As a result, the electrocatalyst exhibited remarkable performance for hydrogen evolution reaction in both acidic and basic media. It required only 70 and 123 mV to drive 10 mA current density under acidic and basic media, respectively. For higher current density (e.g. 120 mA), the electrocatalytic performance of the hollow CoP/CNT was much better than that of benchmark electrocatalyst Pt/C, presumably due to superior mass transport attribute. Furthermore, the electrode exhibited excellent stability – at least for 15 h at 70 mV and 1000 potentiodynamic sweeps.

CHAPTER 7

CONCLUSION AND RECOMMENDATIONS

This study introduced new methods for synthesizing Mo₂C/C, Mo₂C/CNT, MoP/CNT and CoP/CNT composites to serve as inexpensive electrocatalysts for the hydrogen evolution reaction during water electrolysis.

A novel strategy to prepare β -Mo₂C supported on mesoporous carbon was demonstrated. In this approach, Metal-Organic Framework namely MIL-53(Al) rendered (1) confined environment for the nucleation and growth of fine Mo₂C nanoparticles, and (2) porous and rigid support for Mo₂C nanoparticles. Restricted space in the form of porous texture of MIL 53(Al) seemed to inhibit agglomeration and coalescence of in-situ-developed Mo₂C, presumably through homogeneous distribution of molybdenum on outer and inner frameworks of MOF, and thus guided the formation of fine and fairly dispersed Mo₂C nanocrystallites (5 – 10 nm in size) in carbon texture. As-synthesized Mo₂C/C heterostructure showed highly efficient electrocatalytic hydrogen evolution in alkaline aqueous media; better than that of Mo₂C/XC72 and close to commercial electrocatalyst Pt/C. Electrochemical impedance analysis of Mo₂C/C suggested the presence of two-time constants, and improved electrocatalytic performance of Mo₂C/C was attributed to faster charge kinetics. Furthermore, Tafel slope suggested a Volmer-Heyrovsky mechanism was operative in HER reaction. This impregnation method, demonstrated by the preparation of Mo₂C-based electrocatalyst, could open new avenues for the development of variety of nanostructured catalysts using the porous texture of metal-organic frameworks.

Another simple method is disclosed to prepare successfully fine-grained and uniformly dispersed Mo₂C onto the surface of CNT. The method involved complexation of molybdenum with oxalate group, which inhibited the agglomeration & coalescence and rendered restrained nucleation & growth of Mo₂C nanoparticles. A plausible mechanism involving complexation, nucleation with concomitant growth of Mo₂C on CNT surface was proposed. Oxalate-derived Mo₂C/CNT electrocatalyst exhibited highly efficient hydrogen evolution and excellent stability in acidic medium. Improved electrocatalytic performance was attributed to smaller surface-charge-resistance, and higher specific and electrochemical active surface area. Besides, estimated value of Tafel slope (51.34 mV dec⁻¹) confirmed that electrochemical desorption (Heyrovsky reaction) was the rate-determining step. Electrocatalyst performance showed strong dependency on synthesis temperature, ratio of Mo and CNT and catalyst loading. Study further revealed that charge transfer resistance increases and electrochemical active surface area decreases beyond optimum loading of Mo₂C on CNT. This affected the performance adversely. We believe that this strategy is likely to be employed for the fabrication of other relevant nanostructured electrocatalysts, as particle size and dispersion on solid support plays a critical role in determining the performance of catalysts.

The tendency to form molybdenum carbides and phosphides was strongly depended on the free energy of formation. The experimental and calculated data indicated that the energy formation of phosphides is relatively lower than that for carbides, suggesting the formation of MoP is thermodynamically more favorable [186]. To this end and taking the advantages of molybdenum oxalate complexation in presence of phosphoric acid (H₃PO₄) as a phosphorous precursor, an oxalate route was generalized to produce ultra-small and

uniformly distributed MoP nanoparticles onto the surface of CNT after carburization. The achieved Oxalate-derived MoP/CNT hybrids showed improved electrochemical hydrogen (H_2) evolution performance and robust durability in 0.5 M H_2SO_4 aqueous solution. The enhanced electrocatalytic performance may be attributed to smaller charge transfer resistance plus larger specific and electrochemical active surface area. In addition, a lower value of Tafel slope (51.6 mV/Dec) suggested the electrochemical desorption reaction was adopted as the rate-determining step for the Volmer–Heyrovsky electrocatalysis mechanism.

Due to better ionic and electrical diffusion, low mass density, porous texture, and most accessible active sites, hollow nanostructures are important for several technological applications including energy and environment sectors. a single-step protocol to obtain interconnected and hollow cobalt phosphide (CoP) supported on carbon nanotubes was devised. A plausible mechanism comprising cobalt complexation with hexamethylenetetramine, decomposition, oxide formation, and the concomitant growth of phosphide phase into a hollow morphology is proposed. The hollow CoP/CNT exhibits remarkable electrocatalytic performance for hydrogen evolution reaction (HER) – low onset (18 mV) and overpotential ($\eta_{10} = 70$ mV), small Tafel slope (53 mVdec⁻¹), and high turnover frequency (0.59 s⁻¹ at $\eta = 70$ mV). The electrode was stable at least for 15 h under continuous hydrogen production, and activity remained intact after 1000 potentiodynamic sweeps. Electrocatalytic performance of as-prepared CoP/CNT was compared with benchmark Pt/C and non-hollow CoP/CNT. The performance was rationalized in terms of specific surface area, electrochemical active surface area, electrical conductivity and interfacial charge transfer kinetics. The developed complexation strategy reported here

could pave the way to synthesize the other early transition metal phosphides for electrocatalytic water splitting and energy storage materials.

References

- [1] O. O. James, S. Maity, M. A. Mesubi, K. O. Ogunniran, T. O. Siyanbola, S. Sahu, and R. Chaubey, “Towards reforming technologies for production of hydrogen exclusively from renewable resources,” *Green Chem.*, vol. 13, p. 2272, 2011.
- [2] S. E. Hosseini, M. A. Wahid, , M. M. Jamil, , A. A. Azli, and M. F. Misbah, “A review on biomass-based hydrogen production for renewable energy supply,” *Int. J. Energy Res.*, vol. 39, pp. 1597–1615, 2015.
- [3] J. Turner, G. Sverdrup, M. K. Mann, P. C. Maness, B. Kroposki, M. Ghirardi, R. J. Evans, D. Blake, “Renewable hydrogen production,” *Int. J. Energy Res.*, vol. 32, pp. 379–407, 2008.
- [4] A. Borgschulte, “The Hydrogen Grand Challenge,” *Front. Energy Res.*, vol. 4, no. April, pp. 1–8, 2016.
- [5] O. Nematollahi, H. Hoghooghi, M. Rasti, and A. Sedaghat, “Energy demands and renewable energy resources in the Middle East,” *Renew. Sustain. Energy Rev.*, vol. 54, pp. 1172–1181, 2016.
- [6] Alvaro Umaña and Peter Eigen, “Brown to green: The G20 transition to a low-carbon economy,” no. 3rd report, 2017.
- [7] A. Ursua, L. M. Gandia, and P. Sanchis, “Hydrogen Production From Water Electrolysis: Current Status and Future Trends,” *Proc. IEEE*, vol. 100, no. 2, pp. 410–426, 2012.

- [8] Y. Ma, G. Guan, X. Hao, J. Cao, and A. Abudula, “Molybdenum carbide as alternative catalyst for hydrogen production – A review,” *Renew. Sustain. Energy Rev.*, vol. 75, no. November, pp. 1101–1129, 2017.
- [9] M. Zeng and Y. Li, “Recent advances in heterogeneous electrocatalysts for the hydrogen evolution reaction,” *J. Mater. Chem. A Mater. energy Sustain.*, vol. 3, pp. 14942–14962, 2015.
- [10] S. Wirth, F. Harnisch, M. Weinmann, and U. Schröder, “Comparative study of IVB – VIB transition metal compound electrocatalysts for the hydrogen evolution reaction,” *Applied Catal. B, Environ.*, vol. 126, pp. 225–230, 2012.
- [11] T. Shinagawa and K. Takanabe, “Towards Versatile and Sustainable Hydrogen Production through Electrocatalytic Water Splitting: Electrolyte Engineering,” *ChemSusChem*, vol. 10, pp. 1318–1336, 2017.
- [12] J. Wang, F. Xu, H. Jin, Y. Chen, and Y. Wang, “Non-Noble Metal-based Carbon Composites in Hydrogen Evolution Reaction: Fundamentals to Applications,” *Adv. Mater.*, vol. 29, p. 1605838, 2017.
- [13] C. C. L. McCrory, S. Jung, I. M. Ferrer, S. M. Chatman, J. C. Peters, and T. F. Jaramillo, “Benchmarking Hydrogen Evolving Reaction and Oxygen Evolving Reaction Electrocatalysts for Solar Water Splitting Devices,” *J. Am. Chem. Soc.*, vol. 137, no. 13, pp. 4347–4357, 2015.
- [14] S. Z. Qiao, Y. Zheng, Y. Jiao, M. Jaroniec, and S. Z. Qiao, “Advancing the Electrochemistry of the Hydrogen- Evolution Reaction through Combining

- Experiment and Theory,” *Angew. Chem. Int. Ed.*, vol. 54, pp. 52–65, 2015.
- [15] H. Ang, H. Wang, B. Li, Y. Zong, X. Wang, and Q. Yan, “3D Hierarchical Porous Mo₂C for Efficient Hydrogen Evolution,” *Small*, vol. 12, no. 21, pp. 2859–2865, 2016.
- [16] L. Ma, L. R. L. Ting, V. Molinari, C. Giordano, and B. S. Yeo, “Efficient hydrogen evolution reaction catalyzed by molybdenum carbide and molybdenum nitride nanocatalysts synthesized via the urea glass route,” *J. Mater. Chem. A*, vol. 3, no. 16, pp. 8361–8368, 2015.
- [17] L. Tian, X. Yan, and X. Chen, “Electrochemical Activity of Iron Phosphide Nanoparticles in Hydrogen Evolution Reaction,” *ACS Catal.*, vol. 6, pp. 5441–5448, 2016.
- [18] L. Liao, J. Zhu, X. Bian, L. Zhu, M. D. Scanlon, and H. H. Girault, “MoS₂ Formed on Mesoporous Graphene as a Highly Active Catalyst for Hydrogen Evolution,” *Adv. Funct. Mater.*, vol. 23, pp. 5326–5333, 2013.
- [19] J. Kibsgaard and T. F. Jaramillo, “Molybdenum phosphosulfide: An active, acid-stable, earth- Abundant catalyst for the hydrogen evolution reaction,” *Angew. Chemie - Int. Ed.*, vol. 53, no. 52, pp. 14433–14437, 2014.
- [20] S. T. Oyama, “Transition Metal Carbides, Nitrides, and Phosphides,” in *Handbook of heterogeneous catalysis*, 2008, pp. 342–356.
- [21] J. G. Chen, “Carbide and nitride overlayers on early transition metal surfaces: preparation, characterization, and reactivities,” *Chem. Rev.*, vol. 96, pp. 1477–1498,

1996.

- [22] W. Yao, P. Makowski, C. Giordano, and F. Goettmann, "Synthesis of Early-Transition-Metal Carbide and Nitride Nanoparticles through the Urea Route and Their Use as Alkylation Catalysts," *Chem. Eur. J.*, vol. 15, pp. 11999–12004, 2009.
- [23] E. Furimsky, "Metal carbides and nitrides as potential catalysts for hydroprocessing," *Appl. Catal. A Gen.*, vol. 240, pp. 1–28, 2003.
- [24] S. T. Oyama, T. Gott, H. Zhao, and Y. Lee, "Transition metal phosphide hydroprocessing catalysts : A review," *Catal. Today*, vol. 143, pp. 94–107, 2009.
- [25] U. Jansson and E. Lewin, "Sputter deposition of transition-metal carbide films — A critical review from a chemical perspective," *Thin Solid Films*, vol. 536, pp. 1–24, 2013.
- [26] R. B. Levy and M. Boudart, "Platinum-Like Behavior of Tungsten Carbide in Surface Catalysis," *Science*, vol. 181, no. 4099, pp. 547–549, 1973.
- [27] H. Vrubel and X. Hu, "Molybdenum boride and carbide catalyze hydrogen evolution in both acidic and basic solutions," *Angew. Chemie - Int. Ed.*, vol. 51, no. 51, pp. 12703–12706, 2012.
- [28] P. G. Li, M. Lei, Z. B. Sun, L. Z. Cao, Y. F. Guo, X. Guo, and W. H. Tang, "C₃N₄ as a precursor for the synthesis of NbC , TaC and WC nanoparticles," *J. Alloys Compd.*, vol. 430, pp. 237–240, 2007.
- [29] S. T. OYAMA, *The Chemistry of Transition Metal Carbides and Nitrides*, 1st ed. Glasgow: Blackie Academic & Professional, 1996.

- [30] C. G. Morales-Guio, L.-A. Stern, and X. Hu, “Nanostructured hydrotreating catalysts for electrochemical hydrogen evolution,” *Chem. Soc. Rev.*, vol. 43, no. 43, pp. 6555–6569, 2014.
- [31] F. Ma, H. B. Wu, B. Y. Xia, C. Xu, X. Wen, and D. Lou, “Hierarchical β -Mo₂C Nanotubes Organized by Ultrathin Nanosheets as a Highly Efficient Electrocatalyst for Hydrogen Production,” *Angew. Chemie Int. Ed.*, vol. 54, pp. 1–6, 2015.
- [32] C. Wan, N. A. Knight, and B. M. Leonard, “Crystal structure and morphology control of molybdenum carbide nanomaterials synthesized from an amine–metal oxide composite,” *Chem. Commun.*, vol. 49, pp. 10409–10411, 2013.
- [33] L. Liao, S. Wang, J. Xiao, X. Bian, Y. Zhang, M. D. Scanlon, X. Hu, Y. Tang, B. Liu, and H. H. Girault, “A nanoporous molybdenum carbide nanowire as an electrocatalyst for hydrogen evolution reaction,” *Energy Environ. Sci.*, vol. 7, no. 1, pp. 387–392, 2014.
- [34] W. F. Chen, C. H. Wang, K. Sasaki, N. Marinkovic, W. Xu, J. T. Muckerman, Y. Zhu, and R. R. Adzic, “Highly active and durable nanostructured molybdenum carbide electrocatalysts for hydrogen production,” *Energy Environ. Sci.*, vol. 6, no. 3, pp. 943–951, 2013.
- [35] D. H. Youn, S. Han, J. Y. Kim, J. Y. Kim, H. Park, S. H. Choi, and J. S. Lee, “Highly Active and Stable Hydrogen Evolution Electrocatalysts Based on Molybdenum Compounds on Carbon Nanotube À Graphene Hybrid Support,” *ACS Nano*, vol. 8, no. 5, pp. 5164–5173, 2014.

- [36] L. F. Pan, Y. H. Li, S. Yang, P. F. Liu, M. Q. Yu, and H. G. Yang, “Molybdenum carbide stabilized on graphene with high electrocatalytic activity for hydrogen evolution reaction.,” *Chem. Commun. (Camb).*, vol. 50, no. 86, pp. 13135–7, 2014.
- [37] H. Furukawa, K. E. Cordova, M. O’Keeffe, and O. M. Yaghi, “The Chemistry and Applications of Metal-Organic Frameworks,” *Science*, vol. 341, no. 6149, pp. 1230444–1230444, 2013.
- [38] M. Jahan, Q. Bao and K. P. Loh, “Electrocatalytically Active Graphene–Porphyrin MOF Composite for Oxygen Reduction Reaction,” *Angew. Chemie*, vol. 51, no. 47, p. SI, 2012.
- [39] M. Jaroniec, S. Z. Qiao, T. Y. Ma, S. Dai , “Metal-Organic Framework-Derived Hybrid Co₃O₄-Carbon Porous Nanowire Arrays as Reversible Oxygen Evolution Electrodes,” *Angew. Chemie*, vol. 51, no. 47, pp. 13925–13931, 2012.
- [40] X. Cao, B. Zheng, W. Shi, J. Yang, Z. Fan, Z. Luo, X. Rui, B. Chen, Q. Yan, and H. Zhang, “Reduced Graphene Oxide Wrapped MoO₃ Composites Prepared by Using Metal–Organic Frameworks as Precursor for All-Solid-State Flexible Supercapacitors,” *Adv. Mater.*, vol. 27, no. 32, pp. 4695–4701, 2015.
- [41] B. Chen, Y. Yang, F. Zapata, G. Lin, G. Qian, and E. B. Lobkovsky, “Luminescent open metal sites within a metal-organic framework for sensing small molecules,” *Adv. Mater.*, vol. 19, no. 13, pp. 1693–1696, 2007.
- [42] N. L. Torad, M. Hu, S. Ishihara, H. Sukegawa, A. A. Belik, M. Imura, K. Ariga, Y. Sakka, and Y. Yamauchi, “Direct synthesis of MOF-derived nanoporous carbon

- with magnetic Co nanoparticles toward efficient water treatment,” *Small*, vol. 10, no. 10, pp. 2096–2107, 2014.
- [43] P. Horcajada, T. Chalati, C. Serre, B. Gillet, C. Sebrie, T. Baati, J. F. Eubank, D. Heurtaux, P. Clayette, C. Kreuz, J. S. Chang, Y. K. Hwang, V. Marsaud, P. N. Bories, L. Cynober, S. Gil, G. Ferey, P. Couvreur, and R. Gref, “Porous metal-organic-framework nanoscale carriers as a potential platform for drug delivery and imaging,” *Nat. Mater.*, vol. 9, no. 2, pp. 172–178, 2010.
- [44] M. Abirami, S. M. Hwang, J. Yang, S. T. Senthilkumar, J. Kim, W. S. Go, B. Senthilkumar, H. K. Song, and Y. Kim, “A Metal-Organic Framework Derived Porous Cobalt Manganese Oxide Bifunctional Electrocatalyst for Hybrid Na-Air/Seawater Batteries,” *ACS Appl. Mater. Interfaces*, vol. 8, no. 48, pp. 32778–32787, 2016.
- [45] X. W. X. Xu, F. Nosheen, “Ni-Decorated Molybdenum Carbide Hollow Structure Derived from Carbon-Coated Metal-Organic Framework for Electrocatalytic Hydrogen Evolution Reaction,” *Chem. Mater.*, vol. 2, pp. 1–7, 2016.
- [46] T. Tian, L. Ai, and J. Jiang, “Metal–organic framework-derived nickel phosphides as efficient electrocatalysts toward sustainable hydrogen generation from water splitting,” *RSC Adv.*, vol. 5, no. 14, pp. 10290–10295, 2015.
- [47] S. Liu, Q. Huo, R. Chen, P. Chen, Y. Li, and Y. Han, “Synthesis and Characterization of an Iron Nitride Constructed by a Novel Template of Metal Organic Framework,” *J. Spectrosc.*, vol. 2015, 2015.

- [48] K. Pramoda, M. Kaur, U. Gupta, and C. N. R. Rao, “Nanocomposites of 2D-MoS₂ nanosheets with the metal–organic framework, ZIF-8,” *Dalt. Trans.*, pp. 1–10, 2016.
- [49] C. Sun, Q. Dong, J. Yang, Z. Dai, J. Lin, P. Chen, W. Huang, and X. Dong, “Metal–organic framework derived CoSe₂ nanoparticles anchored on carbon fibers as bifunctional electrocatalysts for efficient overall water splitting,” *Nano Res.*, vol. 9, no. 8, pp. 2234–2243, 2016.
- [50] J. S. Li, Y. J. Tang, C. H. Liu, S. L. Li, R. H. Li, L. Z. Dong, Z. H. Dai, J. C. Bao, and Y. Q. Lan, “Polyoxometalate-based metal-organic framework-derived hybrid electrocatalysts for highly efficient hydrogen evolution reaction,” *J. Mater. Chem. A Mater. energy Sustain.*, vol. 0, pp. 1–6, 2013.
- [51] J. S. Li, S. L. Li, Y. J. Tang, M. Han, Z. H. Dai, J. C. Bao, and Y. Q. Lan, “Nitrogen-doped Fe/Fe₃C@graphitic layer/carbon nanotube hybrids derived from MOFs: efficient bifunctional electrocatalysts for ORR and OER,” *Chem. Commun.*, vol. 51, no. 13, pp. 2710–2713, 2015.
- [52] H. B. Wu, B. Y. Xia, L. Yu, X. Y. Yu, and W. X. D. Lou, “Porous molybdenum carbide nano - octahedrons synthesized via confined carburization in metal - organic frameworks for efficient hydrogen production,” *Nat. Commun.*, vol. 6, pp. 1–12, 2015.
- [53] Q. L. Zhu, W. Xia, T. Akita, R. Zou, and Q. Xu, “Metal-Organic Framework-Derived Honeycomb-Like Open Porous Nanostructures as Precious-Metal-Free Catalysts for Highly Efficient Oxygen Electoreduction,” *Adv. Mater.*, pp. 6391–6398, 2016.

- [54] Y. Liu, X. Zhou, T. Ding, C. Wang, and Q. Yang, “3D architecture constructed via the confined growth of MoS₂ nanosheets in nanoporous carbon derived from metal-organic frameworks for efficient hydrogen production,” *Nanoscale*, vol. 7, no. 43, pp. 18004–18009, 2015.
- [55] Y. Xu, R. Wu, J. Zhang, Y. Shi, and B. Zhang, “Anion-exchange synthesis of nanoporous FeP nanosheets as electrocatalysts for hydrogen evolution reaction,” *Chem. Commun.*, vol. 49, pp. 6656–8, 2013.
- [56] Y. Pan, W. Hu, D. Liu, Y. Liu, and C. Liu, “Carbon nanotubes decorated with nickel phosphide nanoparticles as efficient nanohybrid electrocatalysts for the hydrogen evolution reaction,” *J. Mater. Chem. A*, vol. 3, no. 24, pp. 13087–13094, 2015.
- [57] J. Tian, Q. Liu, Y. Liang, Z. Xing, A. M. Asiri, and X. Sun, “FeP Nanoparticles Film Grown on Carbon Cloth : An Ultrahighly,” *ACS Appl. Mater. Interfaces*, vol. 6, pp. 20579–20584, 2014.
- [58] J. F. Callejas, C. G. Read, E. J. Popczun, J. M. McEnaney, and R. E. Schaak, “Nanostructured Co₂P Electrocatalyst for the Hydrogen Evolution Reaction and Direct Comparison with Morphologically Equivalent CoP,” *Chem. Mater.*, vol. 27, no. 10, pp. 3769–3774, 2015.
- [59] C. Lo and P. Kuo, “Synthesis and Magnetic Properties of Iron Phosphide Nanorods,” *J. Phys. Chem. C*, vol. 114, pp. 4808–4815, 2010.
- [60] E. J. Popczun, J. R. McKone, C. G. Read, A. J. Biech, A. M. Wiltout, N. S. Lewis, and R. E. Schaak, “Nanostructured nickel phosphide as an electrocatalyst for the

- hydrogen evolution reaction.,” *J. Am. Chem. Soc.*, vol. 135, no. 25, pp. 9267–70, Jul. 2013.
- [61] Y. Pan, Y. Lin, Y. Chen, Y. Liu, and C. Liu, “Cobalt phosphide-based electrocatalysts: synthesis and phase catalytic activity comparison for hydrogen evolution,” *J. Mater. Chem. A*, vol. 4, no. 13, pp. 4745–4754, 2016.
- [62] E. Muthuswamy, P. R. Kharel, G. Lawes, and S. L. Brock, “Control of Phase in Phosphide Nanoparticles Produced by Metal,” *ACS Nano*, vol. 3, no. 8, pp. 2383–2393, 2009.
- [63] L. A. Stern, L. Feng, F. Song, and X. Hu, “Ni₂P as a Janus catalyst for water splitting: the oxygen evolution activity of Ni₂P nanoparticles,” *Energy Environ. Sci.*, vol. 8, no. 8, pp. 2347–2351, 2015.
- [64] L. Feng, H. Vrubel, and X. Hu, “Easily-prepared dinickel phosphide (Ni₂P) nanoparticles as an efficient and robust electrocatalyst for hydrogen evolution,” *Phys. Chem. Chem. Phys.*, vol. 16, pp. 5917–5921, 2014.
- [65] P. Xiao, M. A. Sk, L. Thia, X. Ge, R. J. Lim, J. Y. Wang, K. H. Lim, P. Xiao, M. A. Sk, L. Thia, X. Ge, R. J. Lim, J. Y. Wang, K. H. Lim, and X. Wang, “Molybdenum phosphide as an efficient electrocatalyst for the hydrogen evolution reaction,” *Energy Environ. Sci.*, vol. 7, no. 1, pp. 2624–2629, 2014.
- [66] Z. Xing, Q. Liu, A. M. Asiri, and X. Sun, “Closely interconnected network of molybdenum phosphide nanoparticles: A highly efficient electrocatalyst for generating hydrogen from water,” *Adv. Mater.*, vol. 26, no. 32, pp. 5702–5707,

2014.

- [67] K. L. Stamm, J. C. Garno, G. y. Liu, and S. L. Brock, “A general methodology for the synthesis of transition metal pnictide nanoparticles from pnictate precursors and its application to iron-phosphorus phases,” *J. Am. Chem. Soc.*, vol. 125, no. 14, pp. 4038–4039, 2003.
- [68] P. Jiang, Q. Liu, C. Ge, W. Cui, Z. Pu, A. M. Asiri, and X. Sun, “CoP nanostructures with different morphologies: synthesis, characterization and a study of their electrocatalytic performance toward the hydrogen evolution reaction,” *J. Mater. Chem. A*, vol. 2, no. 35, p. 14634, 2014.
- [69] L. Dai, D. W. Chang, J. B. Baek, and W. Lu, “Carbon nanomaterials for advanced energy conversion and storage.,” *Small*, vol. 8, no. 8, pp. 1130–66, 2012.
- [70] W. Liu, E. Hu, H. Jiang, Y. Xiang, Z. Weng, M. Li, Q. Fan, X. Yu, E. I. Altman, and H. Wang, “A highly active and stable hydrogen evolution catalyst based on pyrite-structured cobalt phosphosulfide.,” *Nat. Commun.*, vol. 7, p. 10771, 2016.
- [71] X. Fan, H. Zhou, and X. Guo, “WC Nanocrystals Grown on Vertically Aligned Carbon Nanotubes: An Efficient and Stable Electrocatalyst for Hydrogen Evolution Reaction.,” *ACS Nano*, vol. 9, no. 5, pp. 5125–5134, 2015.
- [72] C. Rutherglen, D. Jain, and P. Burke, “Nanotube electronics for radiofrequency applications.,” *Nat. Nanotechnol.*, vol. 4, no. 12, pp. 811–9, 2009.
- [73] M. D. Volder, S. Tawfick, R. Baughman, and A. Hart, “Carbon nanotubes: present and future commercial applications,” *Science*, vol. 339, no. 2013, pp. 535–9, 2013.

- [74] Q. Liu, Z. Pu, A. M. Asiri, and X. Sun, “Nitrogen-doped carbon nanotube supported iron phosphide nanocomposites for highly active electrocatalysis of the hydrogen evolution reaction,” *Electrochim. Acta*, vol. 149, no. 3, pp. 324–329, 2014.
- [75] Y. P. Zhu, X. Xu, H. Su, Y. P. Liu, T. Chen, and Z. Y. Yuan, “Ultrafine Metal Phosphide Nanocrystals in Situ Decorated on Highly Porous Heteroatom-Doped Carbons for Active Electrocatalytic Hydrogen Evolution,” *ACS Appl. Mater. Interfaces*, vol. 7, no. 51, pp. 28369–28376, 2015.
- [76] Q. Lu, G. S. Hutchings, W. Yu, Y. Zhou, R. V. Forest, R. Tao, J. Rosen, B. T. Yonemoto, Z. Cao, H. Zheng, J. Q. Xiao, F. Jiao, and J. G. Chen, “Highly porous non-precious bimetallic electrocatalysts for efficient hydrogen evolution,” *Nat. Commun.*, vol. 6, p. 6567, 2015.
- [77] M. S. Faber and S. Jin, “Earth-abundant inorganic electrocatalysts and their nanostructures for energy conversion applications,” *Energy Environ. Sci.*, vol. 7, pp. 3519–3542, 2014.
- [78] P. Xiao, W. Chen, and X. Wang, “A Review of Phosphide-Based Materials for Electrocatalytic Hydrogen Evolution,” *Adv. Energy Mater.*, vol. 5, no. 24, pp. 1–13, 2015.
- [79] P. C. K. Vesborg, B. Seger, and I. Chorkendorff, “Recent development in hydrogen evolution reaction catalysts and their practical implementation,” *J. Phys. Chem. Lett.*, vol. 6, no. 6, pp. 951–957, 2015.
- [80] V. R. Stamenkovic, B. Fowler, B. S. Mun, G. Wang, P. N. Ross, C. A. Lucas, and

- N. M. Markovic, "Improved oxygen reduction activity on Pt₃Ni (111) via increased surface site availability," *Science*, vol. 315, no. 5811, pp. 493–497, 2007.
- [81] P. D. Tran, S. Y. Chiam, P. P. Boix, Y. Ren, S. S. Pramana, J. Fize, V. Artero, and J. Barber, "Novel cobalt/nickel–tungsten-sulfide catalysts for electrocatalytic hydrogen generation from water," *Energy Environ. Sci.*, vol. 6, no. 8, p. 2452, 2013.
- [82] C. He and J. Tao, "Synthesis of nanostructured clean surface molybdenum carbides on graphene sheets as efficient and stable hydrogen evolution reaction catalysts," *Chem. Commun.*, vol. 51, no. 39, pp. 8323–8325, 2015.
- [83] W. F. Chen, J. T. Muckerman, and E. Fujita, "Recent developments in transition metal carbides and nitrides as hydrogen evolution electrocatalysts," *Chem. Commun. (Camb.)*, vol. 49, no. 79, pp. 8896–909, Oct. 2013.
- [84] S. Meyer, A. V. Nikiforov, I. M. Petrushina, K. Köhler, E. Christensen, J. O. Jensen, and N. J. Bjerrum, "Transition metal carbides (WC, Mo₂C, TaC, NbC) as potential electrocatalysts for the hydrogen evolution reaction (HER) at medium temperatures," *Int. J. Hydrogen Energy*, vol. 40, no. 7, pp. 2905–2911, 2015.
- [85] J. F. Lin, O. Pitkänen, J. Mäklin, R. Puskas, A. Kukovecz, A. Dombovari, G. Toth, and K. Kordas, "Synthesis of tungsten carbide and tungsten disulfide on vertically aligned multi-walled carbon nanotube forests and their application as non-Pt electrocatalysts for the hydrogen evolution reaction," *J. Mater. Chem. A*, vol. 3, no. 28, pp. 14609–14616, 2015.
- [86] D. J. Li, U. N. Maiti, J. Lim, D. S. Choi, W. J. Lee, Y. Oh, G. Y. Lee, and S. O. Kim,

- “Molybdenum Sulfide/N-Doped CNT Forest Hybrid Catalysts for High-Performance Hydrogen Evolution Reaction,” *Nano Lett.*, vol. 14, p. 1228–1233, 2014.
- [87] D. Voiry, H. Yamaguchi, J. Li, R. Silva, and D. C. B. Alves, “Enhanced Catalytic Activity in Strained Chemically Exfoliated WS₂ Nanosheets for Hydrogen Evolution,” *Nat. Mater.*, vol. 9, pp. 1–23, 2013.
- [88] S. M. Tan and M. Pumera, “Bottom-up Electrosynthesis of Highly Active Tungsten Sulfide (WS_{3-x}) Films for Hydrogen Evolution,” *ACS Appl. Mater. Interfaces*, vol. 8, no. 6, pp. 3948–3957, 2016.
- [89] D. Kong, H. Wang, Z. Lu, and Y. Cui, “CoSe₂ Nanoparticles Grown on Carbon Fiber Paper: An efficient and Stable Electrocatalyst for Hydrogen Evolution Reaction,” *J. Am. Chem. Soc.*, vol. 136, no. 13, pp. 1–7, 2014.
- [90] A. I. Carim, F. H. Saadi, M. P. Soriaga, and N. S. Lewis, “Electrocatalysis of the hydrogen-evolution reaction by electrodeposited amorphous cobalt selenide films,” *J. Mater. Chem. A*, vol. 2, no. 34, pp. 13835–13839, 2014.
- [91] X. Wang, Y. V. Kolen’Ko, X. Q. Bao, K. Kovnir, and L. Liu, “One-Step Synthesis of Self-Supported Nickel Phosphide Nanosheet Array Cathodes for Efficient Electrocatalytic Hydrogen Generation,” *Angew. Chemie - Int. Ed.*, vol. 54, no. 28, pp. 8188–8192, 2015.
- [92] J. S. Moon, J. H. Jang, E. G. Kim, Y. H. Chung, S. J. Yoo, and Y. K. Lee, “The nature of active sites of Ni₂P electrocatalyst for hydrogen evolution reaction,” *J. Catal.*,

vol. 326, no. 0, pp. 92–99, 2015.

- [93] A. B. Laursen, K. R. Patraju, M. J. Whitaker, M. Retuerto, T. Sarkar, N. Yao, K. V. Ramanujachary, M. Greenblatt, and G. C. Dismukes, “Nanocrystalline Ni_5P_4 : a hydrogen evolution electrocatalyst of exceptional efficiency in both alkaline and acidic media,” *Energy Environ. Sci.*, vol. 8, no. 3, pp. 1027–1034, 2015.
- [94] P. Jiang, Q. Liu, Y. Liang, J. Tian, A. M. Asiri, and X. Sun, “A Cost-Effective 3D Hydrogen Evolution Cathode with High Catalytic Activity: FeP Nanowire Array as the Active Phase,” *Angew. Chemie - Int. Ed.*, vol. 53, no. 47, pp. 12855–12859, 2014.
- [95] R. W. Liu, S. Gu, H. F. Du, and C. M. Li, “Controlled synthesis of FeP nanorod arrays as highly efficient hydrogen evolution cathode,” *J. Mater. Chem. A*, vol. 2, no. 41, pp. 17263–17267, 2014.
- [96] Y. Shi and B. Zhang, “Recent advances in transition metal phosphide nanomaterials: synthesis and applications in hydrogen evolution reaction,” *Chem. Soc. Rev.*, vol. 45, no. 6, pp. 1529–1541, 2016.
- [97] B. Cao, G. M. Veith, J. C. Neufeind, R. R. Adzic, P. G. Khalifah, and P. G. Kha, “Mixed close packed cobalt molybdenum nitrides as non-noble metal electrocatalysts for the hydrogen evolution reaction Mixed close packed cobalt molybdenum nitrides as non-noble metal electrocatalysts for the hydrogen evolution reaction,” *J. Am. Chem. Soc.*, vol. 135, p. 19186–19192, 2013.
- [98] W. F. Chen, K. Sasaki, C. Ma, A. I. Frenkel, N. Marinkovic, J. T. Muckerman, Y.

- Zhu, and R. R. Adzic, “Hydrogen-Evolution Catalysts Based on Non-Noble Metal Nickel-Molybdenum Nitride Nanosheets,” *Angew. Chemie*, vol. 124, no. 25, pp. 6235–6239, Jun. 2012.
- [99] R. Wu, J. Zhang, Y. Shi, D. Liu and B. Zhang “Metallic WO₂–Carbon Mesoporous Nanowires as Highly Efficient Electrocatalysts for Hydrogen Evolution Reaction,” *J. Am. Chem. Soc.*, vol. 137, p. 6983–6986., 2015.
- [100] R. Xu, R. Wu, Y. Shi, J. Zhang, and B. Zhang, “Ni₃Se₂ nanoforest/Ni foam as a hydrophilic, metallic, and self-supported bifunctional electrocatalyst for both H₂ and O₂ generations,” *Nano Energy*, vol. 24, pp. 103–110, 2016.
- [101] F. Armstrong, N. Belsey, J. Cracknell, G. Goldet, A. Parkin, E. Reisner, K. Vincent, and A. F. Wait, “Dynamic electrochemical investigations of hydrogen oxidation and production by enzymes and implications for future technology.,” *Chem. Soc. Rev.*, vol. 38, no. 1, pp. 36–51, 2009.
- [102] B. W. Jensen, K. Fraser, C. Ong, M. Forsyth, and D. R. MacFarlane, “Conducting polymer composite materials for hydrogen generation,” *Adv. Mater.*, vol. 22, no. 15, pp. 1727–1730, 2010.
- [103] T. F. Jaramillo, K. P. Jorgensen, J. Bonde, J. H. Nielsen, S. Horch, and I. Chorkendorff, “Identification of Active Edge Sites for Electrochemical H₂ Evolution from MoS₂ Nanocatalysts,” *Science*, vol. 317, no. 5834, pp. 100–102, 2007.
- [104] A. L. Goff, V. Artero, B. Jusselme, P. D. Tran, N. Guillet, R. Métayé, A. Fihri, S. Palacin, and M. Fontecave, “From Hydrogenases to Noble Metal–Free Catalytic

- Nanomaterials for H₂ Production and Uptake,” *Science*, vol. 326, no. 5958, pp. 1384–1387, 2009.
- [105] P. D. Tran, A. Le Goff, J. Heidkamp, B. Jousselme, N. Guillet, S. Palacin, H. Dau, M. Fontecave, and V. Artero, “Noncovalent modification of carbon nanotubes with pyrene-functionalized nickel complexes: Carbon monoxide tolerant catalysts for hydrogen evolution and uptake,” *Angew. Chemie - Int. Ed.*, vol. 50, no. 6, pp. 1371–1374, 2011.
- [106] N. S. Alhajri, D. H. Anjum, and K. Takanabe, “Molybdenum carbide–carbon nanocomposites synthesized from a reactive template for electrochemical hydrogen evolution,” *J. Mater. Chem. A*, vol. 2, no. 27, pp. 10548–10556, 2014.
- [107] K. Zhang, C. Li, Y. Zhao, X. Yu, and Y. Chen, “Porous one-dimensional Mo₂C-amorphous carbon composites: high-efficient and durable electrocatalysts for hydrogen generation,” *Phys. Chem. Chem. Phys.*, vol. 17, no. 25, pp. 16609–14, 2015.
- [108] Z. Shi, Y. Wang, H. Lin, H. Zhang, M. Shen, S. Xie, Y. Zhang, Q. Gao, and Y. Tang, “Porous nanoMoC@graphite shell derived from a MOFs-directed strategy: an efficient electrocatalyst for the hydrogen evolution reaction,” *J. Mater. Chem. A*, vol. 4, pp. 6006–6013, 2016.
- [109] L. Fan, P. F. Liu, X. Yan, L. Gu, Z. Z. Yang, H. G. Yang, S. Qiu, and X. Yao, “Atomically isolated nickel species anchored on graphitized carbon for efficient hydrogen evolution electrocatalysis,” *Nat. Commun.*, vol. 7, p. 10667, 2016.

- [110] N. A. Khan, J. W. Jun, J. H. Jeong, and S. H. Jhung, "Remarkable adsorptive performance of a metal–organic framework, vanadium-benzenedicarboxylate (MIL-47), for benzothiophene," *Chem. Commun.*, vol. 47, no. 4, pp. 1306–1308, 2011.
- [111] J. Liu, F. Zhang, X. Zou, G. Yu, N. Zhao, S. Fan, and G. Zhu, "Environmentally friendly synthesis of highly hydrophobic and stable MIL-53 MOF nanomaterials.," *Chem. Commun. (Camb)*, vol. 49, no. 67, pp. 7430–2, 2013.
- [112] C. Wan, Y. N. Regmi, and B. M. Leonard, "Multiple phases of molybdenum carbide as electrocatalysts for the hydrogen evolution reaction," *Angew. Chemie - Int. Ed.*, vol. 53, no. 25, pp. 6407–6410, 2014.
- [113] H. Vrubel, D. Merki, and X. Hu, "Hydrogen evolution catalyzed by MoS₃ and MoS₂ particles," *Energy Environ. Sci.*, vol. 5, no. 3, pp. 6136–6144, 2012.
- [114] J. Kibsgaard, Z. Chen, B. N. Reinecke, and T. F. Jaramillo, "Engineering the surface structure of MoS₂ to preferentially expose active edge sites for electrocatalysis," *Nat. Mater.*, vol. 11, no. 11, pp. 963–969, 2012.
- [115] F. Safizadeh, E. Ghali, and G. Houlachi, "Electrocatalysis developments for hydrogen evolution reaction in alkaline solutions - A Review," *Int. J. Hydrogen Energy*, vol. 40, no. 1, pp. 256–274, 2015.
- [116] X. Yan, L. Tian, M. He, and X. Chen, "Three-dimensional crystalline/amorphous Co/Co₃O₄ core/shell nanosheets as efficient electrocatalysts for hydrogen evolution reaction," *Nano Lett.*, vol. 15, no. 9, pp. 6015–6021, 2015.
- [117] A. R. J. Kucernak and V. N. Naranammalpuram Sundaram, "Nickel phosphide: the

- effect of phosphorus content on hydrogen evolution activity and corrosion resistance in acidic medium,” *J. Mater. Chem. A*, vol. 2, no. 41, pp. 17435–17445, 2014.
- [118] W. Cui, C. Ge, Z. Xing, A. M. Asiri, and X. Sun, “Ni_xS_y-MoS₂ hybrid microspheres: One-pot hydrothermal synthesis and their application as a novel hydrogen evolution reaction electrocatalyst with enhanced activity,” *Electrochim. Acta*, vol. 137, pp. 504–510, 2014.
- [119] B. Sljukic, M. Vujkovic, L. Amaral, D. M. F. Santos, R. P. Rocha, C. A. C. Sequeira, and J. L. Figueiredo, “Carbon-supported Mo₂C electrocatalysts for hydrogen evolution reaction,” *J. Mater. Chem. A*, vol. 3, no. 30, pp. 15505–15512, 2015.
- [120] K. Zhang, Y. Zhao, D. Fu, and Y. Chen, “Molybdenum carbide nanocrystal embedded N-doped carbon nanotubes as electrocatalysts for hydrogen generation,” *J. Mater. Chem. A*, vol. 3, pp. 5783–5788, 2015.
- [121] L. F. Pan, Y. H. Li, S. Yang, P. F. Liu, M. Q. Yu, and H. G. Yang, “Molybdenum carbide stabilized on graphene with high electrocatalytic activity for hydrogen evolution reaction,” *Chem. Commun. (Camb.)*, vol. 50, no. 86, pp. 13135–7, Oct. 2014.
- [122] X. J. Yang, X. J. Feng, H. Q. Tan, H. Y. Zang, X. L. Wang, Y. H. Wang, E. B. Wang, and Y. G. Li, “N-Doped graphene-coated molybdenum carbide nanoparticles as highly efficient electrocatalysts for the hydrogen evolution reaction,” *J. Mater. Chem. A*, vol. 4, no. 10, pp. 3947–3954, 2016.
- [123] M. Fan, H. Chen, Y. Wu, L. Feng, Y. Liu, and G. Li, “Growth of molybdenum

- carbide micro-islands on carbon cloth toward binder-free cathodes for efficient hydrogen evolution reaction,” *J. Mater. Chem. A Mater. energy Sustain.*, vol. 3, pp. 16320–16326, 2015.
- [124] H. Vrubel and X. Hu, “Molybdenum boride and carbide catalyze hydrogen evolution in both acidic and basic solutions,” *Angew. Chem. Int. Ed. Engl.*, vol. 51, no. 51, pp. 12703–6, Dec. 2012.
- [125] J. Tian, Q. Liu, A. M. Asiri, and X. Sun, “Self-Supported Nanoporous Cobalt Phosphide Nanowire Arrays: An Efficient 3D Hydrogen-Evolving Cathode over the Wide Range of pH 0–14,” *J. Am. Chem. Soc.*, vol. 136, no. 50, p. 7587–7590, 2014.
- [126] M. Cabán-Acevedo, M. L. Stone, J. R. Schmidt, J. G. Thomas, Q. Ding, H.-C. Chang, M.-L. Tsai, J.-H. He, and S. Jin, “Efficient hydrogen evolution catalysis using ternary pyrite-type cobalt phosphosulphide,” *Nat. Mater.*, vol. 14, no. 12, pp. 1245–51, 2015.
- [127] Z. Luo, R. Miao, T. D. Huan, I. M. Mosa, A. S. Poyraz, W. Zhong, J. E. Cloud, D. A. Kriz, S. Thanneeru, J. He, Y. Zhang, R. Ramprasad, and S. L. Suib, “Mesoporous MoO_{3-x} Material as an Efficient Electrocatalyst for Hydrogen Evolution Reactions,” *Adv. Energy Mater.*, vol. 6, no. 16, pp. 1–11, 2016.
- [128] F. Harnisch, G. Sievers, and U. Schröder, “Tungsten carbide as electrocatalyst for the hydrogen evolution reaction in pH neutral electrolyte solutions,” *Appl. Catal. B Environ.*, vol. 89, pp. 455–458, 2009.
- [129] Y. Huang, Q. Gong, X. Song, K. Feng, K. Nie, F. Zhao, Y. Wang, M. Zeng, J.

- Zhong, Y. Li, “Mo₂C Nanoparticles Dispersed on Hierarchical Carbon Microflowers for Efficient Electrocatalytic Hydrogen Evolution,” *ACS Nano*, vol. 10, pp. 11337–11343, 2016.
- [130] Z. Pu, M. Wang, Z. Kou, A. I. Saana, and S. Mu, “Mo₂C quantum dots embedded chitosan-derived nitrogen-doped carbon for efficient hydrogen evolution in a broad pH range,” *Chem. Commun.*, vol. 52, no. 86, pp. 12753–12756, 2016.
- [131] M. Qamar, A. Adam, B. Merzougui, A. Helal, O. Abdulhamid, and M. N. Siddiqui, “Metal–organic framework-guided growth of Mo₂C embedded in mesoporous carbon as a high-performance and stable electrocatalyst for the hydrogen evolution reaction,” *J. Mater. Chem. A*, vol. 4, no. 41, pp. 16225–16232, 2016.
- [132] C. Limberg and B. Schiemenz, “Intermediates and products of the reaction of MoCl₅ with ethanol: crystal structures of [MoOCl₃ (EtOH)] and H [MoOCl₄]. 2EtOH,” *J. Chem. Soc. Dalt. Trans.*, vol. 3, pp. 2–6, 1930.
- [133] J. T. C. He, “Universal Strategy to Fabricate a Two-Dimensional Layered Mesoporous Mo₂C Electrocatalyst Hybridized on Graphene Sheets with High Activity and Durability for Hydrogen Generation,” *ACS Appl. Mater. Interfaces*, vol. 8, pp. 18107–18118, 2016.
- [134] H. Lin, Z. Shi, S. He, X. Yu, S. Wang, Q. Gao, and Y. Tang, “Heteronanowires of MoC–Mo₂C as efficient electrocatalysts for hydrogen evolution reaction,” *Chem. Sci.*, vol. 7, pp. 3399–3405, 2016.
- [135] F. X. Ma, H. Bin Wu, B. Y. Xia, C. Y. Xu, and X. W. Lou, “Hierarchical b-Mo₂C

- Nanotubes Organized by Ultrathin Nanosheets as a Highly Efficient Electrocatalyst for Hydrogen Production,” *Angew. Chemie - Int. Ed.*, vol. 54, no. 51, pp. 15395–15399, 2015.
- [136] B. Cao, G. M. Veith, J. C. Neuefeind, R. R. Adzic, and P. G. Khalifah, “Mixed close-packed cobalt molybdenum nitrides as non-noble metal electrocatalysts for the hydrogen evolution reaction,” *J. Am. Chem. Soc.*, vol. 135, no. 51, pp. 19186–19192, 2013.
- [137] P. R. Jothi, Y. Zhang, J. P. Scheifers, H. Park, and B. P. T. Fokwa, “Molybdenum diboride nanoparticles as a highly efficient electrocatalyst for the hydrogen evolution reaction,” *Sustain. Energy Fuels*, vol. 1, pp. 1928–1934, 2017.
- [138] Z. X. Cai, X. H. Song, Y. R. Wang, and X. Chen, “Electrodeposition-Assisted Synthesis of Ni₂P Nanosheets on 3D Graphene/Ni Foam Electrode and Its Performance for Electrocatalytic Hydrogen Production,” *ChemElectroChem*, vol. 2, no. 11, pp. 1665–1671, 2015.
- [139] M. Ledendecker, S. Krickalderön, C. Papp, H. P. Steinrück, M. Antonietti, and M. Shalom, “The Synthesis of Nanostructured Ni₅P₄ Films and their Use as a Non-Noble Bifunctional Electrocatalyst for Full Water Splitting,” *Angew. Chemie - Int. Ed.*, vol. 54, no. 42, pp. 12361–12365, 2015.
- [140] L. Berben and J. C. Peters, “Hydrogen evolution by cobalt tetraimine catalysts adsorbed on electrode surfaces,” *Chem. Commun. (Camb)*, vol. 46, no. 3, pp. 398–400, 2010.

- [141] C. Deng, F. Ding, X. Li, Y. Guo, W. Ni, H. Yan, K. Sun, and Y. M. Yan, “Templated-preparation of a three-dimensional molybdenum phosphide sponge as a high performance electrode for hydrogen evolution,” *J. Mater. Chem. A*, vol. 4, no. 1, pp. 59–66, 2016.
- [142] W. Cui, Q. Liu, Z. Xing, A. M. Asiri, K. A. Alamry, and X. Sun, “MoP nanosheets supported on biomass-derived carbon flake: One-step facile preparation and application as a novel high-active electrocatalyst toward hydrogen evolution reaction,” *Appl. Catal. B Environ.*, vol. 164, pp. 144–150, 2014.
- [143] C. Deng, J. Xie, Y. Xue, M. He, X. Wei, and Y. M. Yan, “Synthesis of MoP decorated carbon cloth as a binder-free electrode for hydrogen evolution,” *RSC Adv.*, vol. 6, no. 73, pp. 68568–68573, 2016.
- [144] H. Vrubel, T. Moehl, M. Grätzel, and X. Hu, “Revealing and accelerating slow electron transport in amorphous molybdenum sulphide particles for hydrogen evolution reaction,” *Chem. Commun.*, vol. 49, no. 79, p. 8985, 2013.
- [145] S. S. J. Aravind, K. Ramanujachary, A. Mugweru, and T. D. Vaden, “Molybdenum phosphide-graphite nanomaterials for efficient electrocatalytic hydrogen production,” *Appl. Catal. A Gen.*, vol. 490, pp. 101–107, 2015.
- [146] M. A. R. Anjum and J. S. Lee, “Sulfur and Nitrogen Dual-Doped Molybdenum Phosphide Nanocrystallites as an Active and Stable Hydrogen Evolution Reaction Electrocatalyst in Acidic and Alkaline Media,” *ACS Catal.*, vol. 7, no. 4, pp. 3030–3038, 2017.

- [147] X. D. Wang, Y. F. Xu, H. S. Rao, W. J. Xu, H. Y. Chen, W. X. Zhang, D. B. Kuang, and C. Y. Su, “Novel porous molybdenum tungsten phosphide hybrid nanosheets on carbon cloth for efficient hydrogen evolution,” *Energy Environ. Sci.*, vol. 9, no. 4, pp. 1468–1475, 2016.
- [148] J. M. McEnaney, J. C. Crompton, J. F. Callejas, E. J. Popczun, A. J. Biacchi, N. S. Lewis, and R. E. Schaak, “Amorphous Molybdenum Phosphide Nanoparticles for Electrocatalytic Hydrogen Evolution,” *Chem. Mater.*, vol. 26, no. 16, pp. 4826–4831, Aug. 2014.
- [149] T. Wang, K. Du, W. Liu, Z. Zhu, Y. Shao, and M. Li, “Enhanced electrocatalytic activity of MoP microparticles for hydrogen evolution by grinding and electrochemical activation,” *J. Mater. Chem. A*, vol. 3, no. 8, pp. 4368–4373, 2015.
- [150] Z. Chen, C. Lv, Z. Chen, L. Jin, J. Wang, and Z. Huang, “Molybdenum Phosphide Flakes Catalyze Hydrogen Generation in Acidic and Basic Solutions,” *Am. J. Anal. Chem.*, vol. 5, no. December, pp. 1200–1213, 2014.
- [151] X. Chen, D. Wang, Z. Wang, P. Zhou, Z. Wu, and F. Jiang, “Molybdenum phosphide: a new highly efficient catalyst for the electrochemical hydrogen evolution reaction,” *Chem. Commun.*, vol. 50, no. 79, pp. 11683–11685, 2014.
- [152] Z. Yao, Y. Su, C. Lu, C. Yang, Z. Xu, J. Zhu, X. Zhuang, and F. Zhang, “Template-directed approach to two-dimensional molybdenum phosphide-carbon nanocomposites with high catalytic activities in the hydrogen evolution reaction,” *New J. Chem.*, vol. 40, no. 7, pp. 6015–6021, 2016.

- [153] H. Yan, Y. Jiao, A. Wu, C. Tian, X. Zhang, L. Wang, Z. Ren, and H. Fu, "Cluster-like molybdenum phosphide anchored on reduced graphene oxide for efficient hydrogen evolution over a broad pH range," *Chem. Commun.*, vol. 52, no. 61, pp. 9530–9533, 2016.
- [154] Y. Zhao, S. Wang, C. Li, X. Yu, and C. Zhu, "Nanostructured molybdenum phosphide/N,P dual-doped carbon nanotube composite as electrocatalysts for hydrogen evolution," *RSC Adv.*, vol. 6, pp. 7370–7377, 2016.
- [155] Z. Pu, S. Wei, Z. Chen, and S. Mu, "Flexible molybdenum phosphide nanosheet array electrodes for hydrogen evolution reaction in a wide pH range," *Appl. Catal. B Environ.*, vol. 196, pp. 193–198, 2016.
- [156] Z. Pu, I. S. Amiin, X. Liu, M. Wang, and S. Mu, "Ultrastable nitrogen-doped carbon encapsulating molybdenum phosphide nanoparticles as highly efficient electrocatalyst for hydrogen generation," *Nanoscale*, vol. 8, no. 39, pp. 17256–17261, 2016.
- [157] Z. Pu, I. Saana Amiin, M. Wang, Y. Yang, and S. Mu, "Semimetallic MoP₂: an active and stable hydrogen evolution electrocatalyst over the whole pH range," *Nanoscale*, vol. 8, no. 16, pp. 8500–8504, 2016.
- [158] K. Ojha, M. Sharma, H. Koley, and A. K. Ganguli, "Reduced graphene oxide and MoP composite as highly efficient and durable electrocatalyst for hydrogen evolution in both acidic and alkaline media," *Catal. Sci. Technol.*, vol. 7, no. 3, pp. 668–676, 2017.

- [159] J. Yang, F. Zhang, X. Wang, D. He, G. Wu, Q. Yang, X. Hong, Y. Wu, and Y. Li, “Porous Molybdenum Phosphide Nano-Octahedrons Derived from Confined Phosphorization in UIO-66 for Efficient Hydrogen Evolution,” *Angew. Chemie - Int. Ed.*, vol. 55, no. 41, pp. 12854–12858, 2016.
- [160] X. Zou and Y. Zhang, “Noble metal-free hydrogen evolution catalysts for water splitting,” *Chem. Soc. Rev.*, vol. 44, no. 15, pp. 5148–5180, 2015.
- [161] D. Kong, H. Wang, Z. Lu, and Y. Cui, “CoSe₂ nanoparticles grown on carbon fiber paper: An efficient and stable electrocatalyst for hydrogen evolution reaction,” *J. Am. Chem. Soc.*, vol. 136, no. 13, pp. 4897–4900, 2014.
- [162] Y. Chen, G. Yu, W. Chen, Y. Liu, G. D. Li, P. Zhu, Q. Tao, Q. Li, J. Liu, X. Shen, H. Li, X. Huang, D. Wang, T. Asefa, and X. Zou, “Highly Active, Nonprecious Electrocatalyst Comprising Borophene Subunits for the Hydrogen Evolution Reaction,” *J. Am. Chem. Soc.*, vol. 139, no. 36, pp. 12370–12373, 2017.
- [163] K. E. Marusak, A. C. Johnston-Peck, W. C. Wu, B. D. Anderson, and J. B. Tracy, “Size and Composition Control of CoNi Nanoparticles and Their Conversion into Phosphides,” *Chem. Mater.*, vol. 29, no. 7, pp. 2739–2747, 2017.
- [164] T. D. Nguyen, C. T. Dinh, and T. O. Do, “Tailoring the assembly, interfaces, and porosity of nanostructures toward enhanced catalytic activity,” *Chem. Commun.*, vol. 51, no. 4, pp. 624–635, 2015.
- [165] K. Qu, Y. Zheng, X. Zhang, K. Davey, S. Dai, and S. Z. Qiao, “Promotion of Electrocatalytic Hydrogen Evolution Reaction on Nitrogen-Doped Carbon

- Nanosheets with Secondary Heteroatoms,” *ACS Nano*, vol. 11, no. 7, pp. 7293–7300, 2017.
- [166] Z. Jin, P. Li, X. Huang, G. Zeng, Y. Jin, B. Zheng, and D. Xiao, “Three-dimensional amorphous tungsten-doped nickel phosphide microsphere as an efficient electrocatalyst for hydrogen evolution,” *J. Mater. Chem. A*, vol. 2, no. 43, pp. 18593–18599, 2014.
- [167] Y. Tan, H. Wang, P. Liu, C. Cheng, F. Zhu, A. Hirata, and M. Chen, “3D Nanoporous Metal Phosphides toward High-Efficiency Electrochemical Hydrogen Production,” *Adv. Mater.*, vol. 28, no. 15, pp. 2951–2955, 2016.
- [168] X. W. Lou, L. A. Archer, and Z. Yang, “Hollow micro-/nanostructures: Synthesis and applications,” *Adv. Mater.*, vol. 20, no. 21, pp. 3987–4019, 2008.
- [169] X. Yu, S. Zhang, C. Li, C. Zhu, Y. Chen, P. Gao, L. Qi, and X. Zhang, “Hollow CoP nanoparticle/N-doped graphene hybrids as highly active and stable bifunctional catalysts for full water splitting,” *Nanoscale*, vol. 8, pp. 10902–10907, 2016.
- [170] M. Liu and J. Li, “Cobalt Phosphide Hollow Polyhedron as Efficient Bifunctional Electrocatalysts for the Evolution Reaction of Hydrogen and Oxygen,” *ACS Appl. Mater. Interfaces*, vol. 8, no. 3, pp. 2158–2165, 2016.
- [171] Q. Liu, J. Tian, W. Cui, P. Jiang, N. Cheng, A. M. Asiri, and X. Sun, “Carbon nanotubes decorated with CoP nanocrystals: A highly active non-noble-metal nanohybrid electrocatalyst for hydrogen evolution,” *Angew. Chemie - Int. Ed.*, vol. 53, no. 26, pp. 6710–6714, 2014.

- [172] T. Liu, K. Wang, G. Du, A. M. Asiri, and X. Sun, “Self-supported CoP nanosheet arrays: a non-precious metal catalyst for efficient hydrogen generation from alkaline NaBH₄ solution,” *J. Mater. Chem. A*, vol. 4, no. 34, pp. 13053–13057, 2016.
- [173] J. Ryu, N. Jung, J. H. Jang, H. J. Kim, and S. J. Yoo, “In Situ Transformation of Hydrogen-Evolving CoP Nanoparticles: Toward Efficient Oxygen Evolution Catalysts Bearing Dispersed Morphologies with Co-oxo/hydroxo Molecular Units,” *ACS Catal.*, vol. 5, no. 7, pp. 4066–4074, 2015.
- [174] C. Wan, Y. N. Regmi, and B. M. Leonard, “Multiple Phases of Molybdenum Carbide as Electrocatalysts for the Hydrogen Evolution Reaction,” *Angew. Chemie*, vol. 126, no. 25, pp. 6525–6528, Jun. 2014.
- [175] Y. Zhang, Q. Gao, Z. Lin, T. Zhang, J. Xu, Y. Tan, W. Tian, and L. Jiang, “Constructing Free Standing Metal Organic Framework MIL-53 Membrane Based on Anodized Aluminum Oxide Precursor,” *Sci. Rep.*, vol. 4:4947, pp. 1–6, 2014.
- [176] E. J. Popczun, C. G. Read, C. W. Roske, N. S. Lewis, and R. E. Schaak, “Highly active electrocatalysis of the hydrogen evolution reaction by cobalt phosphide nanoparticles,” *Angew. Chem. Int. Ed. Engl.*, vol. 53, no. 21, pp. 5427–30, May 2014.
- [177] Z. Huang, Z. Chen, Z. Chen, C. Lv, M. G. Humphrey, and C. Zhang, “Cobalt phosphide nanorods as an efficient electrocatalyst for the hydrogen evolution reaction,” *Nano Energy*, vol. 9, pp. 373–382, 2014.
- [178] J. Chang, L. Liang, C. Li, M. Wang, J. Ge, C. Liu, and W. Xing, “Ultrathin cobalt

- phosphide nanosheets as efficient bifunctional catalysts for a water electrolysis cell and the origin for cell performance degradation,” *Green Chem.*, vol. 18, no. 8, pp. 2287–2295, 2016.
- [179] S. Gu, H. Du, A. M. Asiri, X. Sun, and C. M. Li, “Three-dimensional interconnected network of nanoporous CoP nanowires as an efficient hydrogen evolution cathode,” *Phys. Chem. Chem. Phys.*, vol. 16, no. 32, pp. 16909–13, 2014.
- [180] C. C. Hou, S. Cao, W. F. Fu, and Y. Chen, “Ultrafine CoP Nanoparticles Supported on Carbon Nanotubes as Highly Active Electrocatalyst for Both Oxygen and Hydrogen Evolution in Basic Media,” *ACS Appl. Mater. Interfaces*, vol. 7, no. 51, pp. 28412–28419, 2015.
- [181] F. H. Saadi, A. I. Carim, E. Verlage, J. C. Hemminger, N. S. Lewis, and M. P. Soriaga, “CoP as an acid-stable active electrocatalyst for the hydrogen-evolution reaction: Electrochemical synthesis, interfacial characterization and performance evaluation,” *J. Phys. Chem. C*, vol. 118, no. 50, pp. 29294–29300, 2014.
- [182] B. You, N. Jiang, M. Sheng, S. Gul, J. Yano, and Y. Sun, “High-Performance Overall Water Splitting Electrocatalysts Derived from Cobalt-Based Metal-Organic Frameworks,” *Chem. Mater.*, vol. 27, no. 22, pp. 7636–7642, 2015.
- [183] C. Wu, Y. Yang, D. Dong, Y. Zhang, and J. Li, “In Situ Coupling of CoP Polyhedrons and Carbon Nanotubes as Highly Efficient Hydrogen Evolution Reaction Electrocatalyst,” *Small*, vol. 13, no. 15, pp. 1–9, 2017.
- [184] L. Ma, X. Shen, H. Zhou, G. Zhu, Z. Ji, and K. Chen, “CoP nanoparticles deposited

on reduced graphene oxide sheets as an active electrocatalyst for the hydrogen evolution reaction,” *J. Mater. Chem. A*, vol. 3, no. 10, pp. 5337–5343, 2015.

[185] H. Du, Q. Liu, N. Cheng, A. M. Asiri, X. Sun, and C. M. Li, “Template-assisted synthesis of CoP nanotubes to efficiently catalyze hydrogen-evolving reaction,” *J. Mater. Chem. A*, vol. 2, no. 36, pp. 14812–14816, 2014.

[186] Z. W. Yao, “Corrigendum to “Exploration on synthesis of activated carbon supported molybdenum carbide, nitride and phosphide via carbothermal reduction route,” *J. Alloys Compd.*, vol. 484, p. 974, 2009.

Appendix A

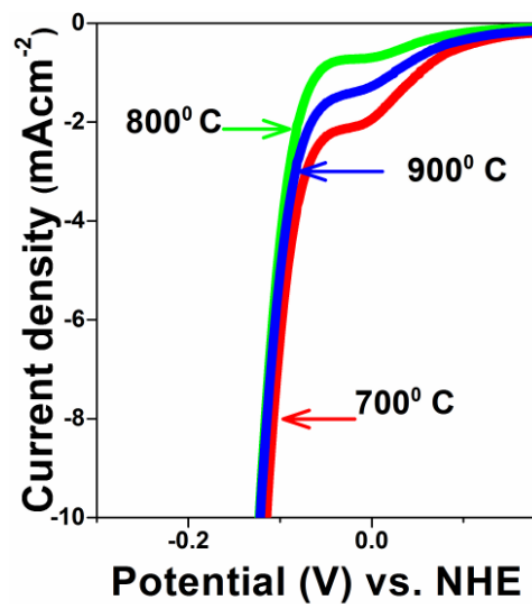


Figure 66: Polarization profiles of MoP/CNT prepared at different synthetic temperatures.

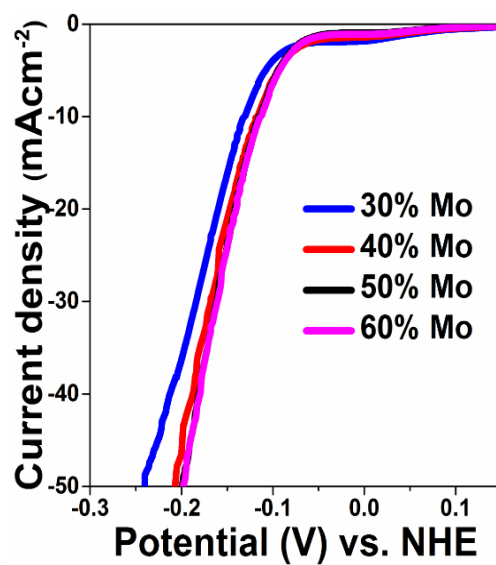


Figure 67: LSVs of MoP/CNT obtained as function of Mo content.

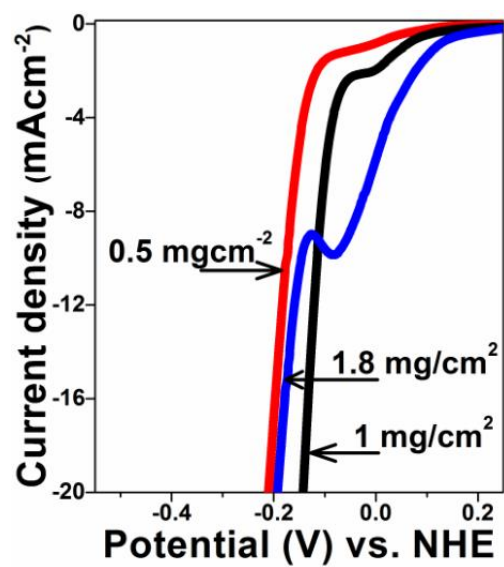


Figure 68: Linear sweep voltammograms showing Effect of catalyst loading of MoP/CNT

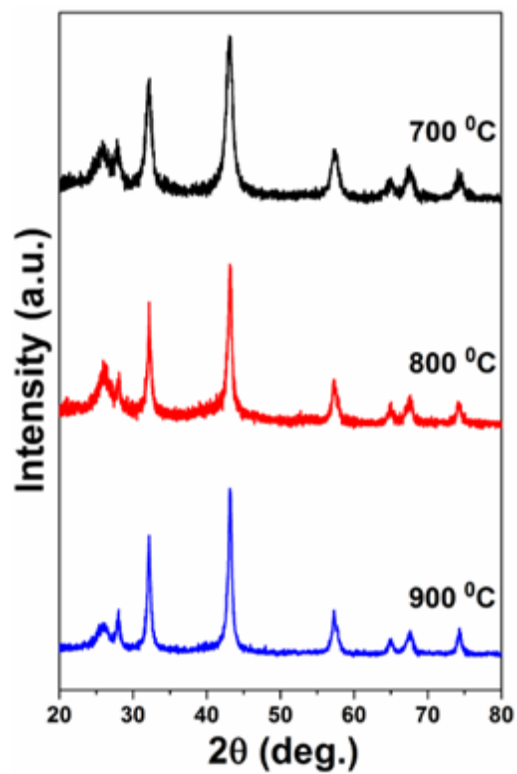


Figure 69: XRD spectra of MoP/CNT obtained at different synthesis temperature.

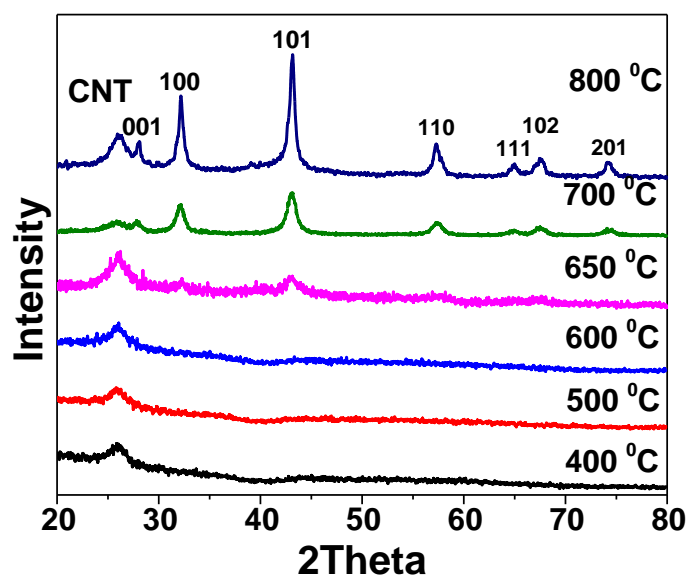


Figure 70: Temperature-dependent evolution in XRD patterns of MoP/CNT obtained in the presence of oxalic acid.

Appendix B

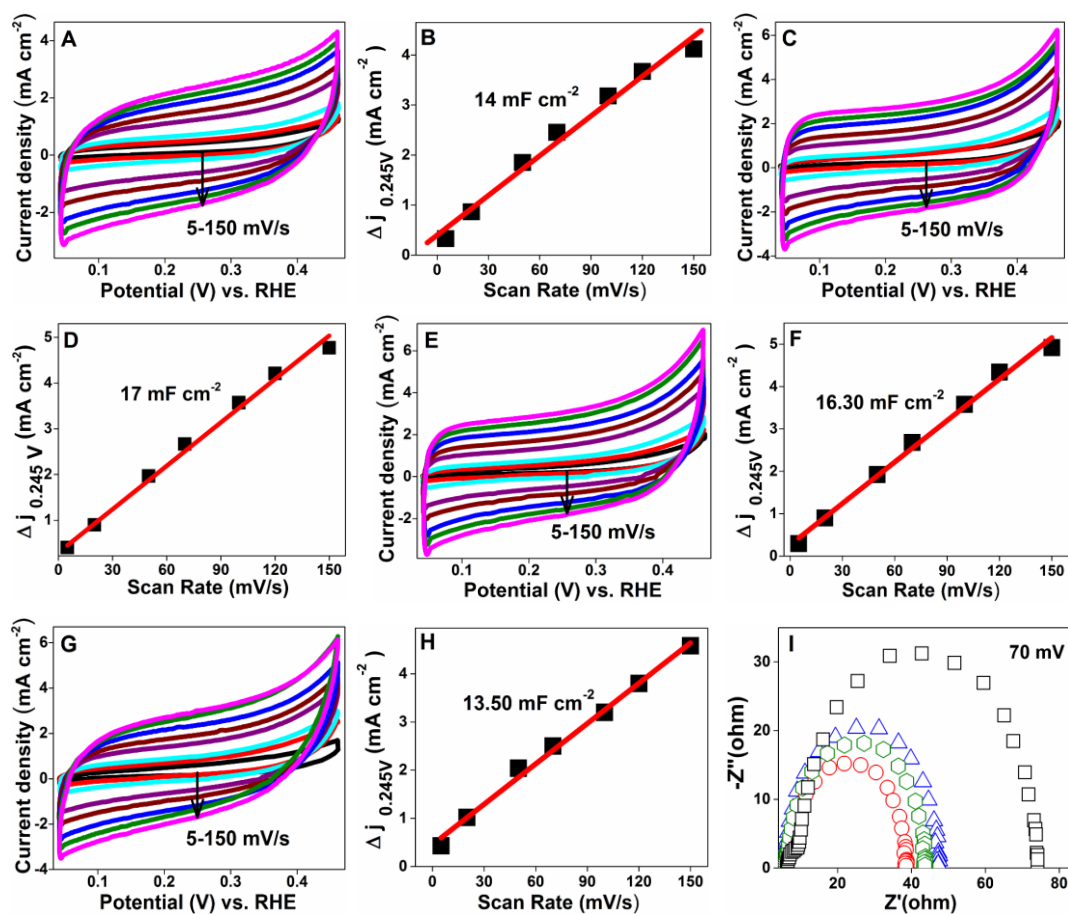


Figure 71: Cyclic voltammograms (A, C, E, G) of CoP/CNT recorded at different scan rates from 5 to 150 mVs⁻¹, and their corresponding plots (B, D, F, H) of the current density at 0.245 VRHE vs. scan rate as a function of CoP content. (I) Nyquist plot as a function of cobalt contents.

Vitae

Name :Alaaldin Mohamed Abdalla Adam

Nationality :Sudanese

Date of Birth :6/24/1982

Email :amabdella5@gmail.com

Address :KFUPM, Dhahran 31261, Saudi Arabia

Academic Background :M.Sc. in chemistry from University of Gezira

List of Publications;

- 1- Qamar, M., **Adam, A.**, Azad, A. M., & Kim, Y. W., Benzyl Alcohol-Mediated Versatile Method to Fabricate Non-Stoichiometric Metal Oxide Nanostructures. ACS Applied Materials & Interfaces, 9.46 (2017): 40573-40579.
- 2- Khan, A., M. I. Ahmed, **A. Adam**, A. M. Azad, and M. Qamar, "A novel fabrication methodology for sulfur-doped ZnO nanorods as an active photoanode for improved water oxidation in visible-light regime." Nanotechnology 28.5 (2017): 055602
- 3- Qamar, M., **Adam, A.**, Merzougui, B., Helal, A., Abdulhamid, O., & Siddiqui, M. N. Metal organic framework-guided growth of Mo₂C embedded in mesoporous carbon as high-performance and stable electrocatalyst for hydrogen evolution reaction. Journal of Materials Chemistry A. 2016, 4(41):16225-32.

- 4- Ahmed, M. I., **A. Adam**, A. Khan, M. N. Siddiqui, Z. H. Yamani, and M. Qamar. "Synthesis of mesoporous NiWO₄ nanocrystals for enhanced photoelectrochemical water oxidation." Materials Letters 177 (2016): 135- 13.
- 5- Ahmed MI, **Adam A.**, Khan A, Rehman A, Qamaruddin M, Siddiqui MN, Qamar M. Improved photoelectrochemical water oxidation under visible light with mesoporous CoWO₄. Materials Letters. 2016, (183):281-4.
- 6- **Adam A.**, Qamar, M. Siddiqui M. N., Oxalate-directed growth of molybdenum phosphide on carbon nanotube as high-performance and durable electrocatalyst for hydrogen evolution reaction, (in progress).
- 7- **A. Adam**, M. Qamar, M. N. Siddiqui, Rational growth of high-performance molybdenum carbide on carbon nanotubes for electrochemical hydrogen evolution reaction, (in progress).
- 8- **A. Adam**, M. Qamar, M. N. Siddiqui, Hollow and Interconnected Scaffold of CoP and Carbon Nanotubes as High Performance Electrocatalyst for Hydrogen Evolution Reaction (in progress).

CONFERENCE PRESENTATIONS:

- 1- Oxalate-assisted synthesis of nanostructured Mo₂C/CNT nanocomposite as a high performance and stable electrochemical hydrogen evolution reaction. **A. Adam**, M. Qamar, B. Merzougui, M.N. Siddiqui. The 4th Saudi International Nanotechnology Conference. held during 25-26th October 2016 at KFUPM, Dhahran, Saudi Arabia.